Generalized Quasilinear Simulation of Turbulent Channel Flow

BY

Colleen B. Kellam

BS, Aerospace Engineering, University of Colorado at Boulder, 2003

MS, Aerospace Engineering, University of Central Florida, 2010

Dissertation

Submitted to the University of New Hampshire

in Partial Fulfillment of

the Requirements for the Degree of

Doctor of Philosophy

in

Mechanical Engineering

September, 2019

This dissertation has been examined and approved in partial fulfillment of the requirements for the degree of Doctor of Philosophy in Mechanical Engineering by:

Gregory Chini, Dissertation Director
Professor of Mechanical Engineering

Steve Tobias
Professor of Applied Mathematics, University of Leeds

John F. Gibson
Associate Professor of Mathematics and Statistics

Christopher White
Associate Professor of Mechanical Engineering

Jeffrey S. Oishi
Assistant Professor of Physics, Bates College

On 11 June 2019

Original approval signatures are on file with the University of New Hampshire Graduate School.

To my mother, who always believed I could fly,

and my father, who left me with his love of mathematics before God called him Home.

Acknowledgments

I credit all of my accomplishments to my personal Savior, Jesus Christ. It is through His richest grace and mercy that I have successfully reached the end of this graduate school journey.

To my advisor, Greg Chini: Your insight into and understanding of the mathematics that describe the physical world are matched only by the extraordinary efforts you make in investing in the education and lives of your students. I am profoundly grateful for the investment you have made in my education, research, and this dissertation, as well as for your encouragement and support the past three years. You have not only directly shaped the type of researcher I will be, you have fundamentally influenced my approach to teaching and mentoring students. Any and all future successes of mine in research and as an educator will truly be a reflection of you. P.S. Thank you for keeping me out of "jail".

To the other members of my committee, John Gibson, Chris White, Steve Tobias, and Jeff Oishi: Thank you for your time, invaluable feedback, and genuine interest in my work. I am so humbled to have had the opportunity to learn from each of you.

To Brandon Montemuro and Aaron Carta: This dissertation would contain nothing but hand turkeys and tears if it were not for your constant help and superhuman patience. Your contributions are inextricably linked to this document, and I am forever thankful.

To Ian Duffy: I am leaving New Hampshire in the best shape of my life, and I owe the complete lifestyle change I have been able to make to you. I am so grateful for your friendship, and for giving me a confidence that has permeated every aspect of my life.

To my incredible network of family, friends, and colleagues (my sister Heather, Carrie Cassidy, Kurt Herzinger, Rilee Bolduc, Aleks Wojtowicz, John Klapp, and so many others): Thank you for your phone calls, texts, e-mails, and prayers these past three years - they always came at the perfect time.

Table of Contents

List of Figures

Abstract

Generalized Quasilinear Simulation of Turbulent Channel Flow

by

Colleen B. Kellam

University of New Hampshire, September, 2019

Direct numerical simulation (DNS) of wall-bounded turbulent flows in physically relevant parameter regimes remains infeasible in many cases of practical interest. Accordingly, this work further establishes the generalized quasilinear (GQL) approximation, introduced by Marston *et al.* (Phys. Rev. Lett., 116, 2016), as a robust, accurate, and efficient alternative to existing simulation and modeling schemes by investigating its effectiveness as a tool for simulating turbulent channel flow. The GQL reduction is achieved by separating the flow variables into low and high modes via a spectral filter rather than by decomposition into a strict mean and fluctuations, as for the quasilinear (QL) approximation, and then neglecting certain nonlinear interactions *a priori*. The effectiveness of GQL over the more common QL approximation scheme and the effect of varying the spectral cutoff on the flow dynamics is explored in two distinct parameter regimes and assessed using a multitude of turbulence statistics, including energy budgets. GQL is shown to be significantly more accurate than QL relative to DNS, even when only a modest number of low modes (e.g., 3-5) is retained. A primary conclusion of this work is that GQL accurately predicts the turbulence intensity and

Reynolds stress profiles, captures the energy distribution across the entire dynamic range of scales, and recovers the characteristic dynamics and turbulence structure of wall-bounded shear flows. A second significant finding is the emergence of a discontinuity in the GQL energy spectra, which is conjectured to be attributable to the lack of modal instability in the high-mode set. A preliminary linear stability analysis about the turbulent mean velocity profile reveals a band of unstable low streamwise wavenumber modes, lending credence to this conjecture and pointing to a more precise methodology. Moreover, the success of the GQL approximation in quantitatively reproducing low-order turbulence statistics and instantaneous flow structure affirms the importance of both linear mechanisms and spectrally nonlocal energy transfers in fully-developed wall-turbulence.

Chapter 1

Introduction

Wall-bounded turbulence is an active area of research that spans an array of scientific and engineering disciplines. It is widely acknowledged that the dynamics of turbulent motion near solid surfaces is largely responsible for the drag force on aircraft and ships, the distribution of heat in the atmosphere, and the energy required to deliver oil through pipelines (Smits and Marusic, 2013). A deeper understanding of the dynamics that underlie the generation and sustenance of turbulence could have profound societal impact by enabling, for example, significant reduction in fuel costs in the airline and shipping industries and greater accuracy and more advanced warning in weather prediction.

Even after a century of research, however, analytical solutions to the partial differential equations (PDEs) that govern turbulent flows have not been found, and despite tremendous advances in computational hardware, direct numerical simulations of turbulent flows in parameter regimes relevant in most engineering applications remain untenable. Consequently, efficient simulation techniques either heavily rely on *ad hoc* modeling of unresolved scales, fail to capture the instantaneous dynamics due to time-averaging, or both. These challenges highlight the need for new computationally-efficient algorithms that employ approximation schemes that are broadly applicable to many different types of flows (i.e., are robust) and that are capable of accurately recovering instantaneous dynamical information while providing insight into the dominant physical processes.

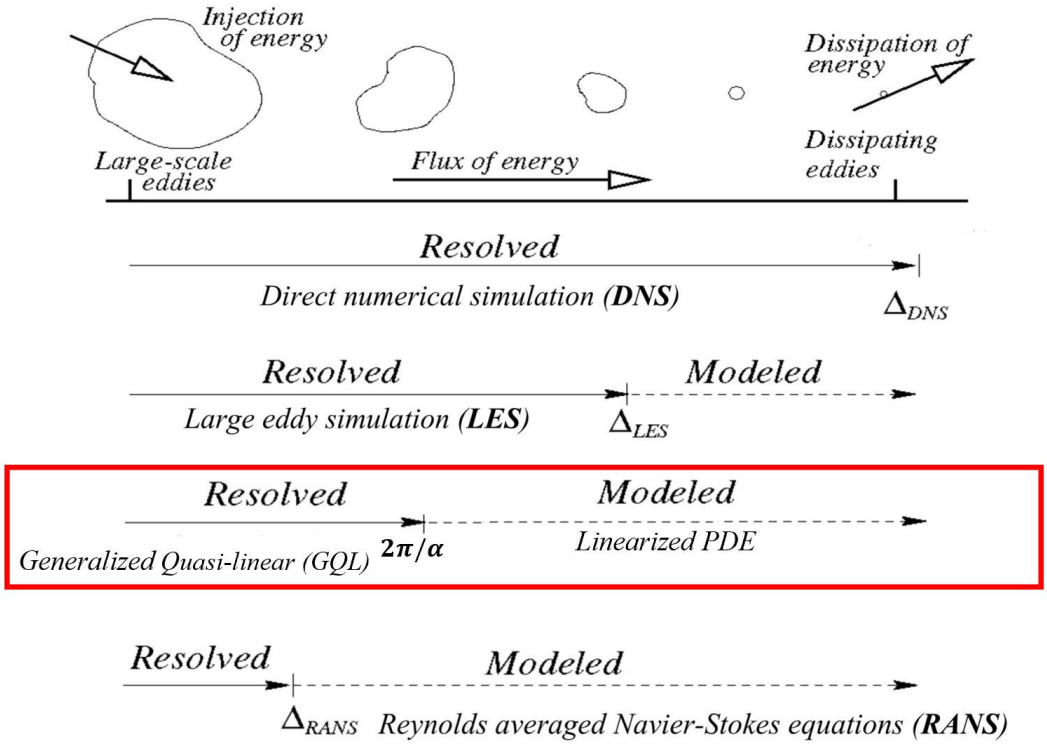

Figure 1.1: Methodologies for simulating turbulent flows, where Δ represents the cutoff between resolved and modeled scales and α is the streamwise wavenumber (Bakker, 2018).

1.1 Current turbulent flow modeling methodologies

Three prevailing methodologies for simulating turbulent flow are direct numerical simulation (DNS), large eddy simulation (LES), and Reynolds averaged Navier-Stokes (RANS) simulation (see Figure 1.1), where the requirement for modeling the unresolved scales ranges from none in DNS to extensive in RANS. DNS offers an "exact" numerical solution to the governing PDEs, but because the entire dynamic range of scales is resolved, the computational cost is prohibitive in parameter regimes of physical relevance. RANS is more computationally feasible, but due to the time-averaging, information about the instantaneous dynamics is lost. Moreover, the use of *ad hoc* models to represent the unresolved dynamics requires extensive tuning and generally lacks robustness.

The generalized quasilinear (GQL) approximation is explored in this work as a potential

	INSTANTANEOUS DYNAMICS	STATISTICAL DYNAMICS
TRUTH	Navier-Stokes Equations (NL)	Cumulant Hierarchy (DSS)
APPROX	Quasilinear (QL)	CE2 (S3T)
	Generalized Quasilinear (GQL)	GCE2

Table 1.1: Relation between instantaneous and statistical dynamical formulations.

alternative to LES. Like LES, GQL employs a decomposition into resolved and modeled scales, but uses a markedly different modeling scheme for the unresolved scales. To close the equations, LES relies on the *addition* of an *ad hoc* model that presumes information about the effect of the unresolved scales on the resolved large-scale eddies. In contrast, GQL employs a linearization of the Navier-Stokes (NS) equations to solve for the small scales by neglecting certain nonlinear interactions *a priori*. Equivalently, GQL removes dynamics defined by the governing PDEs while LES adds dynamics not defined by those PDEs. Moreover, circumstantial evidence suggests that, currently, GQL is as computationally efficient as LES while having the capability of being both more robust and more accurate.

A further motive for studying the GQL algorithm is that, once validated, it can be used as the basis for direct *statistical* simulations (DSS). DSS is being used increasingly in geophysical and astrophysical applications, as the vast range of scales in these flows makes instantaneous methods computationally intractable. In particular, if the statistics of a system are the quantities of primary interest, computational savings can be accrued by solving directly for these statistics rather than by generating and then averaging large data sets. The DSS methods referenced subsequently are shown with their instantaneous counterparts in Table 1.1.

The second-order cumulant expansion (CE2) introduced by Marston et al. (2008) uses the quasilinear (QL) approximation as a closure: a linearized PDE is used to solve for the small-scale statistics. CE2 is also called stochastic structural stability theory (S3T) by Farrell and Ioannou (2003; 2007), but here the nomenclature CE2 will be used. Although CE2 is

able to recover accurate statistics in turbulent flows close to equilibrium, the CE2 algorithm fails to recover important first- and second-order statistics for systems far from equilibrium (Marston et al., 2016). For such flows, a higher-order cumulant truncation or, alternatively, a more accurate second-order closure model is required. Since the GQL approximation can be closed exactly at second order *and* is shown in this and other recent works to be capable of more accurately reproducing second-order statistics than QL-based schemes, it can be used to develop a more robust DSS formulation, introduced by Tobias and Marston (2017) as the generalized cumulant expansion of second order (GCE2). The use of GQL as the basis for a statistical closure is one means of improving the computational efficiency of turbulence simulations.

1.2 Energy transfer and self-sustaining processes in wall-bounded turbulent shear flows

To gain physical insight into the QL and GQL approximations, it is first helpful to understand two crucial phenomena in turbulent wall flows: inter-scale energy transfer and the self-sustaining process (SSP).

Inter-scale energy transfer

A defining characteristic of turbulent flow is the presence of energy-containing eddies exhibiting a range of length scales spanning several orders of magnitude, interacting with each other, continuously changing in time, and giving the appearance of random, chaotic motion (Cushman-Roisin, 2018; Smits and Marusic, 2013). The mechanism that underlies the transfer of energy among these eddies is associated with the nonlinear term in the PDEs governing these flows. A fundamental understanding of this energy transfer process is important for a deeper understanding of turbulence (Domaradzki and Rogallo, 1990).

In classic isotropic turbulence, kinetic energy generally is injected at scales near the largest

length scale of the flow. Energy is then passed down to the smallest scales via nonlinear interactions, where the energy is dissipated into heat. This well-known "energy cascade", introduced by Richardson (1920) and quantified by Kolmogorov (1941), is one manifestation of the interplay between inertial and viscous forces (Cho et al., 2018). The source of energy in shear flows is the gradient of the mean velocity, and the mechanism by which energy is fed into the turbulent cascade is the interaction between the mean velocity gradient and the average momentum fluxes (Reynolds stresses) carried by the velocity fluctuations (Tennekes and Lumley, 1972; Jiménez and Kawahara, 2013). In isotropic turbulence, the range of scales over which the energy must cascade is independent of spatial direction. In wall-bounded shear flows, however, the presence of solid surfaces confines the large energy-containing eddies and the energy cascade becomes a function of distance from the wall (Jiménez and Kawahara, 2013). The anisotropic nature of wall-bounded turbulence thus leads to a phenomenologically more complex mechanism governing energy transfer.

Wall-bounded flows, in particular, present a challenge to LES owing to the wall-normal dependence of the flow scales. Near the wall, even the largest (local) scales are very small, which requires very high temporal and spatial resolution. Insufficient resolution results in the underestimation of the wall-shear stress in LES, which affects the accuracy of the entire simulation (Reynolds, 2000). On the other hand, increasing the resolution to capture the small-scale dynamics eliminates the computational savings inherent in LES. A further disadvantage of LES is the inability to capture the effects of energy transfer from the unresolved scales to the resolved scales, or backscatter.

In this work, a distinction will be made between local and nonlocal energy transfer. Energy transfer is defined relative to two particular scales of motion. If the two scales of motion are similar, the energy transfer is considered to be local. If the two scales of motion are dissimilar, the energy transfer is nonlocal. The isotropic energy cascade described in this section is an example of local energy transfer, in that energy from a given scale is lost to a neighboring smaller scale (Domaradzki et al., 1994). Nonlocal energy transfer occurs when

energy is transferred between non-neighboring scales.

The two approximations investigated in this work, *viz.* QL and GQL, employ different restrictions on the way in which the scales are permitted to interact nonlinearly (and, hence, exchange energy), and will be explained in detail in subsequent sections.

Self-sustaining process

Another defining characteristic of turbulent flows is that they are self-sustaining, The near-wall region in wall-bounded turbulent flows is characterized by large gradients of the flow variables and high momentum transport, and is dominated by streaks of high and low streamwise velocity and associated streamwise vortical structures (Jiménez and Kawahara, 2013). Since the discovery in these flows regions of streamwise-averaged spanwise-varying streamwise velocity, or streaks, by Kline et al. (1967), strong evidence has been accumulated suggesting that the streaks and quasi-streamwise vortices play a vital role in the sustenance of turbulence. Figure 1.2 shows an example of this streaky flow in a horizontal plane near the wall as computed from a DNS of turbulent channel flow. Moreover, Jiménez and Pinelli (1999) showed a single streak and a single pair of quasi-streamwise vortices are able to reproduce with some success the statistics of the full flow.

As is well known, the fundamental challenge to the application of the classical hydrodynamic stability approach to wall-bounded turbulent flows is that the laminar state either completely lacks exponentially-growing linear eigenmodes or is weakly unstable (i.e., with growth rates inversely proportional to the Reynolds number), despite the experimental evidence suggesting strong/rapid instability (Waleffe, 1997). In contrast, the self-sustaining process (SSP) approach pioneered by Waleffe (1997) seeks to understand the mechanisms and processes by which turbulence is sustained. His SSP theory was motivated in part by the work of Jiménez and Moin (1991) in which a continuation technique is used, but rather than tracking fixed points, the turbulent solution is tracked instead. This procedure confirmed that the nonlinear interactions of growing eigenmodes arrising not from an instability of the

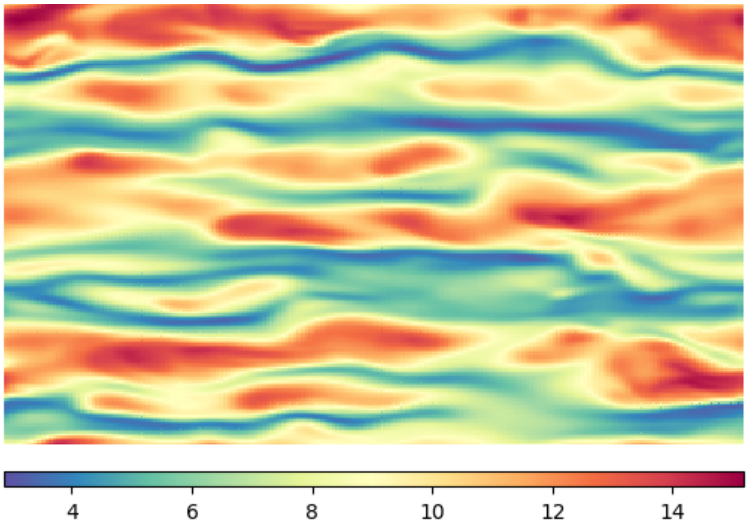

Figure 1.2: Streamwise velocity in the plane parallel to the walls in the near-wall region of turbulent channel flow.

laminar state but rather from the *streaks* does indeed feed back onto (and, hence, sustain) the streamwise rolls.

More specifically, the self-sustaining process introduced by Waleffe (1997) is an extension of the mean-flow/first-harmonic theory by Benney (1984) and hairpin vortical studies by Acarlar and Smith (1987). In this process, the spanwise-wall-normal rolls elongated in the streamwise direction redistribute the mean shear to create streaks that are unstable through an instability of inflectional type, and the nonlinear self-interaction of the 3D perturbation that results from the instability directly feeds back onto the rolls, thus completing a feedback loop. The self-sustaining process of Waleffe (1997) provides a compelling framework for understanding the underlying instability maintaining turbulence in wall-bounded shear flows using a mechanistic approach. It should also be noted that similar conclusions have been drawn analytically using an asymptotic approach, termed vortex-wave interaction (VWI) theory. Specifically, Hall and Smith (1991) and Hall and Sherwin (2010) demonstrate that the interaction between longitudinal vortices and an accompanying Rayleigh instability mode results in a finite-amplitude equilibrium (i.e., self-sustaining) state. Crucially, in VWI and its extension by Chini et al. (2017), the Rayleigh mode satisfies a *linearized* equation about the streamwise-mean streaky flow. Moreover, these asymptotic theories show that a *single*

streamwise-varying mode can sustain the nonlinear state; in this sense, these theories provide the basis for a *minimal* model of turbulence.

Like VWI and SSP theories, the (generalized) quasilinear approximation exploits the notion that the streak instability plays a central role in wall turbulence, in that the governing equations are linearized about the streamwise-invariant streaks. Stated another way, instead of decomposing into a time-averaged mean flow and fluctuations about the time-averaged mean, as is the standard practice in Reynolds averaging, the Navier-Stokes equations are linearized about the *streamwise-averaged* mean. The analytical details of this linearization will be provided in subsequent chapters, but both the motivation for and merit of this choice derive from the physical essence of the SSP of Waleffe (1997) and are further substantiated by the analytical results of Hall and Smith (1991), Hall and Sherwin (2010), and Chini et al. (2017).

1.3 Generalized quasilinear (GQL) approximation

Development of quasilinear (QL) theory

The generalized quasilinear approximation (GQL) is an extension of the quasilinear (QL) approximation, which is rooted in the early derivation of analytical theories for turbulent interactions and the interactions between waves and mean flows (Marston et al., 2016). Quasilinear theory was first introduced by Stuart (1958), when he hypothesized that the dominant non-linear interaction in a turbulent flow is between the suitably-defined mean flow and the first harmonic component of the disturbance (i.e., the fluctuation about the mean). By ignoring higher-order terms, a method for approximating the dynamics can be developed (Stuart, 1958). In the same era, Herring (1963) utilized closely related concepts in the development of mean field theory for turbulent convection. Under the quasilinear approximation, each flow field generally is decomposed into a suitable *spatial* mean plus a fluctuation component, and fluctuation/fluctuation nonlinearities are retained only where

they feed back upon the mean fields. One crucial physical consequence is that energy cannot scatter among the fluctuations, which severs the energy cascade described in Section 1.2.

The QL approximation has proven useful in the development of a direct statistical simulation (DSS) approach for scenarios in which the flow statistics of a system are of greater interest than instantaneous dynamics (Tobias et al., 2011). This is often the case for astrophysical and atmospheric phenomena, for which a DNS is computationally untenable in parameter regimes of interest and LES (or other sub-grid) models require extensive *ad hoc* modeling (Tobias et al., 2011). Another QL theory is known as the restricted nonlinear (RNL) model, in which fluctuation-fluctuation interactions either are neglected or stochastically parameterized and only a small band of fluctuation modes is retained. RNL has been shown to sustain turbulence with a modest number of fluctuation modes and even when only a single fluctuation mode is retained, as first demonstrated by Thomas et al. (2014, 2015) in Couette flow and later by Farrell et al. (2016) in Poiseuille flow, and as earlier anticipated by the VWI theory of Hall and Smith (1991) and Hall and Sherwin (2010) and the asympotitcally-reduced model of Beaume et al. (2015). If fluctuation-fluctuation interactions are neglected (rather than stochastically parameterized) and a single fluctuation mode is retained, the nomenclature "constrained RNL" model is used, which is identical to the single-mode quasilinear (SMQL) approximation referred to in this work. An additional, "band-limited" RNL model was introduced by Bretheim et al. (2018), whereby an optimal set of non-zero streamwise wavenumbers are retained. This specialized "sideband truncation" yields a computationally-efficient numerical scheme, a concept that can also be explored in GQL (Boyd, 2001).

While investigators using the QL approximation have been able to recover large-scale dynamics of the system and see improvement in efficiency over DNS, the suppression of energy scatter among the fluctuation modes leads to significant inaccuracies in first- and second-order statistics, which becomes more evident the further the system is driven from equilibrium (Marston et al., 2016). Numerous investigators have shown that in wall-bounded

shear flows, QL over-predicts homogenization, or mixing, in the core and inaccurately recovers the Reynolds stresses (Thomas et al., 2014; Farrell et al., 2016; Tobias and Marston, 2017; Bretheim et al., 2018). As a result, the dynamics and structure of the flow are fundamentally altered by the QL approximation.

Development of the generalized quasilinear (GQL) algorithm

The GQL approximation, first introduced by Marston et al. (2016), was developed to improve upon the accuracy of QL simulations relative to full direct numerical simulations. The GQL reduction is achieved by separating the flow variables into low and high modes via a spectral filter rather than by decomposition into a strict mean and fluctuations. Nonlinear coupling among the high modes is retained only where this coupling projects onto the dynamics of the low modes, which are allowed to undergo fully nonlinear interactions. Because spectrally non-local energy scatter is permitted, there is improved recovery of small-scale dynamics and overall energy distribution in the system. Further, GQL can retain an user-specified number of low-mode interactions, allowing for a systematic way to investigate the behavior of nonlinear interactions.

The GQL approximation has been employed previously in the investigation of several systems. In the first study, Marston et al. (2016) used GQL to simulate two-dimensional driven turbulence on a spherical surface and on a 'β-plane', the latter being a paradigmatic problem for understanding the formation of jets in the atmosphere and oceans and in planetary and interstellar gas bodies. Relative to the fully nonlinear simulations, GQL was shown to better reproduce (particularly second-order) statistics and instantaneous dynamics than QL, even when just a single additional mode is included in the set of large scales. Next, Child et al. (2016) examined GQL in the context of the axisymmetric (two-dimensional) helical magnetorotational instability (HMRI), which is thought to be a key mechanism in the formation of stars and black holes. Although the dynamics of this system are quite different from zonal jets, investigators again found that GQL performed significantly better than QL

in reproducing the statistics of the HMRI, even when a modest number of large-scale modes is retained. Another outcome is the formulation of a new DSS method based on the GQL approximation, which promises to yield better statistical results in systems where CE2 has been shown to be inadequate. Motivated in part by the possibility of implementing such a second-order closure method for DSS, Tobias and Marston (2017) investigated the effectiveness of GQL in simulating three-dimensional rotating Couette flow. Non-rotating Couette flow is a canonical problem in the class of wall-bounded shear flows, and is dynamically distinct from the systems previously explored using the GQL approximation. In three dimensions, Couette flow turbulence (whether rotating or not) is anisotropic in the horizontal directions and exhibits a forward energy cascade, characteristics that were absent in the 2D models previously explored. Tobias and Marston (2017) employed the GQL approximation in both horizontal directions, and concluded that the GQL approximation, even with only a few (< 5) large-scale modes, is significantly more effective at reproducing first- and second-order statistics relative to a QL approximation in one or both translationally invariant directions. Although this conclusion accords with that of other investigators, it is especially interesting considering the presence of the forward energy cascade (Tobias and Marston, 2017). Finally, Tobias et al. (2018) investigated GQL in a class of convective systems in which the driving of the velocity is effected by buoyancy and other dynamical fields rather than via imposed small-scale forcing or through the boundaries. Using the Busse annulus model, it was again demonstrated that GQL (even with a modest number of low modes retained) significantly outperformed QL in reproducing the dynamics of the flow.

The present work seeks to further validate GQL as an effective methodology for recovering the statistics and instantaneous dynamics of turbulent flows. To complement previous investigations focusing on astrophysical and geophysical systems, this work explores the effectiveness of the GQL approximation in turbulent channel (i.e., plane Poiseuille) flow, a paradigm problem for engineering turbulence. As for other turbulent systems, GQL can also be used to probe the behavior of the nonlinear interactions in wall-bounded shear flows.

Crucially, however, unlike rotating Couette flow, turbulent channel flow is only weakly (viscously) linearly unstable.

1.4 Objectives

The overarching aim of this work is to continue to develop the relatively new GQL methodology as an alternative to existing methods of simulating turbulent flows. To accomplish this goal, the GQL approximation will be used in the simulation of 3D turbulent channel flow, thereby broadening scope of applicability of GQL to engineering flows. This primary aim will be met by pursuing three broad objectives:

Accuracy and robustness of GQL in turbulent channel flow

To assess accuracy and robustness of the GQL approximation, GQL simulations at various truncations are compared to QL simulations and to DNS in two parameter regimes for a range of low/high mode partitions in the streamwise direction. A host of metrics are used to determine how well GQL recovers the statistics and instantaneous dynamics of the flow relative to the fully nonlinear (NL) simulation (i.e., to DNS). The primary analysis is performed in the highest Reynolds number regime simulated using GQL to date, while the second parameter regime is at a lower Reynolds number in an extended horizontal domain.

Insight into nonlinear energy transfer between scales

The algorithm used for simulating GQL accepts the desired truncation (i.e., partition between low and high streamwise modes) as an user input. The various truncations of GQL simulations are chosen to enable systematic investigation of the effect of allowing or prohibiting certain nonlinear interactions in the low modes. The impact of the GQL approximation on the flow is explored by comparing turbulence metrics with those obtained from fully nonlinear simulations and by both physical-space and spectral nonlinear energy

transfers. This approach yields insight into how energy and momentum are transferred by turbulent motions in inhomogeneous anisotropic flows.

Computational efficiency of GQL

There is ample scope to explore ways to reduce the computational cost of GQL simulations, thereby improving efficiency while not sacrificing accuracy. Although these approaches are not explored in depth in this work, sufficient evidence is acquired to suggest this new methodology is accurate, leaving the door open for future studies aiming to increase efficiency. Accordingly, preliminary computational efficiency data are collected for simulations performed and included as an appendix.

1.5 Outline of dissertation

This section outlines the organization of the dissertation.

In Chapter 2, the initial-boundary value problem for channel flow used in this investigation is formulated, along with definitions of the non-dimensionalization, physical and Fourier representations of the equations of motion and energy equations, and notation used throughout. This chapter is also intended to provide necessary background knowledge on wall-bounded shear flows and to define and outline the turbulence metrics used to examine the accuracy of the GQL algorithm. This includes first- and second-order statistics and methods for characterizing the structure and topology of the flow.

In Chapter 3, the derivations of the algorithms employed in this work are presented. In Section 3.1, the derivation of the QL approximation and the development of an algorithm for a minimum model of QL, the single mode quasilinear (SMQL) reduction, is presented. In this algorithm, which is implemented in MATLAB, the three-dimensional problem is reduced to a "$2+\epsilon$"-dimensional system by retaining only a single streamwise fluctuation mode. In Section 3.2, the derivation of the GQL reduction is presented. The algorithm, written in Python and using the Dedalus spectral framework for solving partial differential equations

developed by Burns et al. (2019), operates in four modalities: SMQL, QL, GQL, and NL.

In Chapter 4, the results and analysis of GQL simulations in the high(er) Reynolds number parameter regime are presented. A number of metrics are used to quantify the effectiveness of the GQL algorithm, including the mean velocity and mean velocity gradient profiles, instantaneous and fluctuating velocity fields, enstrophy, Reynolds stress profiles, turbulent structures and coherent patterns of the turbulent flow field, and physical and spectral energy analysis. It is conclusively shown that the GQL simulations are better able to recover the first- and second-order statistics of the fully nonlinear solution. Furthermore, the necessary number of large-scale modes retained to achieve such agreement is modest (< 3). In particular, GQL simulations are remarkably accurate in reproducing the turbulence intensity and Reynolds stress profiles, which specifically addresses the primary shortcomings of the QL approximation. A major finding is the identification of a discontinuity in the spanwise-averaged streamwise energy spectra, which will be discussed in detail in a subsequent chapter.

In accord with the overarching objective, select simulations are performed at a lower Reynolds number but in an extended spatial domain to determine the difference, if any, in the effectiveness of GQL. The resulting analysis is summarized in Chapter 5. First, SMQL simulations are performed using both the MATLAB- and Python-based algorithms and the first-order statistics are compared to the fully nonlinear simulation. In this way, the algorithm written in MATLAB provides an external validation of the Dedalus code, at least for first-order statistics. Then, a subset of the turbulence metrics used in the higher Reynolds number regime are utilized to assess the effectiveness of select GQL simulations in this distinct, lower Reynolds number parameter regime. Again, GQL demonstrates the ability to accurately recover flow statistics and instantaneous dynamics, even when only three low modes are retained.

Finally, the spectral energy discontinuity observed in the GQL simulations is explored in Chapter 6. It is conjectured that the discontinuity is a consequence of modal instabilities being entirely contained in the low-mode set. To test the conjecture, hydrodynamic stability

theory is employed to determine the stability of the long-time and horizontal mean turbulent flow. A band of unstable modes at $Re_\tau = 200$ is identified by numerically solving a modified Orr-Sommerfield stability problem in which an anisotropic eddy viscosity model introduced by Sen and Veeravali (2000) is used. Although this result lends credence to the conjecture, quantitative prediction of the band of unstable streamwise modes is sensitive to the precise form of the eddy viscosity model chosen, suggesting a more careful stability analysis of the (two-dimensional) time- and streamwise-averaged streak flow ultimately may be necessary.

Chapter 2

Problem Formulation and Background

In this chapter, the equations and boundary conditions governing channel flow, the paradigm problem used exclusively in this work, are specified. Background material on wall-bounded shear flows is also provided, which may be skimmed by a well-informed reader without loss of understanding of the later chapters. Since the primary objective is to validate the GQL approximation, important turbulence metrics appropriate for channel flow are introduced.

2.1 Description of channel flow

2.1.1 Governing equations

Channel flow, or plane Poiseuille flow, is a pressure-driven flow between two parallel stationary plates, as shown in Figure 2.1. The x coordinate is aligned with the streamwise direction, y with the spanwise direction, and z with the wall-normal direction. The size of the channel is $[L_x, L_y, L_z]$, where $L_z = 2h$ and h is the channel half-height. For an incompressible Newtonian fluid, the governing PDEs are the incompressible (3D) Navier-Stokes equations:

$$\partial_t \boldsymbol{u} + \boldsymbol{u} \cdot \nabla \boldsymbol{u} = -\frac{1}{\rho} \nabla p + \nu \nabla^2 \boldsymbol{u} + \boldsymbol{F} \tag{2.1}$$

$$\nabla \cdot \boldsymbol{u} = 0 \tag{2.2}$$

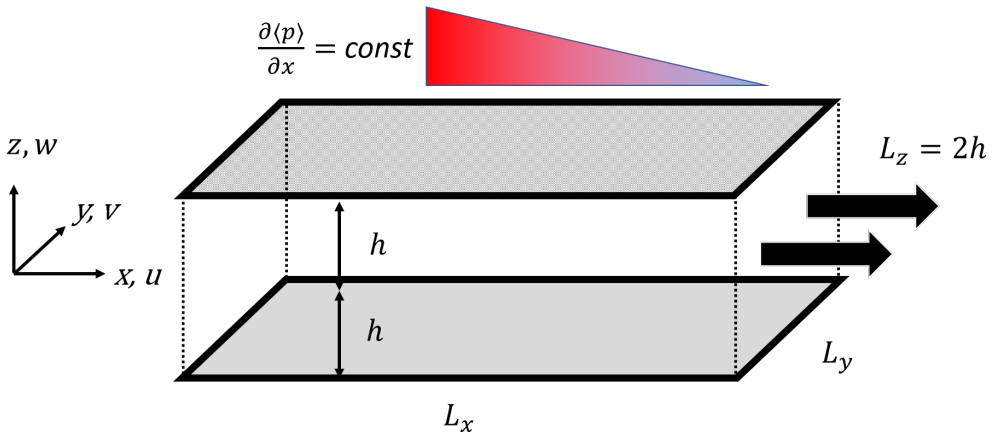

Figure 2.1: Schematic of the channel flow geometry used throughout this work (Tsukahara et al., 2005).

where $\boldsymbol{u} = (u, v, w)$ is the velocity field, p is the pressure distribution, $\boldsymbol{F}$ is the forcing due to the mean pressure gradient applied in the streamwise direction, ρ is the (constant) density, and ν is the (constant) kinematic viscosity.

Equations (2.1) and (2.2) are subject to no-slip/no penetration boundary conditions

$$\boldsymbol{u} = (u, v, w) = (0, 0, 0) \text{ at } z = \pm h \tag{2.3}$$

In this work, the mean pressure gradient that drives the flow is taken to be constant, which fixes the (mean) streamwise velocity gradient at the wall. Thus $\boldsymbol{F} = [-\frac{1}{\rho}\frac{d\langle p\rangle}{dx}, 0, 0]$. Averages are indicated by the use of angled brackets and the type of averaging is specified by a subscript (e.g., $\langle\cdot\rangle_{x,t}$) or redefined explicitly. The use of angled brackets without a subscript indicates a generic averaging operation, to be later specified.

2.1.2 Non-dimensionalization

The system of equations described by Equations (2.1) to (2.3) is rendered dimensionless using the channel half-height, h, and the characteristic time scale $h/\sqrt{Gh}$, where $G = -\frac{1}{\rho}\frac{d\langle p\rangle}{dx}$ is the term associated with the constant pressure gradient driving the flow in the streamwise direction. The friction Reynolds number is therefore defined as $Re_\tau = \frac{u_\tau h}{\nu}$, where $u_\tau = \sqrt{Gh}$ is the friction velocity; i.e., the square-root of the ratio of the mean wall shear stress to the

density.

The governing PDEs therefore can be expressed as

$$\partial_t \boldsymbol{u} + \boldsymbol{u} \cdot \nabla \boldsymbol{u} = -\nabla p + \frac{1}{Re_\tau} \nabla^2 \boldsymbol{u} - 1\hat{x} \tag{2.4}$$

$$\nabla \cdot \boldsymbol{u} = 0 \tag{2.5}$$

where all variables and parameters in Equations (2.4) and (2.5) and henceforth are dimensionless. The dimensionless size of the channel is $[L_x,\ L_y,\ 2]$ and the nondimensional boundary conditions become

$$\boldsymbol{u} = (u, v, w) = (0, 0, 0) \text{ at } z = \pm 1 \tag{2.6}$$

Periodicity of all fields is imposed in x and y, with spatial periods L_x and L_y, respectively.

2.2 Wall regions and scaling

The dependence of the dynamic range of scales on distance from the wall leads to the division of the flow into specific regions, shown in Figure 2.2 for high Reynolds number ($Re_\tau = 10^4$). Very close to the wall, viscosity is important, and viscous stresses are large compared to Reynolds stresses. The viscous scales obtained using dimensional analysis are defined as

$$u_\tau = \sqrt{\frac{\tau_w}{\rho}} \qquad \text{friction velocity} \tag{2.7}$$

$$\delta_\nu \triangleq \sqrt{\frac{\rho}{\tau_w}} = \frac{\nu}{u_\tau} \qquad \text{viscous length scale} \tag{2.8}$$

$$\mathrm{Re}_\tau \triangleq \frac{u_\tau h}{\nu} \qquad \text{friction Reynolds number} \tag{2.9}$$

$$\boldsymbol{x}^+ \triangleq \frac{\boldsymbol{x}}{\delta_\nu} \qquad \text{inner (or wall) units} \tag{2.10}$$

where the dimensional wall shear stress, τ_w, is defined as

$$\tau_w = \rho\nu \left.\frac{d\langle u \rangle}{dz}\right|_{z^+=0} \tag{2.11}$$

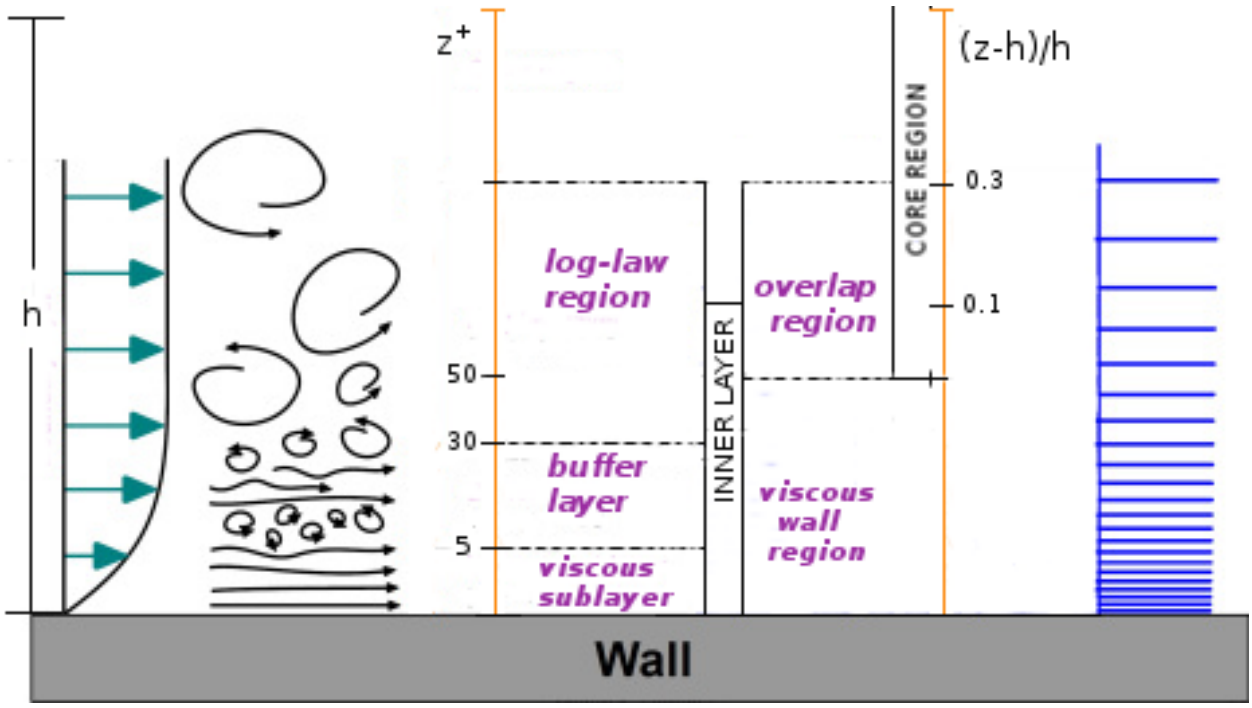

Figure 2.2: Wall regions in channel flow at high Reynolds number ($Re_\tau = 10^4$) (Pope, 2000; Khamlaj, 2018).

Based on this scaling, the friction Reynolds number and the Reynolds number associated with the centerline velocity are related by $Re_{CL} = Re_\tau^2$. It should also be noted that in Figure 2.2 and for purposes of data analysis, the wall-normal coordinate z^+ measures distance, in viscous units, from the top wall (i.e., $z^+ = (1 - z)/\delta_\nu$). All references to z^+ use this convention but other viscous lengths indicated by the $+$ are in accord with Equation (2.10).

An accurate approximation of the equations of motion should be able to reproduce the properties in each region, as explored in depth in later chapters. Here, the defining characteristics of each region are briefly reviewed and related to the metrics used in the analysis where applicable.

The inner layer is characterized by the presence of spanwise-varying streaks of streamwise velocity and by counter-rotating, streamwise vortical structures (Jiménez and Kawahara, 2013). The boundary conditions described by Equation (2.6) require two-component flow in horizontal planes (i.e., u and v are nonzero and $z-$dependent) very close to the wall ($z^+ < 1$)

Pope (2000). Away from the wall, viscous stresses are negligible and the turbulent core of the channel is characterized by large energy-containing eddies of the size $\mathcal{O}(h)$ (Jiménez and Kawahara, 2013). The appropriate scaling in this region is based on the channel half-height, h, and the friction velocity, u_τ. When the Reynolds number is sufficiently large, there is a region between the inner and outer layer that is far enough from the wall for viscous stress to be negligible but where the total (mean plus turbulent) shear stress is constant. In this log-law region, the mean velocity is proportional to the natural logarithm of the distance from the wall scaled in wall units Pope (2000). The emergence of the log-layer can be demonstrated in a number of ways using turbulence metrics and provides another quantitative way to show the accuracy of the approximation technique described in this work.

2.3 Physical and spectral representations of the governing PDEs

2.3.1 Reynolds decomposition

Since turbulent flows are spatio-temporally chaotic, the flow frequently is decomposed into a suitable mean of the velocity and pressure fields and fluctuations about the mean. In this section, the averaging notation $\langle\cdot\rangle$ represents a generic mean, to be specified subsequently.

Let the velocity field be decomposed as $\boldsymbol{u} = \boldsymbol{U} + \boldsymbol{u}'$, where $\boldsymbol{U} = \langle \boldsymbol{u} \rangle$ is the generic mean and the prime notation denotes the fluctuations about the mean. The pressure field is expressed similarly. Substituting the decomposed velocity and pressure fields into Equation (2.4) and following the rules of projection (or ensemble rules of averaging), yields evolution equations for the mean and the fluctuations about the mean:

$$\partial_t \boldsymbol{U} + \boldsymbol{U} \cdot \nabla \boldsymbol{U} - 1\hat{x} + \nabla P - \frac{1}{Re}\nabla^2 \boldsymbol{U} = -\langle \boldsymbol{u}' \cdot \boldsymbol{\nabla} \boldsymbol{u}' \rangle \tag{2.12}$$

$$\partial_t \boldsymbol{u}' + \boldsymbol{U} \cdot \nabla \boldsymbol{u}' + \boldsymbol{u}' \cdot \nabla \boldsymbol{U} + \nabla p' - \frac{1}{Re}\nabla^2 \boldsymbol{u}' = -(\boldsymbol{u}' \cdot \nabla \boldsymbol{u}' - \langle \boldsymbol{u}' \cdot \boldsymbol{\nabla} \boldsymbol{u}' \rangle) \tag{2.13}$$

The term on the right-hand side of Equation (2.12) is the gradient of the so-called

Reynolds stresses, which is of primary importance in understanding the dynamics of turbulence. Reynolds stresses are also responsible for the "closure problem" in turbulence: the mean equations of motion are not closed strictly in terms of mean fields, thus necessitating the use of methods for obtaining the unknown information (e.g., Reynolds stresses). The desire to employ systematic approximation schemes is one of the motivations for developing the GQL algorithm. Equations (2.12) and (2.13) will be used in Chapter 3 to illustrate the application of the quasilinear (QL) and generalized quasilinear (GQL) approximations.

2.3.2 Turbulent kinetic energy equation

The mechanism by which energy is transferred between the different scales of motion to generate and maintain turbulence is of particular interest in this work. Turbulent kinetic energy (per unit mass), k, is defined as

$$k = \frac{1}{2}\langle u_i' u_i' \rangle \tag{2.14}$$

where the summation convention is assumed.

An evolution equation for the mean and turbulent kinetic energy can be derived by forming the inner product of Equation (2.4) with $\boldsymbol{u}$ and employing the velocity and pressure decomposition described in Section 2.3.1. For channel flow, the evolution of the turbulent kinetic energy is associated with the fluctuation equation:

$$\frac{\partial k}{\partial t} + \langle \boldsymbol{u} \rangle \cdot \nabla k = \underbrace{-\langle u'w' \rangle \frac{\partial \langle u \rangle}{\partial z}}_{1} \underbrace{- \frac{1}{2}\frac{\partial}{\partial z}\langle w \boldsymbol{u} \cdot \boldsymbol{u} \rangle}_{2} \underbrace{- \frac{1}{\rho}\frac{\partial}{\partial z}\langle w'p' \rangle}_{3} + \underbrace{\nu \frac{\partial^2 k}{\partial z^2}}_{4} \underbrace{- 2\nu \langle s_{ij} s_{ij} \rangle}_{5} \tag{2.15}$$

where horizontal homogeneity with respect to the averaging operation $\langle \cdot \rangle$ has been assumed and the fluctuating rate of strain tensor s_{ij} is defined as

$$s_{ij} = \frac{1}{2}\left(\frac{\partial u_i'}{\partial x_j} - \frac{\partial u_j'}{\partial x_i} \right) \tag{2.16}$$

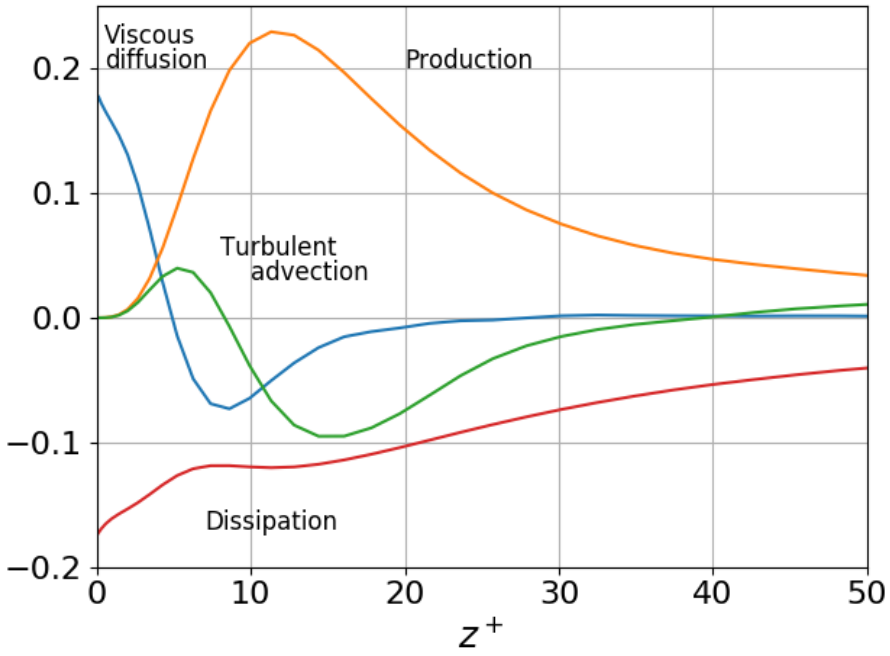

Figure 2.3: Turbulent kinetic energy budget from a DNS of turbulent channel flow at $Re_\tau = 200$ in the (nondimensional) spatial domain $[2\pi, \pi, 2]$ (adapted from Figure 7.18 of Pope (2000)). Note that the pressure transport term is not shown.

The kinetic energy equation is also shown graphically in Figure 2.3. The terms on the right hand side of Equation (2.15) are associated with the following physical processes, as described by Pope (2000):

Term 1: Production (or generation) rate of turbulent kinetic energy, $\mathcal{P}$, which is the result of the vertical Reynolds shear stress acting on the mean velocity gradient, the source term in channel flow. Thus, $\mathcal{P}$ represents the rate at which kinetic energy is transferred from the mean flow to the turbulent eddies. Peak production occurs in the buffer layer at $z^+ \approx 12$, the location where viscous stress and Reynolds shear stress are approximately equal.

Term 2: Turbulent transport (or turbulent advection), $\mathcal{T}$, arises from the nonlinearity of the governing differential equations and transports energy among the different scales (to the wall and to the log-region). Since the GQL approximation restricts certain nonlinear interactions by construction, turbulent transport is of significant interest in this work.

Term 3: Pressure transport. Near the location of peak production, turbulent production

exceeds dissipation, the (small) excess power being carried by the pressure transport.

Term 4: Viscous diffusion, which transports energy towards the wall.

Term 5: Viscous dissipation of turbulent kinetic energy, $2\nu\langle s_{ij}s_{ij}\rangle$. The viscous dissipation term in this equation is often represented by the pseudo-dissipation, $\tilde{\epsilon}$, which is related to the true dissipation by the relation

$$\tilde{\epsilon} = 2\nu\langle s_{ij}s_{ij}\rangle - \nu\frac{\partial^2\langle u_i'u_j'\rangle}{\partial x_i \partial x_j} \tag{2.17}$$

However, the second term in Equation (2.17) is usually small so it will be assumed $\tilde{\epsilon} = 2\nu\langle s_{ij}s_{ij}\rangle$. Viscous dissipation is balanced, on average, by viscous diffusion at the wall.

2.3.3 Spectral-space representation of governing equations

One objective of this work is to gain insight into the nonlinear interactions under the generalized quasilinear approximation. The systematic construction of the GQL algorithm lends itself to examining the effect of restricting particular nonlinear interactions on the process by which energy is transferred locally and non-locally between the large scale motions and the small scale motions. Although the governing equations as written in Equation (2.4) fully describe the dynamics of the flow, they do not provide detailed information about the process by which energy is transferred among the dynamic range of scales, or which of the eddies are involved in the transfer. Employing a Fourier decomposition of the velocity field in the horizontal (streamwise and spanwise) directions facilitates deductions regarding the contributions made by motions of different lateral scales (identified by the different horizontal wavenumbers) to the dynamics of the flow (Domaradzki et al., 1994).

Another compelling reason to use Fourier methods is related to numerical accuracy. In contrast to finite difference methods, which use local, usually low-order, approximations of functions, a spectral method is a global approximation that makes use of high-order polynomials or Fourier series. The two distinct advantages of global methods are the improvement in accuracy and the reduction of numerical (artificial) dissipation in the numerical method.

These advantages are particularly important when simulating turbulent flows. Artificial dissipation from the numerical model can easily swamp the physical dissipation, which would significantly affect the accuracy of the simulation (Trefethen, 2000). A more accurate discretization also allows for a coarser numerical grid, which significantly reduces computational time. The spectral method used predominantly in this work (through the Dedalus software) is a first-order generalized tau method (Burns et al., 2019).

Recall from Section 2.1 the turbulent channel with domain $[L_x \times L_y \times L_z]$. The flow is statistically homogeneous in the streamwise (x) and spanwise (y) directions, which permits a Fourier representation with N_x and N_y modes on a uniformly spaced horizontal grid with grid spacings $\Delta x = L_x/N_x$ and $\Delta y = L_y/N_y$ and periodic boundary conditions in those directions (Pope, 2000). In the wall-normal (z) direction, the flow is not statistically homogeneous and physical boundary conditions are required. Accordingly, in this non-periodic direction, Chebyshev polynomials are used, and the grid spacing is non-uniform with finer grid spacing near the boundaries, ideal for capturing the dynamics of the smallest scales. The non-uniform blue grid on the right side of Figure 2.2 illustrates the effect of such a grid. The state variables can then be represented as truncated Fourier series, where, for example, the velocity field is

$$\boldsymbol{u}(\boldsymbol{x}, t) = \sum_{k_x=-\frac{N_x}{2}+1}^{N_x/2} \sum_{k_y=-\frac{N_y}{2}+1}^{N_y/2} \hat{\boldsymbol{u}}(k_x, k_y, z, t) e^{i\frac{2\pi k_x}{L_x}x + i\frac{2\pi k_y}{L_y}y} \tag{2.18}$$

The real streamwise and spanwise wavenumbers are defined as $\alpha = 2\pi k_x/L_x$ and $\beta = 2\pi k_y/L_y$ respectively. The integer-valued mode numbers k_x and k_y are constrained by an even number of discrete grid points N_x and N_y.

A more compact notation is to express the wavenumbers in vector form, where $\boldsymbol{\kappa} = (\alpha, \beta)$. It follows that $|\kappa| = \sqrt{\alpha^2 + \beta^2}$, and the magnitudes of the lowest wavenumber in the streamwise and spanwise directions, $\alpha_0 = 2\pi/L_x$ and $\beta_0 = 2\pi/L_y$, are associated with the largest possible scale permitted by the geometry of the problem.

The evolution equation for the velocity $\hat{\boldsymbol{u}}(\boldsymbol{\kappa}, z, t)$ in wavenumber space is

$$\partial_t \hat{\boldsymbol{u}}(\boldsymbol{\kappa}, z, t) = \hat{\boldsymbol{N}}(\boldsymbol{\kappa}, z, t) + \frac{1}{Re_\tau}\left(\frac{\partial^2}{\partial z^2} - |\kappa|^2\right)\hat{\boldsymbol{u}}(\boldsymbol{\kappa}, z, t) + \widehat{\boldsymbol{F}}(\boldsymbol{\kappa}, z, t) \tag{2.19}$$

where $\widehat{\boldsymbol{F}}$ is the Fourier transform of the forcing $\boldsymbol{F} = [-1, 0, 0]$ due to the mean pressure gradient applied in the streamwise direction, and $\hat{\boldsymbol{N}}$ is the Fourier transform of the sum of the advection and pressure terms.

The analog for a state variable q in wavenumber space, $q(\boldsymbol{\kappa}, z)$, for $\boldsymbol{\kappa} = 0$ is a plane-averaged mean $\langle q \rangle_{x,y}(z)$ in physical space; thus, the zero mode is associated with the mean, while the non-zero modes are associated with the turbulent fluctuations (Domaradzki et al., 1994). Therefore, Equation (2.19) is equivalent to the evolution equation for the mean velocity, Equation (2.12), for $\boldsymbol{\kappa} = 0$, and the evolution of the velocity fluctuations, Equation (2.13), for $\boldsymbol{\kappa} \neq 0$.

The turbulent kinetic energy balance can also be represented in wavenumber space. The energy amplitude is defined by $E(\boldsymbol{\kappa}, z) = \frac{1}{2}\hat{\boldsymbol{u}}(\boldsymbol{\kappa}, z)\hat{\boldsymbol{u}}^*(\boldsymbol{\kappa}, z)$, where the asterisk $(*)$ denotes the complex conjugate. It follows that

$$\begin{aligned}\partial_t E(\boldsymbol{\kappa}, z) = \Re\left[\hat{\boldsymbol{u}}^*(\boldsymbol{\kappa}, z)\hat{\boldsymbol{F}}(\boldsymbol{\kappa}, z)\right] + \Re\left[\hat{\boldsymbol{u}}^*(\boldsymbol{\kappa}, z)\hat{\boldsymbol{N}}(\boldsymbol{\kappa}, z)\right] + \frac{1}{Re_\tau}\frac{\partial^2}{\partial z^2}E(\boldsymbol{\kappa}, z) \\ - \frac{2}{Re_\tau}|\kappa|^2 E(\boldsymbol{\kappa}, z) - \frac{1}{Re_\tau}\left(\frac{\partial}{\partial z}\hat{\boldsymbol{u}}(\boldsymbol{\kappa}, z)\right)\left(\frac{\partial}{\partial z}\hat{\boldsymbol{u}}^*(\boldsymbol{\kappa}, z)\right)\end{aligned} \tag{2.20}$$

where $\Re$ indicates the real part of a complex quantity and time dependence of the flow fields are assumed. The five terms on the right hand side of Equation (2.20) (from left to right) represent production, nonlinear energy transfer (including pressure transport), energy redistribution by the viscous stresses, and viscous dissipation. Equation (2.20) is therefore equivalent to Equation (2.15).

2.4 Turbulence metrics

Since the primary objective of this work is to determine the effectiveness of the GQL approximation, this section provides a brief overview of the metrics used to compare the

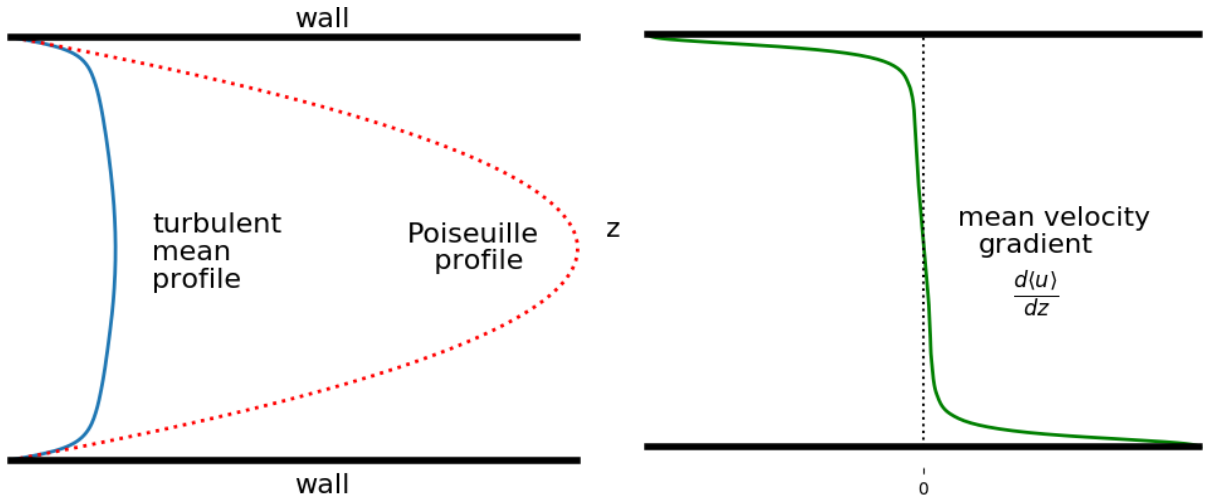

(a) (b)

Figure 2.4: (a) Turbulent mean versus laminar mean velocity profiles and (b) mean velocity gradient profile in a channel.

results obtained under the various approximation schemes discussed in Chapter 1 to the results of the fully nonlinear simulations.

Mean velocity profiles

Figure 2.4a shows a streamwise velocity profile in a fully-developed laminar channel flow and the corresponding time-averaged streamwise velocity profile in fully-developed turbulent channel flow. Recall that for prescribed, constant pressure gradient, the velocity gradient at the wall is fixed. Figure 2.4b shows the corresponding mean velocity gradient profile (alternatively called the mean shear profile).

Reynolds stresses

Reynolds stresses, introduced briefly in Section 2.3.1, originate from the quadratic nonlinearity in Equation (2.4) following Reynolds decomposition and averaging, and physically represent the transfer of momentum by the fluctuating velocity field, coupling the mean flow to the turbulence (Pope, 2000; Davidson, 2015). Since the QL and GQL algorithms neglect certain nonlinear interactions, it is of primary importance to determine how the approximate

Reynolds stress profiles differ from those in the fully nonlinear case. This analysis will serve as one good indicator of the accuracy of the model and can also provide insight into the effect of neglecting particular nonlinear interactions.

It is convenient to express the tensorial Reynolds stresses as components in Cartesian notation. Equating $u'_1 = u'$, $u'_2 = v'$, and $u'_3 = w'$, the Reynolds stress tensor can be expressed as

$$\langle u'_i u'_j \rangle = \begin{bmatrix} \langle u'^2 \rangle & \langle u'v' \rangle & \langle u'w' \rangle \\ \langle v'u' \rangle & \langle v'^2 \rangle & \langle v'w' \rangle \\ \langle w'u' \rangle & \langle w'v' \rangle & \langle w'^2 \rangle \end{bmatrix} \tag{2.21}$$

The turbulent kinetic energy from Equation (2.15) is defined as half the trace of the Reynolds stress tensor. The normal Reynolds stresses, the wall-normal component of the shear stress, $\langle u'w' \rangle$, and the turbulent kinetic energy have been well-characterized in turbulent channel flow and are shown graphically for the inner layer in Figure 2.5 as a function of wall units. Note the wall-normal location of peak amplitude and relative difference in magnitude for each of the Reynolds stress components shown, as well as the rate at which each increases from zero.

Turbulent velocity fluctuations

The strength of a turbulent flow is commonly quantified by computing the root-mean-square (rms) of the velocity fluctuations, given by

$$(u'_{rms}, v'_{rms}, w'_{rms}) = \left(\sqrt{\langle u'^2 \rangle}, \sqrt{\langle v'^2 \rangle}, \sqrt{\langle w'^2 \rangle} \right) \tag{2.22}$$

By definition, Equation (2.22) gives the standard deviation of each fluctuating velocity component. In channel flow, u'^+_{rms} has a distinct peak at $z^+ = 15$, and reaches a local minimum at the centerline, as shown in Figure 2.6.

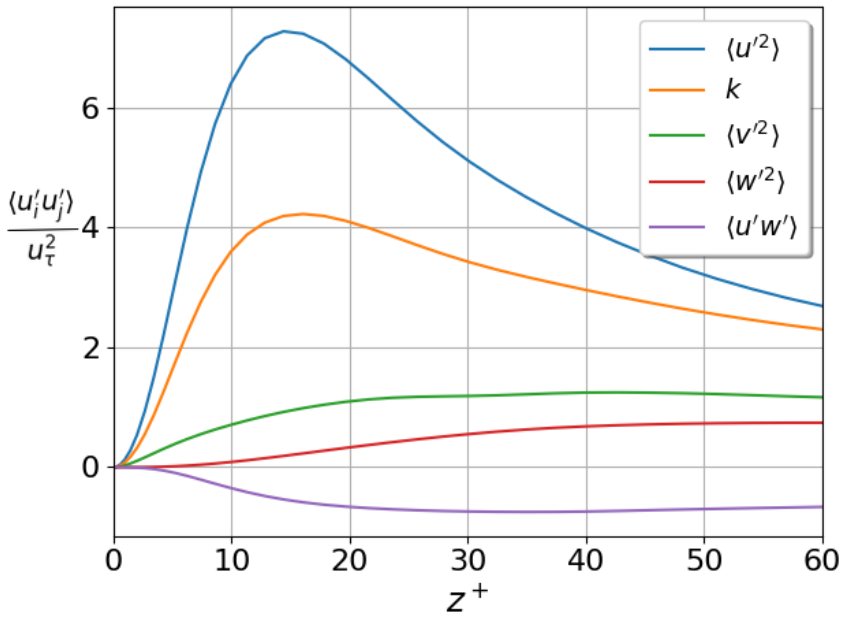

Figure 2.5: Reynolds stress profiles extracted from a DNS of turbulent channel flow at $Re_\tau = 200$ in the (nondimensional) spatial domain $[2\pi, \pi, 2]$.

Anisotropy

As briefly discussed in Chapter 1, turbulence in wall-bounded shear flows is anisotropic and inhomogeneous. An effective way to characterize the anisotropy of turbulent channel flow is by way of the Lumley triangle. Recall for a stress tensor, the diagonal components represent the normal stresses, while the off-diagonal components are the shear stresses. The shear stresses are related to the shear deformation of a parcel of fluid, but the values are dependent on the coordinate system. In contrast, tensor invariants (scalars), or eigenvalues of the stress tensor, do not depend on the coordinate system. Using the invariants of the Reynolds stress tensor, every realizable Reynolds stress state (i.e., having non-negative and non-complex eigenvalues) corresponds to a location on the Lumley triangle (Pope, 2000).

Expressing the Reynolds stress tensor, defined previously by Equation (2.21), as a sum of symmetric and antisymmetric parts, and normalizing by the turbulent kinetic energy

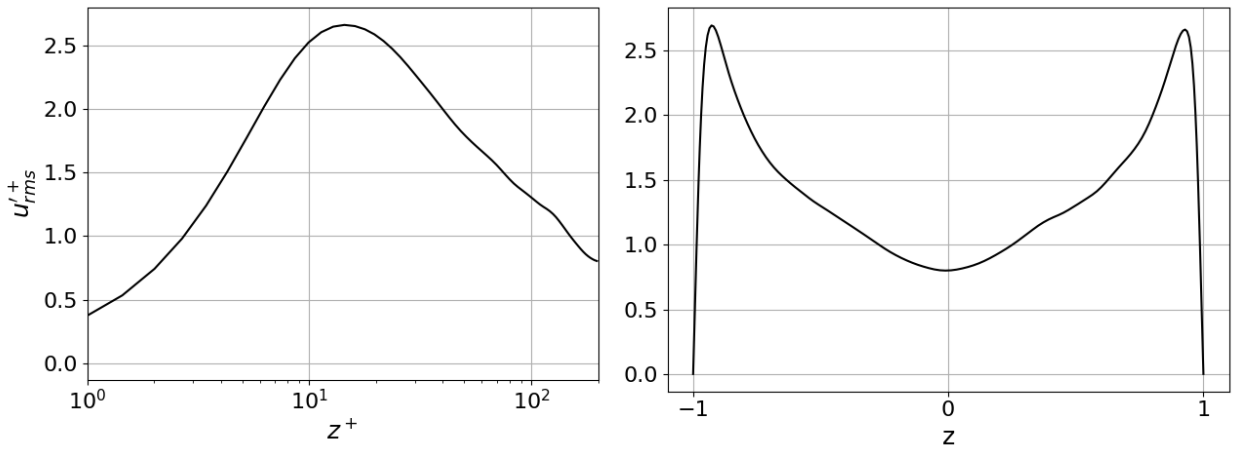

Figure 2.6: Root-mean-square of the streamwise velocity fluctuation taken from DNS data of turbulent channel flow at $Re_\tau = 200$.

$k = \frac{1}{2}\langle u_i' u_i' \rangle$, the normalized Reynolds stress stress anisotropy tensor b_{ij} is defined as

$$b_{ij} = \frac{\langle u_i' u_j' \rangle}{\langle u_\ell' u_\ell' \rangle} - \frac{1}{3}\delta_{ij} = \frac{a_{ij}}{2k} \tag{2.23}$$

where a_{ij} is the antisymmetric part of the Reynolds stress tensor. From linear algebra, the three principal invariants of $\boldsymbol{B}$ are therefore

$$I_1 = b_{ii} = \mathrm{tr}(\boldsymbol{B}) \tag{2.24}$$

$$I_2 = \frac{1}{2}\left[(b_{ii})^2 - b_{ii}^2\right] = \frac{1}{2}\left[(\mathrm{tr}(\boldsymbol{B}))^2 - \mathrm{tr}(\boldsymbol{B}^2)\right] \tag{2.25}$$

$$I_3 = \frac{1}{6}(b_{ii})^3 - \frac{1}{2}b_{ii}b_{jj}^2 + \frac{1}{3}b_{ii}^3 = \det(\boldsymbol{B}) \tag{2.26}$$

Since the Reynolds stress anisotropy tensor is antisymmetric, $\mathrm{tr}(\boldsymbol{B}) = 0$, thus Equation (2.24) always restricts $I_1 = 0$. Therefore, the state of anisotropy can be completely characterized by two invariants. Though I_2 and I_3 can be used, it is convenient to define the two independent invariants, η and ξ, as

$$6\eta^2 = -2I_2 = b_{ii}^2 \tag{2.27}$$

$$6\xi^3 = 3I_3 = b_{ii}^3 \tag{2.28}$$

Equation (2.27) and Equation (2.28) define the coordinate axes (ξ, η) of the Lumley

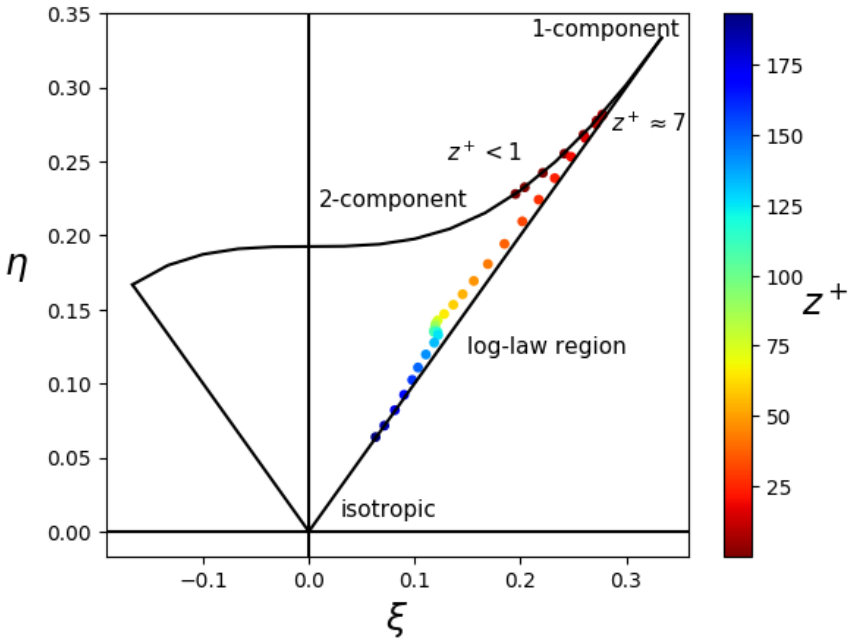

Figure 2.7: Lumley triangle with data from DNS of channel flow, where the color map indicates distance from the wall in inner units (adapted from Figure 11.1 in Pope (2000)).

triangle using the Reynolds stress tensor. It should be noted that a similar figure can be made by plotting I_2 and I_3 instead of ξ and η, which merely results in different boundaries of the triangle. The special states of the Reynolds stress tensor are unchanged, but it can be more difficult to ascertain how close the data is to these boundaries.

The vertical axis η measures the degree of anisotropy, starting with fully isotropic at the origin. Data from a DNS of channel flow generated in this study is shown on the Lumley triangle in Figure 2.7. Due to no-slip boundary conditions, continuity requires that $\partial v'/\partial z = 0$ at each wall. Through Taylor series expansion of the fluctuating velocity, it can be shown that, near the wall, there exists two-component flow (Pope, 2000). Away from the wall but still in the near-wall region, the flow is dominated by streaks which can be modeled as one-component flow. For high enough Reynolds number, there is a region of constant anisotropy in the log-law region, and near the center of the channel, the flow tends to be more isotropic. Therefore, a good approximation method should be able to reproduce these characteristic features in the appropriate regions of the flow.

Strain and vorticity fields

Though still not completely understood, the relationship between the structure of the turbulent strain field and the vorticity field plays a central role in deciphering how dissipation is distributed spatially in the flow and in modeling vortex stretching (Davidson, 2015). Pioneered by Chong et al. (1990) and Cantwell (1993), the construction of a joint probability density function (pdf) of the invariants of the velocity gradient tensor provides statistical information about the local dynamics and topology of a turbulent flow, particularly the interplay between the strain and vorticity fields (Khashehchi et al., 2009). It follows from the same methodology used to construct the invariants of the Reynolds stress tensor that the invariants of the total velocity gradient tensor, L_{ij}, are

$$P = L_{ii} = Tr(\boldsymbol{L}) \tag{2.29}$$

$$Q = -\frac{1}{2}L_{ij}L_{ij} = -\frac{1}{2}Tr(\boldsymbol{L^2}) \tag{2.30}$$

$$R = -\frac{1}{3}L_{ij}L_{jk}L_{ki} = -\frac{1}{3}Tr(\boldsymbol{L^3}) \tag{2.31}$$

For incompressible flows, continuity requires $P = 0$. Written in terms of the symmetric and anti-symmetric parts of the total velocity gradient tensor, S_{ij} and W_{ij} respectively, the second and third invariants are

$$Q = \frac{1}{4}\boldsymbol{\omega}^2 - \frac{1}{2}S_{ij}S_{ji} \tag{2.32}$$

$$R = -\frac{1}{3}(S_{ij}S_{jk}S_{ki} + \frac{3}{4}\omega_i\omega_j S_{ij}) \tag{2.33}$$

where energy dissipation rate, $\epsilon = 2\nu S_{ij}S_{ij}$, measures the magnitude of S_{ij}, $\frac{1}{2}\omega_i\omega_i$ measures the magnitude of A_{ij}, and $\boldsymbol{\omega}$ is the vorticity field.

The Q-R invariants are well-studied in a variety of turbulent flows yielding some universal features, including the characteristic "teardrop" shape of the joint pdf. Broadly, large negative values of Q correspond to regions of high strain and low vorticity, while large positive values of Q indicate regions where vorticity is dominant and strain is weak (Davidson,

2015). While the finer details are not in the scope of this work, the Q-R invariants will be used to gauge the effectiveness of the GQL approximation in recovering certain statistical aspects of the dynamics and topology of fully turbulent flow.

Chapter 3

Algorithms Employed

In this chapter, the analytical details of the quasilinear and generalized quasilinear approximation of the Navier-Stokes equations and the associated numerical methods used to implement the two algorithms central to this work are described. The first algorithm, written in MATLAB, solves the single-mode quasilinear equations only, while the second algorithm, written in Python and utilizing the Dedalus spectral framework (Burns et al., 2019), can operate in four modalities: SMQL, QL, GQL, and fully nonlinear (NL).

3.1 Single-mode quasilinear algorithm

The QL approximation is a well-established theory in which nonlinear fluctuation/fluctuation interactions are retained only when they feed back onto the mean dynamics. As a step toward the development of a GQL algorithm for turbulent channel flow, a QL algorithm was developed in MATLAB with the specific intent of reducing the fully 3D problem to a "$2+\epsilon$"-dimensional simulation by retaining only a *single* streamwise fluctuation mode. The results obtained from the SMQL algorithm developed in MATLAB also provide an external validation for a SMQL simulation performed using the Python code.

3.1.1 System of equations

Recall from Chapter 2 the dimensionless equations governing plane Poiseuille flow are

$$\begin{cases} \partial_t \boldsymbol{u} + \boldsymbol{u} \cdot \nabla \boldsymbol{u} = -\nabla p + \frac{1}{Re_\tau} \nabla^2 \boldsymbol{u} - 1\hat{x} \\ \nabla \cdot \boldsymbol{u} = 0 \\ \boldsymbol{u} = (u, v, w) = (0, 0, 0) \text{ at } z = \pm 1 \end{cases} \tag{3.1}$$

To derive the SMQL algorithm, the first step (as for QL) is to decompose the state variables into a suitable mean and a fluctuation about the mean. In the self-sustaining process described by Waleffe (1997), the instability of the streamwise streaks plays an integral role in the sustenance of turbulence. It is therefore reasonable to linearize the governing equations about the streamwise-averaged streaks, implying the state variables are decomposed into a *streamwise* (x) mean and fluctuation about the mean, such that

$$\boldsymbol{U}(y, z, t) := \langle \boldsymbol{u}(x, y, z, t) \rangle_x \quad P(y, z, t) := \langle p(x, y, z, t) \rangle_x \tag{3.2}$$

$$\boldsymbol{u}(x, y, z, t) = \boldsymbol{U}(y, z, t) + \boldsymbol{u'}(x, y, z, t) \tag{3.3}$$

$$p(x, y, z, t) = P(y, z, t) + p'(x, y, z, t) \tag{3.4}$$

where, accordingly, the prime notation here denotes the fluctuations about the x-mean. Substituting into Equation (3.1) and parsing into mean and fluctuation components yields

$$\partial_t \boldsymbol{U} + \boldsymbol{U} \cdot \nabla \boldsymbol{U} - 1\widehat{\boldsymbol{x}} + \nabla P - \frac{1}{Re_\tau} \nabla^2 \boldsymbol{U} = -\langle \boldsymbol{u'} \cdot \nabla \boldsymbol{u'} \rangle_x \tag{3.5}$$

$$\partial_t \boldsymbol{u'} + \boldsymbol{U} \cdot \nabla \boldsymbol{u'} + \boldsymbol{u'} \cdot \nabla \boldsymbol{U} + \nabla p' - \frac{1}{Re_\tau} \nabla^2 \boldsymbol{u'} = -(\boldsymbol{u'} \cdot \nabla \boldsymbol{u'} - \langle \boldsymbol{u'} \cdot \nabla \boldsymbol{u'} \rangle_x) \tag{3.6}$$

The QL approximation is obtained by keeping only the fluctuation-fluctuation interactions that feed back onto the mean. Neglecting the right-hand side of Equation (3.6) and rearranging results in

$$\partial_t \boldsymbol{u'} + \boldsymbol{U} \cdot \nabla \boldsymbol{u'} + \boldsymbol{u'} \cdot \nabla \boldsymbol{U} = -\nabla p' + \frac{1}{Re_\tau} \nabla^2 \boldsymbol{u'} \tag{3.7}$$

The QL system described by Equations (3.5) and (3.7) is identical to the RNL model

used by Farrell et al. (2016).

It proves convenient to eliminate the pressure gradient from Equations (3.5) and (3.7). Since the mean velocity is independent of x, a streamfunction-vorticity formulation can be employed to eliminate the mean pressure gradient from Equation (3.5), yielding

$$\partial_t \Omega - \partial_z \Psi \partial_y \Omega + \partial_y \Psi \partial_z \Omega = \frac{1}{Re} \nabla_\perp^2 \Omega - \partial_y (\langle \boldsymbol{u}' \cdot \boldsymbol{\nabla} w' \rangle_x) + \partial_z (\langle \boldsymbol{u}' \cdot \boldsymbol{\nabla} v' \rangle_x) \tag{3.8a}$$

$$\nabla^2 \Psi = \Omega \qquad V = -\partial_z \Psi \qquad W = \partial_y \Psi \tag{3.8b}$$

where Ω is the mean x-vorticity component and Ψ is the mean streamfunction. The fluctuating pressure is eliminated by employing the normal-velocity/normal-vorticity method introduced by Kim et al. (1987), in which the fluctuating momentum and continuity equations are reformulated into a fourth-order equation for the normal velocity, w', and a second-order equation for the normal component of the fluctuating vorticity, g'. This results in the system

$$\partial_t \nabla^2 w' = n_w' + \frac{1}{Re_\tau} \nabla^4 w' \tag{3.9a}$$

$$\partial_t g' = n_g' + \frac{1}{Re_\tau} \nabla^2 g' \tag{3.9b}$$

$$0 = f' + \partial_z w' \tag{3.9c}$$

where

$$f' = \partial_x u' + \partial_y v'$$

$$g' = \partial_x v' - \partial_y u'$$

$$n_w' = \partial_z (\partial_x N_1 + \partial_y N_2) - (\partial_x^2 + \partial_y^2) N_3$$

$$n_g' = \partial_x N_2 - \partial_y N_1$$

N_1, N_2, N_3 represent the advection terms in Equation (3.7):

$$N_1 = \bar{u}\partial_x u' + \bar{v}\partial_y u' + v'\partial_y \bar{u} + \bar{w}\partial_z u' + w'\partial_z \bar{u}$$

$$N_2 = \bar{u}\partial_x v' + \bar{v}\partial_y v' + v'\partial_y \bar{v} + \bar{w}\partial_z v' + w'\partial_z \bar{v}$$

$$N_3 = \bar{u}\partial_x w' + \bar{v}\partial_y w' + v'\partial_y \bar{w} + \bar{w}\partial_z w' + w'\partial_z \bar{w}$$

3.1.2 Numerical method

The system of equations made up of Equations (3.5), (3.8) and (3.9) with boundary conditions Equation (3.1) can be solved using a pseudo-spectral method for the spatial derivatives. Specifically, a Fourier series expansion is employed in the streamwise and spanwise directions, and a Chebyshev polynomial expansion is utilized in the wall-normal direction (Trefethen, 2000). Thus, the mean and fluctuating velocity fields can be approximated using the truncated Fourier expansions

$$\boldsymbol{U}(y,z,t) = \sum_{k_x=-\frac{N_x}{2}+1}^{N_x/2} \hat{\boldsymbol{U}}(k_y,z,t) e^{i\frac{2\pi k_y}{L_y}y} \tag{3.10}$$

$$\boldsymbol{u'}(x,y,z,t)) = \sum_{k_x=-\frac{N_x}{2}+1}^{N_x/2} \sum_{k_y=-\frac{N_y}{2}+1}^{N_y/2} \hat{\boldsymbol{u}}'(k_x,k_y,z,t) e^{i\frac{2\pi k_x}{L_x}x + i\frac{2\pi k_y}{L_y}y} \tag{3.11}$$

where k_x and k_y are the streamwise and spanwise mode numbers respectively. In the QL approximation, $\boldsymbol{U}$ represents the mean flow components (i.e., associated only with the $k_x = 0$ mode number). Pressure is similarly defined. The code is advanced in time using a semi-implicit scheme (Crank-Nicolson for the linear terms and second-order Adams-Bashforth for the nonlinear terms). An influence matrix method is used to enforce the boundary conditions associated with Equations (3.8) and (3.9a). The SMQL algorithm is realized by retaining only a single (non-zero) streamwise Fourier component, which is chosen based on the length of the streamwise domain L_x. This reduction to a "2+ϵ"-dimensional simulation dramatically

reduces the computational cost while still sustaining nonlinear dynamics (Bretheim et al., 2018).

3.2 GQL algorithm

While SMQL and other variations (constrained RNL, RNL, and QL, where a discrete spectrum of streamwise fluctuation modes is retained) have been shown to qualitatively recover low-order statistics of the turbulent dynamics, the suppression of energy scatter among fluctuation modes can lead to inaccuracies in the fine-scale structure of the flow and even in the long-time and horizontally-averaged mean velocity profile (Marston et al., 2016; Tobias and Marston, 2017). The GQL approximation addresses the severe restriction on the allowable small-scale energy scatter by permitting fully nonlinear interactions among modes with non-zero streamwise wavenumber. Crucially, even when a single additional low mode is retained, spectrally non-local energy transfers among the fluctuation (i.e., high) modes are enabled, yielding improved recovery of the small-scale flow structure. To this end, a more robust coding language and a more efficient solver proved necessary. Accordingly, the algorithm developed in this section has the capability of operating in four modalities, *viz.*, SMQL, QL, GQL, and fully nonlinear (NL), facilitating a comparative study of these approaches.

3.2.1 System of equations

In the SMQL/QL algorithm, the state variables are decomposed into a strict streamwise mean and fluctuations about the mean. To generalize this decomposition, the velocity vector and pressure are decomposed instead into large-scale and small-scale components, such that

$$\boldsymbol{u} = \boldsymbol{u}_\ell + \boldsymbol{u}_h \tag{3.12}$$

where ℓ and h represent the "low" and "high" wavenumber modes respectively. Low-wavenumber modes are associated with large-scale motions and high-wavenumber modes are associated

with small-scale motions. Physically, under the GQL reduction, the large-scale motions are permitted to interact nonlinearly, while the dynamics of the small-scale motions is determined by linearization about the large-scale motions.

A Fourier series representation is again used for $\boldsymbol{u}_\ell$ and $\boldsymbol{u}_h$,

$$\boldsymbol{u}_\ell(x,y,z,t) = \sum_{k_x=-\Lambda_x}^{\Lambda_x} \sum_{k_y=-\Lambda_y}^{\Lambda_y} \hat{\boldsymbol{u}}(k_x,k_y,z,t) e^{i\frac{2\pi k_x}{L_x}x + i\frac{2\pi k_y}{L_y}y} \tag{3.13}$$

$$\boldsymbol{u}_h = \boldsymbol{u} - \boldsymbol{u}_\ell \tag{3.14}$$

where Λ_x and Λ_y are the spectral cutoff mode numbers that separate the low and high modes in the indicated spatial direction. It is possible to perform GQL in both homogeneous directions, as demonstrated by Tobias and Marston (2017). In this work, however, only the nonlinear interactions in the streamwise (x) direction were restricted, allowing fully nonlinear interactions in the spanwise (y) direction for all cases. The separation in wave-vector space is shown schematically in Figure 3.1a. It is important to note that the imposition of a spectral cutoff does not eliminate modes; rather it simply restricts nonlinear interactions. This distinction should be a recalled when assessing the computational efficiency of the simulation.

Substituting the modal decomposition into Equation (2.4) and projecting onto low and high modes yields, respectively,

$$[\boldsymbol{u}_\ell]_t = \mathcal{L}(\boldsymbol{u}_\ell) + \mathcal{N}_\ell(\boldsymbol{u}_h,\boldsymbol{u}_h) + \mathcal{N}_\ell(\boldsymbol{u}_\ell,\boldsymbol{u}_\ell) + \mathcal{N}_\ell(\boldsymbol{u}_\ell,\boldsymbol{u}_h) + \mathcal{N}_\ell(\boldsymbol{u}_h,\boldsymbol{u}_\ell) \tag{3.15}$$

$$[\boldsymbol{u}_h]_t = \mathcal{L}(\boldsymbol{u}_h) + \mathcal{N}_h(\boldsymbol{u}_\ell,\boldsymbol{u}_h) + \mathcal{N}_h(\boldsymbol{u}_h,\boldsymbol{u}_\ell) + \mathcal{N}_h(\boldsymbol{u}_h,\boldsymbol{u}_h) + \mathcal{N}_h(\boldsymbol{u}_\ell,\boldsymbol{u}_\ell) \tag{3.16}$$

where $\mathcal{L}$ is a linear vector differential operator and $\mathcal{N}$ is an operator that contains the nonlinear interactions in the governing PDE.

The GQL approximation is realized by retaining only specific nonlinear interactions *a priori*. In Equation (3.15), only the nonlinear interactions between low modes and low modes and high modes and high modes that result in low modes are retained. In Equation (3.16), the nonlinear interactions between the low modes and high modes that result in high modes

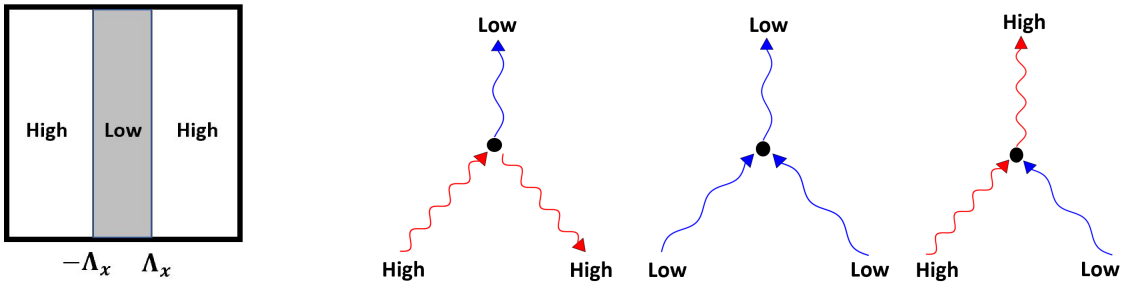

(a) (b)

Figure 3.1: (a) Separation in wave-vector space of modes into "low" and "high" components employed in this work and (b) the set of retained triadic interactions in the GQL approximation (Tobias and Marston, 2017).

are retained. The retained nonlinear interactions are shown schematically in Figure 3.1b. All other nonlinear interactions are neglected. It is emphasized here that, as is also the case with QL, the nonlinear interactions retained in the GQL algorithm obey the conservation laws of the original PDE (Marston et al., 2016). The GQL approximation is expressed as

$$\partial_t \boldsymbol{u}_\ell = \mathcal{L}(\boldsymbol{u}_\ell) + \mathcal{N}_\ell(\boldsymbol{u}_h, \boldsymbol{u}_h) + \mathcal{N}_\ell(\boldsymbol{u}_\ell, \boldsymbol{u}_\ell) \tag{3.17}$$

$$\partial_t \boldsymbol{u}_h = \mathcal{L}(\boldsymbol{u}_h) + \mathcal{N}_h(\boldsymbol{u}_\ell, \boldsymbol{u}_h) + \mathcal{N}_h(\boldsymbol{u}_h, \boldsymbol{u}_\ell) \tag{3.18}$$

If the spectral cutoff $\Lambda_x = 0$ (i.e., the only low mode retained is $k_x = 0$), the last two nonlinear interactions in Equation (3.15) and the last nonlinear interaction in Equation (3.16) are identically zero, and the quasilinear approximation described in Section 3.1 is recovered exactly. For Λ_x equal to the highest wavenumber (i.e., retained in a DNS), the fully nonlinear dynamics are recovered. Thus the GQL approximation effects a homotopy between QL and DNS.

3.2.2 Numerical method

The GQL system of equations described by Equations (3.17) and (3.18) has been coded in Python and solved using the Dedalus spectral framework for numerically simulating PDEs (Burns et al., 2019). Dedalus is an open-source spectral solver written in Python that simply requires the user to define a spectral domain, input systems of equations and boundary con-

ditions in plain text, and select a numerical solver from a database. Here, a pseudo-spectral (Fourier-Fourier-Chebyshev) method is used for the spatial derivatives and a third-order semi-implicit backward difference formula (SBDF3) is used to advance in time. Dedalus also allows for an adaptive timestep, which is used in all simulations. Simulations are performed on Premise, one of the University of New Hampshire's high performance computing clusters.

3.3 Resolution and parameter selection

In wall-bounded shear flows, the dynamics of the near-wall region is most sensitive to grid resolution. In general, the grid resolution used for channel flow DNS must meet the following conditions, as outlined by Ghiasi et al. (2018):

1. The first point (nearest the wall) is located within $z^+ < 1$.

2. There are at least 10 points within $z^+ < 10$.

A competing concern is that the smaller grid size near the wall associated with the staggered grid necessitates a smaller time step, which can be computationally expensive. Ghiasi et al. (2018) compared results of two simulations performed on grids with 11 and 5 grid points within $z^+ < 10$ in a turbulent channel flow using a Chebyshev distribution of points in the wall-normal direction. In both cases, the mean velocity profile is predicted accurately, but the second case (5 grid points) under-predicts the streamwise turbulence intensity. The investigators concluded that the second general condition is required to be satisfied for accurate prediction of flow statistics. This criterion is followed to determine whether the resolution chosen for the GQL simulations is adequate.

A guiding principle in determining a parameter regime for the GQL simulations involved choosing a sufficiently high Reynolds number to sustain turbulence beyond the transitional regime while enabling fully nonlinear simulations to be performed at reasonable computational cost for comparison. The domain size was then chosen to minimize computational cost yet sustaining turbulence. The initial resolution in the wall-normal direction met the

Trial	N_x x N_y x N_z	$[L_x, L_y, L_z]$	Re_τ
1	84 x 84 x 108	$[2\pi, \pi, 2]$	200
2	96 x 96 x 108		
3	96 x 96 x 128		
4	96 x 96 x 144		

Table 3.1: Selection of GQL simulation parameter regime.

requirements proposed by Ghiasi et al. (2018). Through trial and error, an initial parameter regime in which the fully nonlinear case sustained turbulence was achieved at a reasonable computational cost. Fixing the Reynolds number and domain size, several different grid resolutions were explored, as listed in Table 3.1.

Studying the wall-normal dependence of the statistics of the turbulent velocity gradient fields in wall-bounded flow has been shown to yield quantitative justification for choosing a particular grid resolution, as first discussed by Hamlington et al. (2012). Using this methodology, the vertical profiles of the energy dissipation rate were compared at all resolutions.

The energy dissipation rate, ϵ, is a measure of the magnitude of the symmetric strain rate tensor, S_{ij} (see Section 2.4). The variation of the energy dissipation rate with distance from the wall can be seen by plotting the average (in time and the horizontal plane) of the dimensionless energy dissipation rate, as a function of the wall-normal coordinate,

$$\epsilon_{avg}(z) = \langle \epsilon(\boldsymbol{x}, t) \rangle_{A,t} = \frac{2}{Re_\tau} \langle S_{ij} S_{ij} \rangle_{A,t} \tag{3.19}$$

where A is the area of the x-y plane.

The average energy dissipation rate, ϵ_{avg}, for all four resolutions is shown in Figure 3.2. The curves collapse throughout most of the channel, with slight deviations in the viscous layer, specifically near $z^+ \approx 20$. Based on the conclusions of Hamlington et al. (2012), the results indicate that any of the selected resolutions would yield accurate first-order statistics. Ultimately, the resolution yielding the most constant average energy dissipation rate near $z^+ \approx 20$, i.e., 96 x 96 x 144, was chosen because of the better agreement with the dissipation term in the turbulent kinetic energy budget (see Figure 2.3).

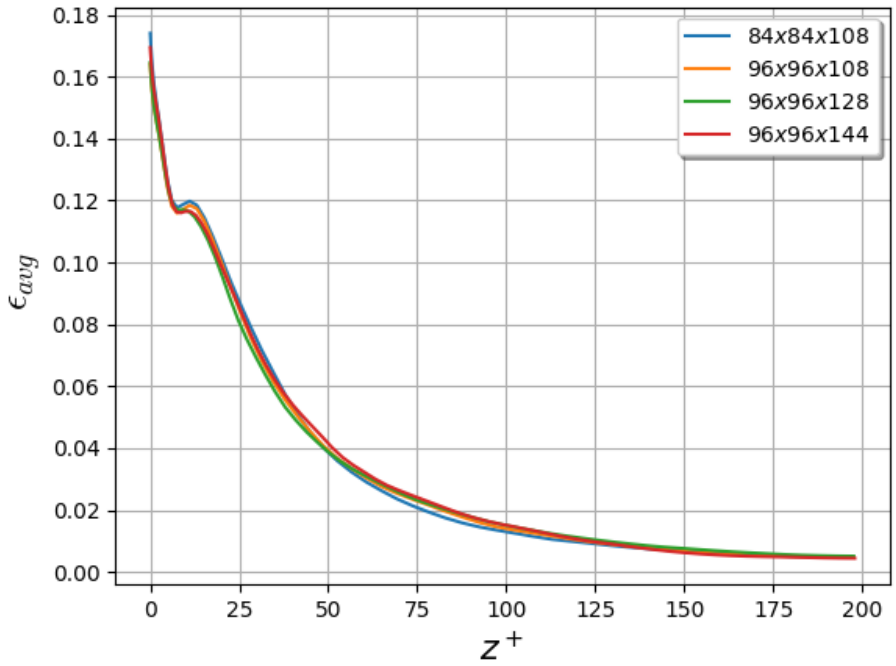

Figure 3.2: Average energy dissipation rate, ϵ_{avg}, for the different grid resolutions listed in Table 3.1.

To more quantitatively examine the adequacy of the grid resolution, the value of the spectral coefficients having the highest mode number ($k_x = N_x/2$, $k_y = \pm N_y/2$, and N_z) for each component of the velocity field, u, v, and w, was determined. Although the ideal truncation error is machine precision, there does not appear to be a consensus in the literature on the maximum error allowed for a direct numerical simulation to be considered "well-resolved". Anecdotal evidence suggests modal amplitudes on the order 10^{-4} to 10^{-6} for the Fourier directions and 10^{-6} to 10^{-9} for the Chebyshev direction yields a well-resolved simulation for the purposes of this work. Analysis of the high Reynolds number regime explored in this work indicates the maximum truncation of the Fourier coefficients is on the order of 10^{-4} for the streamwise and wall-normal velocity components and 10^{-5} for the spanwise velocity component. A similar analysis of the low Reynolds number regime selected in this study reveals the maximum truncation of the Fourier coefficients is on the order of 10^{-3} for all three velocity components. For the high Reynolds number regime, the

maximum truncation of the Chebyshev coefficients has an amplitude on the order 10^{-6} for the streamwise and spanwise velocities and 10^{-7} for the wall-normal velocity. For the low Reynolds number regime, the maximum truncation of the Chebyshev coefficients has an amplitude on the order 10^{-9} for the streamwise and spanwise velocities and 10^{-10} for the wall-normal velocity. These results suggest the fully nonlinear simulations for both Reynolds number regimes are adequately, albeit marginally, resolved for the purposes of the analysis in this work, but could be improved by increasing the resolution in all three spatial directions. This further refinement of the grids has not yet been performed owing to time constraints and computational hardware restrictions, but will be a consideration for future work.

Chapter 4

GQL Simulations at High Reynolds Number

In this chapter, the accuracy of GQL simulations for various values of Λ_x is evaluated by computing metrics introduced in Chapter 2 and performing head-to-head comparisons with QL and the fully nonlinear simulation for the same set of parameters. It will be demonstrated that GQL, even with a modest spectral cutoff ($\Lambda_x \leq 3$), is able to more accurately reproduce the statistics and dynamics of a fully nonlinear turbulent channel flow than is QL.

4.1 Parameter regime and data collection

To establish the accuracy of the GQL approximation, the system parameters were chosen so that a self-sustaining turbulent flow regime could be attained *and* the fully nonlinear dynamics could be feasibly simulated for comparison. Table 4.1 lists the parameters used for all simulations. In total, eight simulations were run: one QL, one NL, and six GQL simulations for various values of Λ_x. The fully nonlinear simulation was initialized with the parabolic Poiseuille velocity profile with random perturbations to trigger turbulence and then run to a statistically steady state. All GQL simulations and the QL simulation were initialized from the NL statistically steady state and run for at least 350 non-dimensional time units. Data is saved every 0.5 non-dimensional time units for all simulations and averaged for purposes of analysis over the last 200 non-dimensional time units, yielding 400 "snapshots" for each simulation. In this section, the mean is defined as the time and horizontal spatial average. A mean quantity will be denoted with capital letters (e.g., $\langle \boldsymbol{u} \rangle_{x,y,t} = \boldsymbol{U}(z)$) and

Cases		$[L_x, L_y, L_z]$	N_x x N_y x N_z	Re_τ
$\Lambda_x = 0$	QL	$[2\pi, \pi, 2]$	96 x 96 x 144	200
$\Lambda_x = 2$	GQL2			
$\Lambda_x = 3$	GQL3			
$\Lambda_x = 8$	GQL8			
$\Lambda_x = 10$	GQL10			
$\Lambda_x = 15$	GQL15			
$\Lambda_x = 20$	GQL20			
$\Lambda_x = 48$	NL			

Table 4.1: GQL simulation parameters.

prime notation again indicates the fluctuations about the mean. Note that, in many cases, quantities were not averaged in the streamwise direction because the data was obtained from vertical plane snapshots at $x = 0$, indicated by $\langle\cdot\rangle_{y,t}$. The data obtained in the vertical (y-z) plane was more temporally resolved than the data for the entire channel by a factor of 20, and therefore was deemed to provide a better statistical representation of these quantities.

4.2 Results and analysis

Mean velocity and mean shear

In turbulent channel flow, the mean profile is the result of a redistribution of vorticity, which forms a region of weak shear in the core and matching regions of strong shear near the walls (Tobias and Marston, 2017; Waleffe et al., 1993). A comparison of the mean velocity and mean shear profiles under the QL and GQL approximations relative to those of the NL simulation is one indication of the model's ability to capture the nonlinear dynamics of the flow. The streamwise mean velocity profile, $U(z)$, and the mean velocity gradient, $\frac{dU}{dz}$, for each simulation identified in Table 4.1 were computed and are plotted in Figure 4.1 as functions of wall-normal distance. The parabolic Poiseuille profile is also included for reference. The line styles used to distinguish the different simulations will be consistent throughout, with the results from the NL simulation always represented by a thick dashed black line, the QL simulation represented by a dashed-dotted blue line, and the GQL simulations rep-

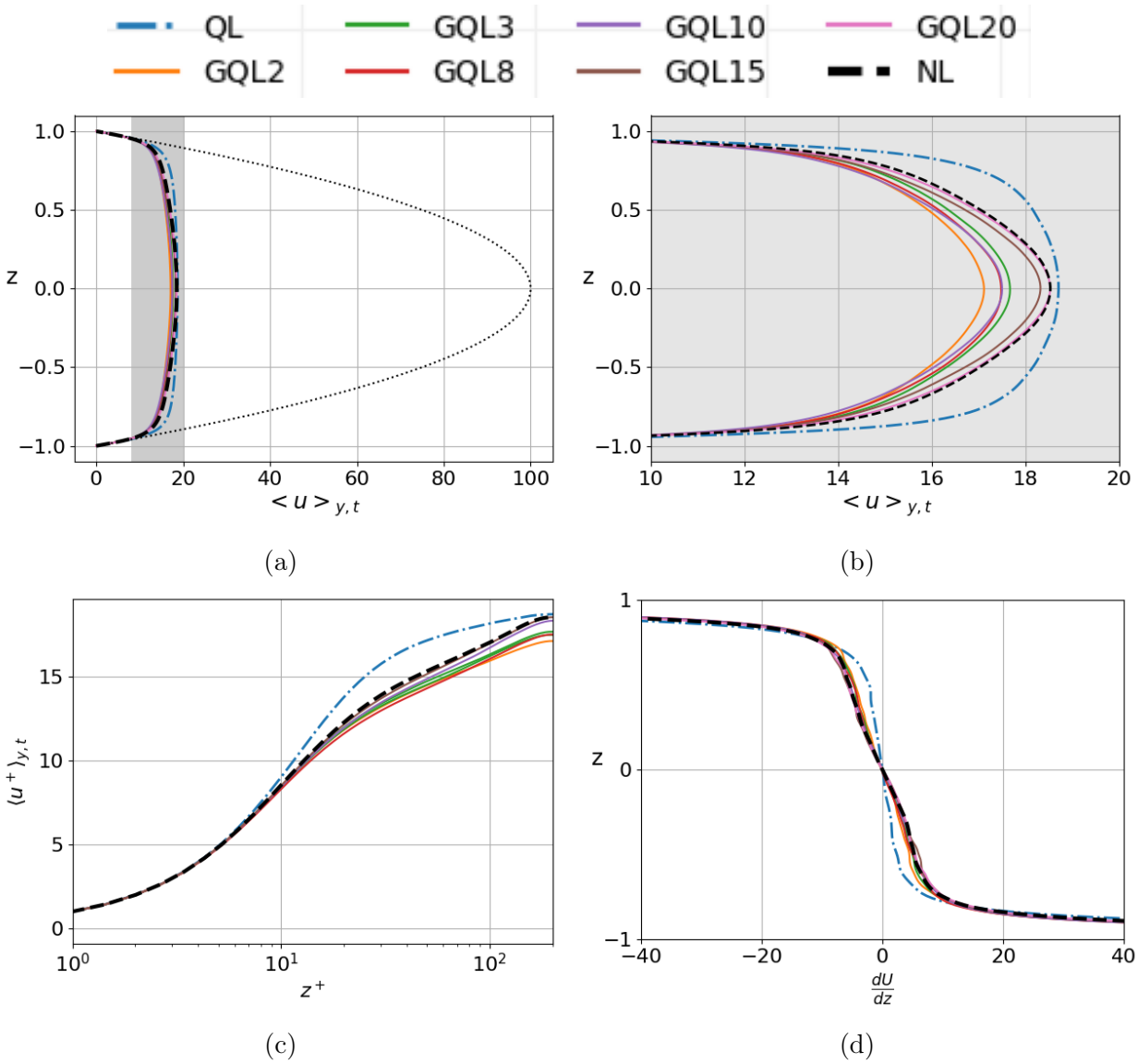

Figure 4.1: Streamwise mean velocity profiles (a) with laminar Poiseuille profile and turbulent mean profiles highlighted by the gray shaded region, (b) blow-up of turbulent streamwise mean velocity profiles, (c) the inner-normalized mean on a semi-log plot, and (d) the mean velocity gradient for all simulations. The color coding shown in the legend above this figure is consistently used throughout this work.

resented by the colors shown in the legend above Figure 4.1.

Figure 4.1a provides visual confirmation that all simulations are in the turbulent regime, indicated by the gray region. Zooming in on the turbulent mean profiles in Figure 4.1b, the QL approximation is demonstrably the least effective at reproducing the NL mean profile, while the GQL profiles are quantitatively more accurate in shape and magnitude, even at

a modest cutoff Λ_x. The GQL simulations, while showing good agreement with the NL mean shear profiles, do have varying degrees of accuracy in recovering the NL mean velocity profile. It is interesting, as noted by Child et al. (2016), that the improvement in accuracy of GQL3 over QL is significant, but increasing Λ_x further yields diminishing returns in the approach to the fully nonlinear first-order statistics. Both observations are consistent with the conclusions of prior investigators who employed GQL in two-dimensional and three-dimensional simulations of other flows and flow regimes (Marston et al., 2016; Child et al., 2016; Tobias and Marston, 2017).

The disparity between the mean profiles is more clearly seen in Figure 4.1c, where the mean and wall-distance are inner-normalized and compared on a semi-log plot. QL over-predicts the mean velocity in the NL log region and is drag-reduced, while all GQL simulations are slightly drag increased. Figure 4.1d demonstrates that the mean shear profiles obtained from the GQL simulations are in good agreement with the NL velocity gradient profile, while the QL simulation over-predicts the mixing in the core and, as a result, underestimates the shear in the core. This result is significant, as the mean shear is the energy source for the turbulence.

A more careful analysis of the mean velocity profiles provides information about the important dynamics of the log region. The log region of the flow is perhaps best identified using the indicator function, $z^+ dU^+/dz^+$, which is shown for all simulations in Figure 4.2. The value of the indicator function in the region between the peak of the Reynolds stress ($z^+ \approx 30$) to the outer edge of the inertial layer ($z \approx 0.2Re_\tau$, $z^+ \approx 40$) corresponds to the slope of the log region, defined as $1/\kappa = 2.5$, where $\kappa = 0.4$ is the well-established von Kármán constant and is independent of Reynolds number. Indeed, the indicator function for NL exhibits a slope of approximately 2.5. Crucially, the indicator function for the GQL simulations also indicates the presence of a log layer, although the value of κ varies as a function of the spectral cutoff Λ_x. In contrast, the indicator function for the QL simulation results does not identify a log layer, an observation in apparent conflict with the conclusions

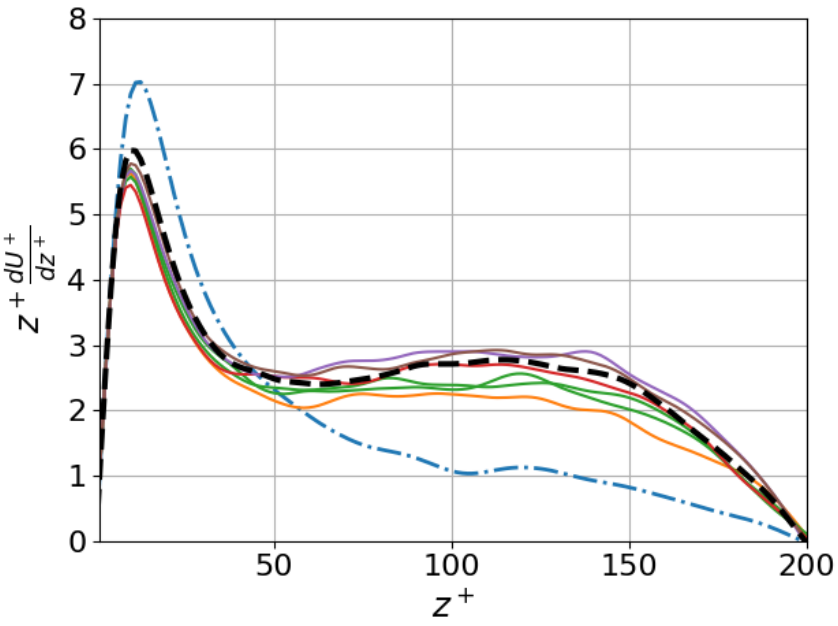

Figure 4.2: Indicator function. A log layer is clearly evident in all GQL profiles, as for the NL profile, but not in the QL simulation.

reached by Farrell et al. (2016) for channel flow at $Re_\tau = 940$. In this work, the absence of log-layer dynamics for the QL simulation is supported by other metrics reported later in this section, in particular the anisotropy analysis. It is significant that all GQL simulations, even those that retain a small number of low modes, recover the log-layer dynamics of the flow, while QL does not.

Instantaneous velocity fields

One advantage of using the GQL approximation rather than a statistical closure is that information about the instantaneous flow fields may be extracted. In Figure 4.3, the instantaneous streamwise velocity field for QL, GQL3, GQL8, and NL (from top to bottom) is shown in the horizontal (x-y) plane $z^+ = 10$ (left column), i.e., near the upper wall, and at $z = 0.1$ (right column), i.e., near the centerline, at one instant in time in the statistically steady regime. The characteristic streaky structures that form in the near-wall region can be seen in all simulations, while the fine-scale structure present in the NL simulation is

clearly evident even in the GQL3 and GQL8 simulations. By contrast, the QL simulation captures certain large-scale structure of the turbulent pattern but lacks the fine-scale streamwise structure present in NL. Additionally, the QL approximation yields larger streamwise velocities than NL. Near the centerline, all simulations reasonably recover the dynamics of NL, though here, too, the QL approximation overestimates the magnitude of the streamwise velocity.

The instantaneous streamwise velocity u in the transverse (y-z) half plane at $x = 0$, shown in Figure 4.4, exhibits fine-scale structures near the wall in all simulations. Even the QL simulation is able to reproduce some defined structure in the spanwise plane, which can be attributed in part to the allowed mode coupling in the spanwise (y) direction. Nevertheless, the QL approximation again overestimates the magnitude of the streamwise velocity.

To more clearly probe the turbulence structure, it is helpful to partition the velocity field into the mean and fluctuating components. The fluctuating streamwise velocity is computed by subtracting off the long-time and horizontal mean, $u' = u - \langle u \rangle_{t,x,y}$, where the time averaging is performed over the statistically steady realizations defined in Section 4.1. The instantaneous fluctuating streamwise velocity field in the horizontal plane is shown in Figure 4.5 and, again, it is evident that the fine-scale structure in the near-wall region is better reproduced by the GQL simulations. In Figure 4.6, the addition of the instantaneous spanwise-wall-normal velocity (v', w') quiver plot overlay shows the perturbation structure in the wall-normal/spanwise plane. With the effects of the mean flow removed, the wavy streaks evident in the horizontal plane and the more complex roll dynamics in the vertical plane of NL are seen to be better captured by the GQL simulations.

Finally, the streak component of the streamwise mean velocity, $U_s = U - \langle U \rangle_y$, is shown in Figure 4.7 at one instant in time with an overlay of the corresponding streamwise-averaged spanwise/wall-normal velocities (V, W). The rolls and streaks can be seen more clearly by time-averaging U_s (and the associated spanwise/wall-normal velocities), shown in Figure 4.8.

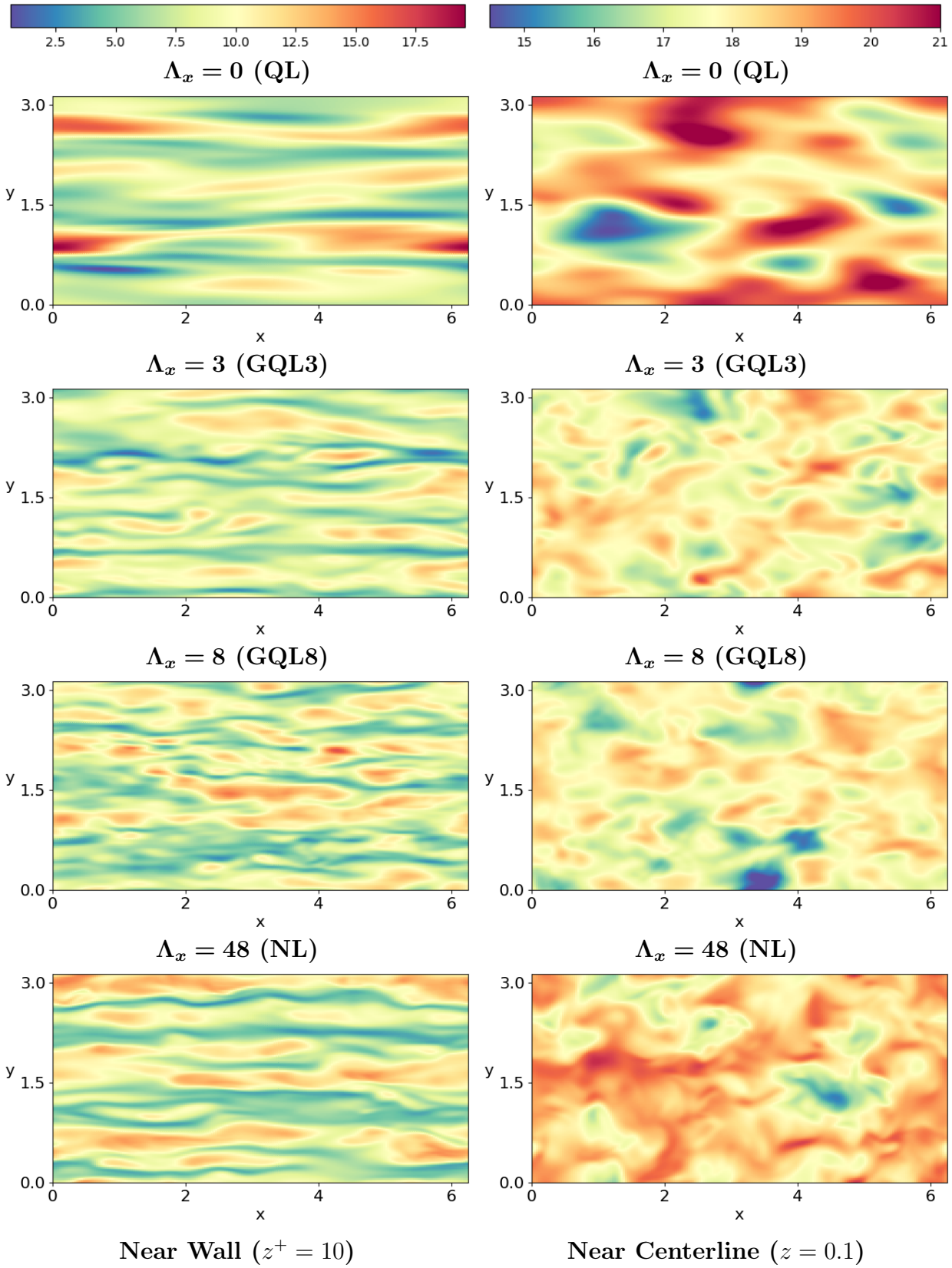

Figure 4.3: Instantaneous streamwise velocity in the horizontal (x-y) plane at $z^+ = 10$ (left column) and near-centerline at $z = 0.1$ (right column) for various Λ_x.

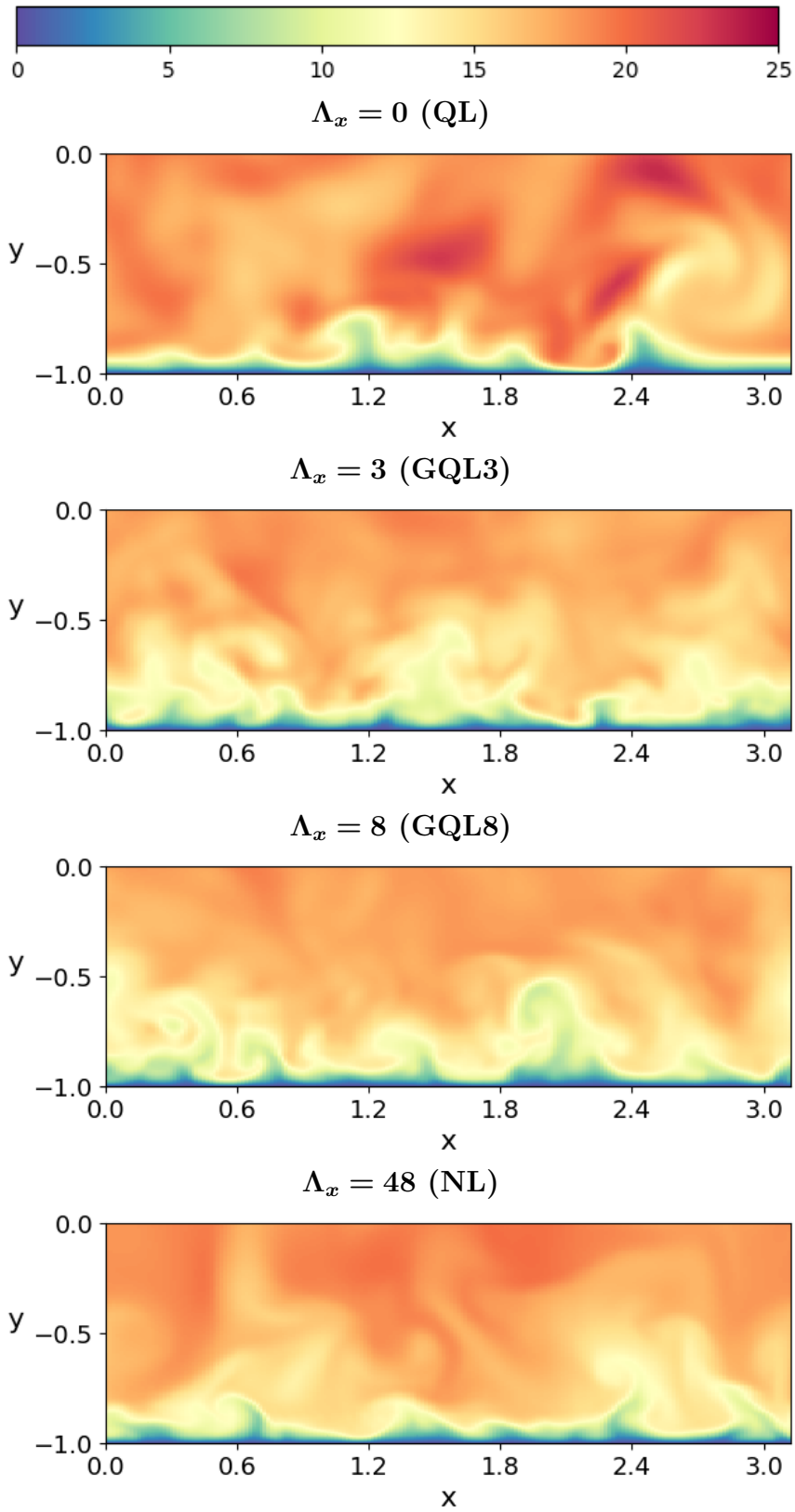

Figure 4.4: Instantaneous streamwise velocity in the vertical (y-z) plane at $x = 0$ for various Λ_x.

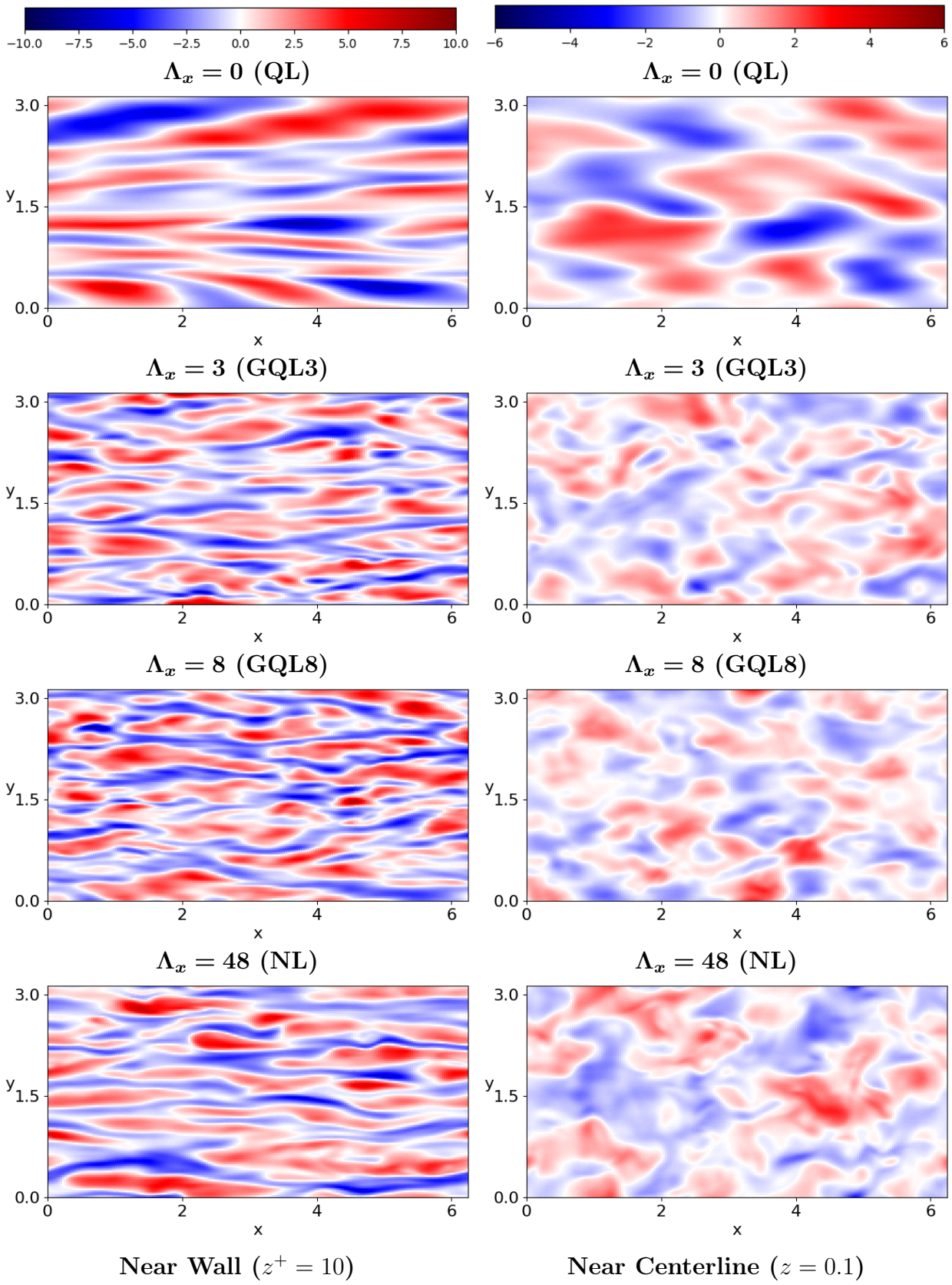

Figure 4.5: Instantaneous fluctuating streamwise velocity in the horizontal (x-y) plane at $z^+ = 10$ (left) and near-centerline at $z = 0.1$ (right) for various Λ_x.

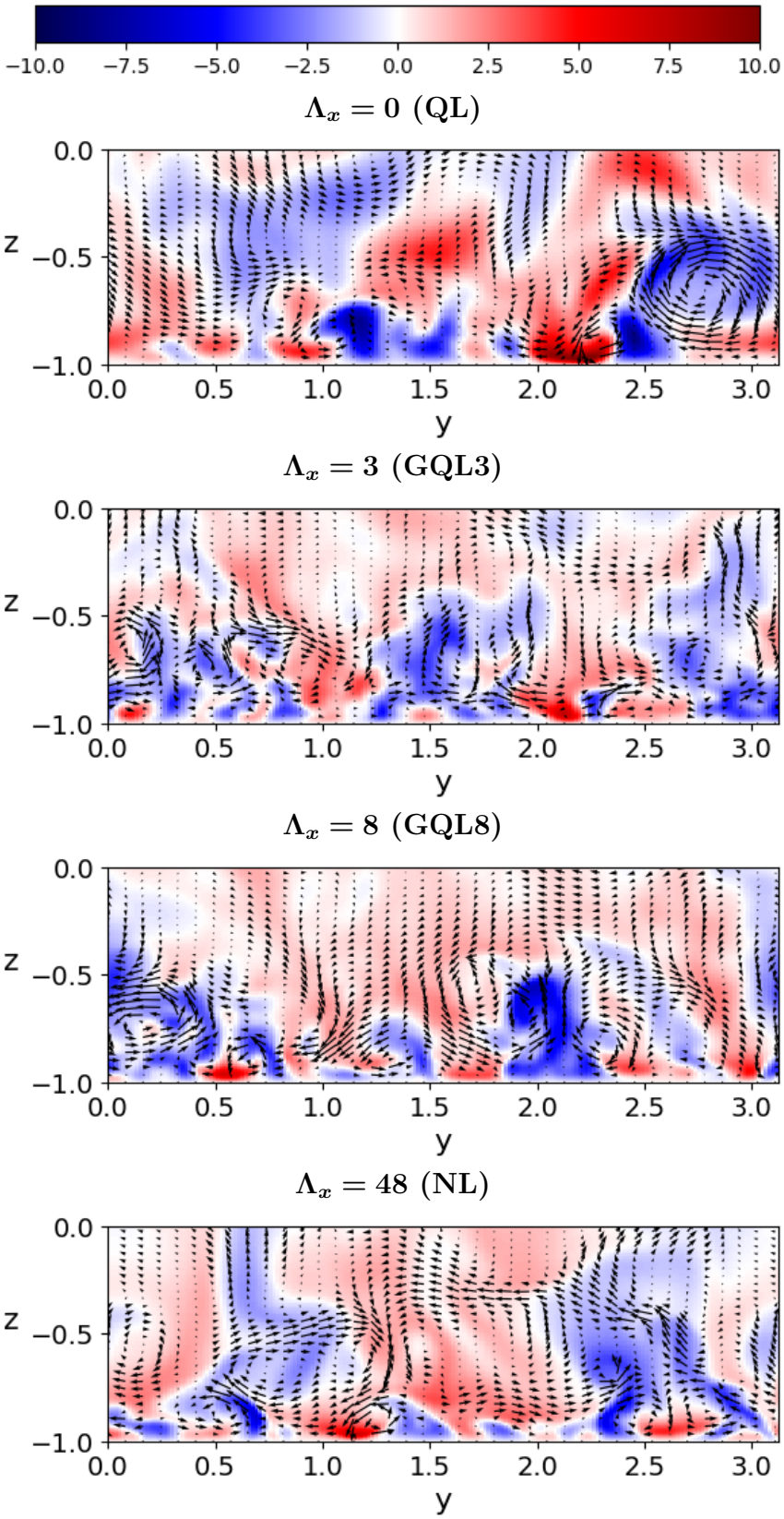

Figure 4.6: Instantaneous fluctuating streamwise velocity in the vertical (y-z) plane at $x = 0$ with (v',w') overlay for various Λ_x.

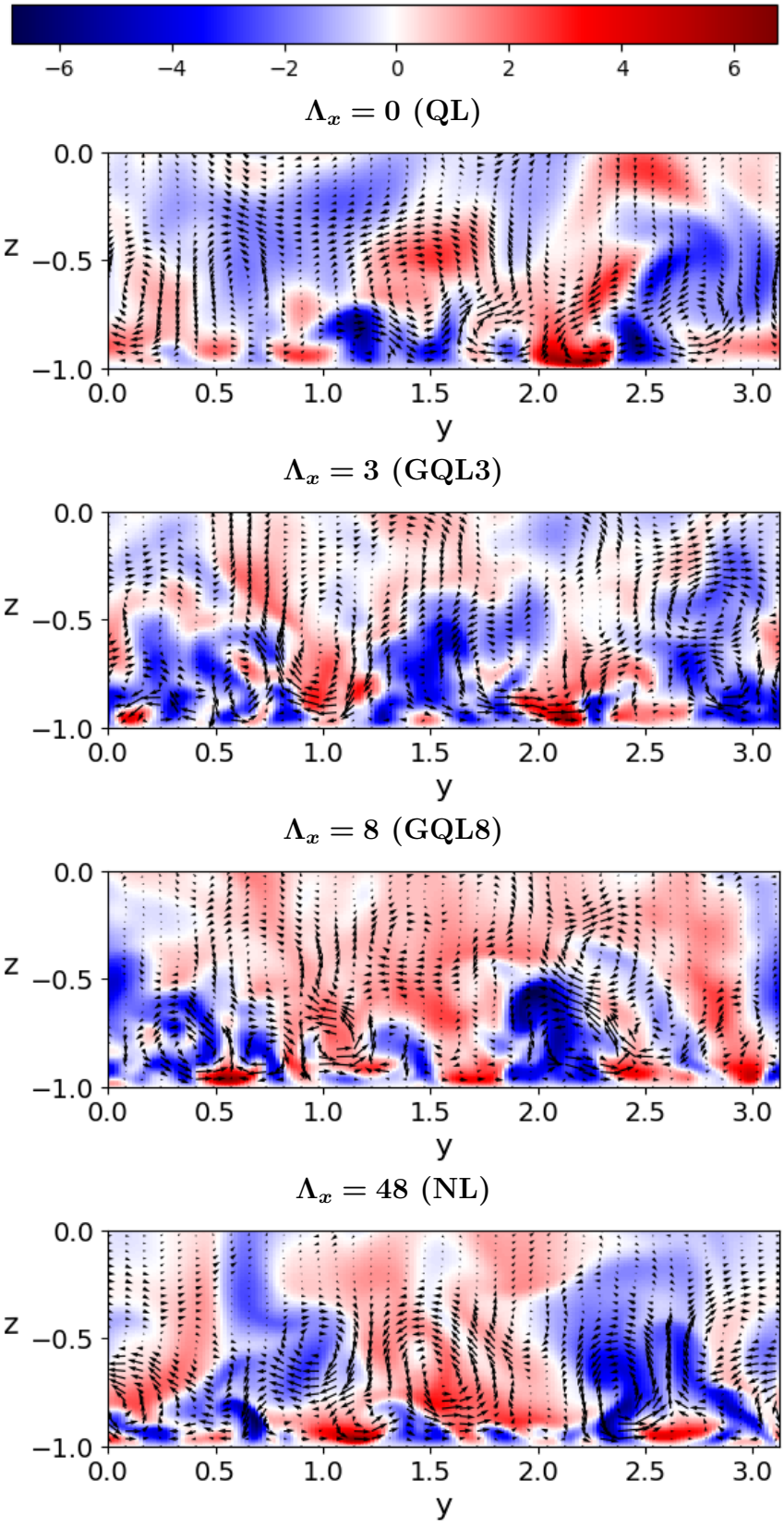

Figure 4.7: Instantaneous streak component in the vertical (y-z) plane at $x = 0$ with (V,W) overlay for various Λ_x.

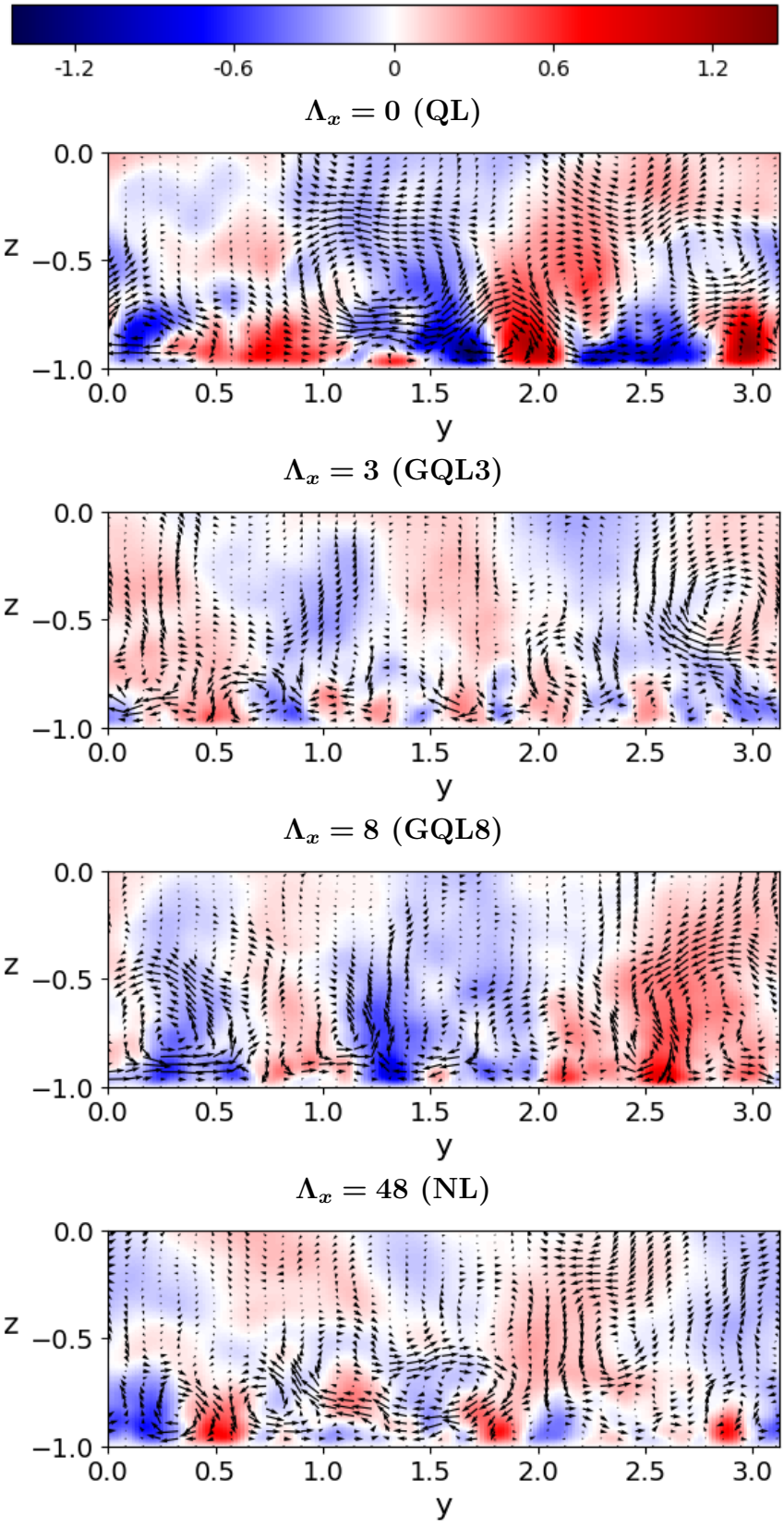

Figure 4.8: Time-averaged streak component in the vertical (y-z) plane at $x = 0$ with $(\langle V\rangle_t,\langle W\rangle_t)$ overlay for various Λ_x.

Streak spacing

It is clear from the instantaneous images that the near-wall region is dominated by low- and high-speed streaks. To further quantify how well the GQL approximation can recover the structure of the flow, a quantitative measure of the spanwise streak-spacing is obtained. Based on a multitude of physical experiments, the characteristic spacing between the streaks near the wall is on average $\Delta y^+ \approx 100$, independently of Reynolds number (Pope, 2000). Here, the streak spacing is quantified using a two-point spanwise correlation of the streamwise fluctuating velocity u', defined as

$$R_{u'u'}(\Delta y, z_1, z_2) = \frac{1}{L_x L_y} \int_0^{L_x} \int_0^{L_y} u'(x, y, z_1) u'(x, y + \Delta y, z_2)\, dx\, dy \tag{4.1}$$

where Δy is the distance between the two spanwise points and, in this computation, only one horizontal plane is used (i.e., $z_1 = z_2$).

In Figure 4.9, the two-point spanwise correlation at $z^+ = 10$ of select GQL simulations is compared with that of QL and NL. The distance Δy has been scaled in wall units, and the correlation function $R_{u'u'}$ has been normalized by the root-mean-square (rms) of the streamwise fluctuating velocity and time-averaged over the statistically steady data. By construction, $R_{u'u'}(\Delta y^+ = 0) = 1$, corresponding to perfect correlation. The first minimum of $R_{u'u'}$ indicates the location of a streak with opposite-signed velocity (i.e., negative correlation). $R_{u'u'}$ crosses zero again for NL and all GQL simulations at $\Delta y^+ \approx 110$, which is in accord with the general consensus of expected streak spacing of 100 wall units (Aghdam and Ricco, 2016; Jiménez and Kawahara, 2013). The spanwise streak spacing for the QL simulation is larger, which accords with the coarse streak pattern evident in Figure 4.5.

Enstrophy

The energy input from the pressure gradient driving the flow is balanced on volume average by the viscous dissipation, which can be related to the volume integral of the magnitude

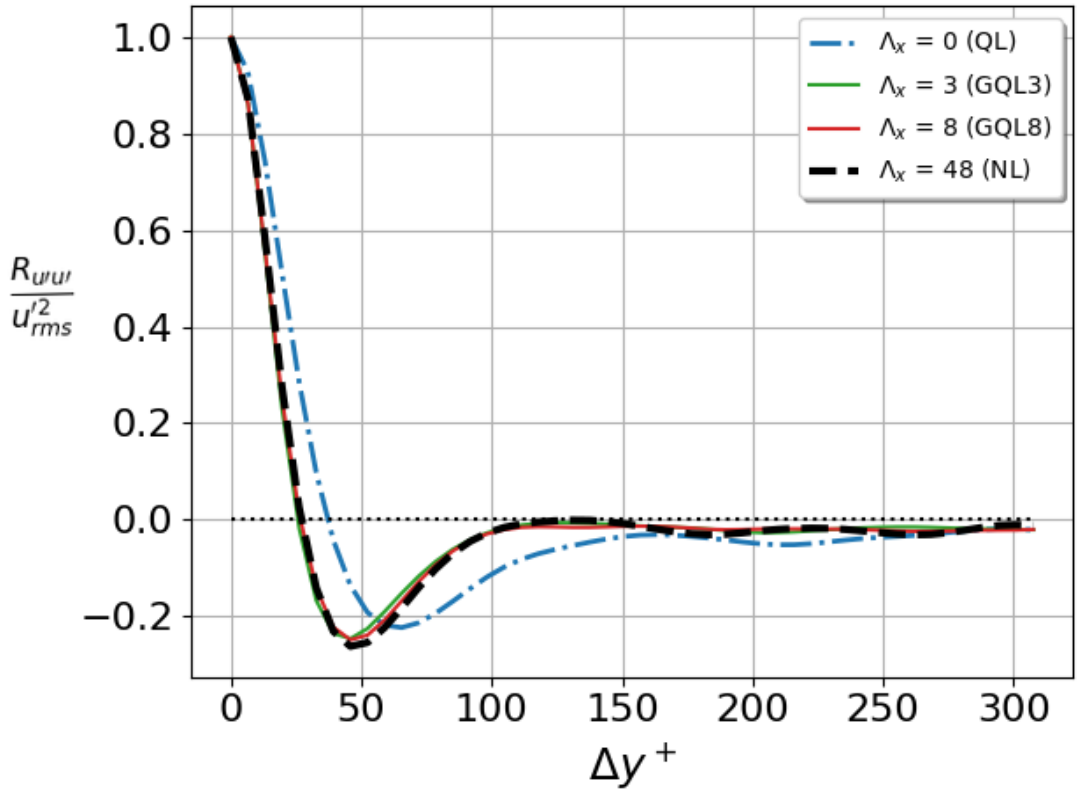

Figure 4.9: Time-averaged two-point spanwise correlation of streamwise velocity fluctuations obtained from select simulations for various Λ_x.

of the vorticity squared:

$$\int \epsilon dV = \frac{1}{Re} \int |\nabla \times \boldsymbol{u}|^2 \, dV \tag{4.2}$$

where ϵ is the dissipation rate and $\nabla \times \boldsymbol{u} = \boldsymbol{\omega}$ is the total vorticity (Tobias and Marston, 2017). The volume-integrated enstrophy is given by the integral on the right-hand side of Equation (4.2). The enstrophy of the system, which thus is proportional to the dissipation rate, can be used as another means to determine the effectiveness of the GQL approximation. The enstrophy can be readily computed for each simulation from the corresponding velocity field data, and the resulting enstrophy from the QL and GQL simulations compared to the fully nonlinear result to quantify the effectiveness of the approximations.

The volume integral from Equation (4.2) is computed by averaging in the horizontal (x-y) plane, then integrating over the wall-normal (z) direction. The resulting values of

Simulation	QL	GQL2	GQL3	GQL8	GQL10	GQL15	GQL20	**NL**
Enstrophy	34.2	29.6	30.7	30.2	30.2	32.9	31.9	**31.7**

Table 4.2: Enstrophy $\int_V \omega^2 dV$ for all $Re_\tau = 200$ simulations from Table 4.1.

the enstrophy for all simulations are shown in Table 4.2. The QL simulation significantly overestimates the enstrophy relative to the NL result, while the GQL simulations, even at modest Λ_x, better reproduce the true enstrophy of the flow. Another feature revealed by this comparison is the non-monotonic variation in the enstrophy as more nonlinear interactions are permitted among the low modes in the GQL simulations. These results and trends are in agreement with those reported in Figure 4.1 in the previous section.

Vortical structure

It is well-established that in highly turbulent flows, there exist regions of large vorticity, $\boldsymbol{\omega}$, organized in thin tube-like structures. The three-dimensional rendering of the magnitude of these vortex tubes is shown in Figure 4.10 for QL, GQL3, and NL, created using Mayavi (Ramachandran and Varoquaux, 2011). The fine-scale structure and the random alignment of the vortex tubes are clearly seen in the NL and GQL3 data, while the vortex tubes seen in the QL simulation lack the fine-scale structure present in the NL case and are aligned primarily in the streamwise direction.

Turbulent fluctuating velocities

To quantify the strength of the turbulence, the root-mean-square (rms) of the fluctuating velocities for all simulations was computed, as defined by Equation (2.22).

The rms streamwise fluctuating velocity profile is shown as a function of both inner (wall-normal) units, $z^+ = z/u_\tau$ (Figure 4.11a), and outer (wall-normal) units z/h (Figure 4.11b), while the spanwise and wall-normal fluctuating velocities are shown as functions of inner wall-normal units (Figures 4.11c and 4.11d, respectively). In all figures, the rms velocity components are normalized by u_τ.

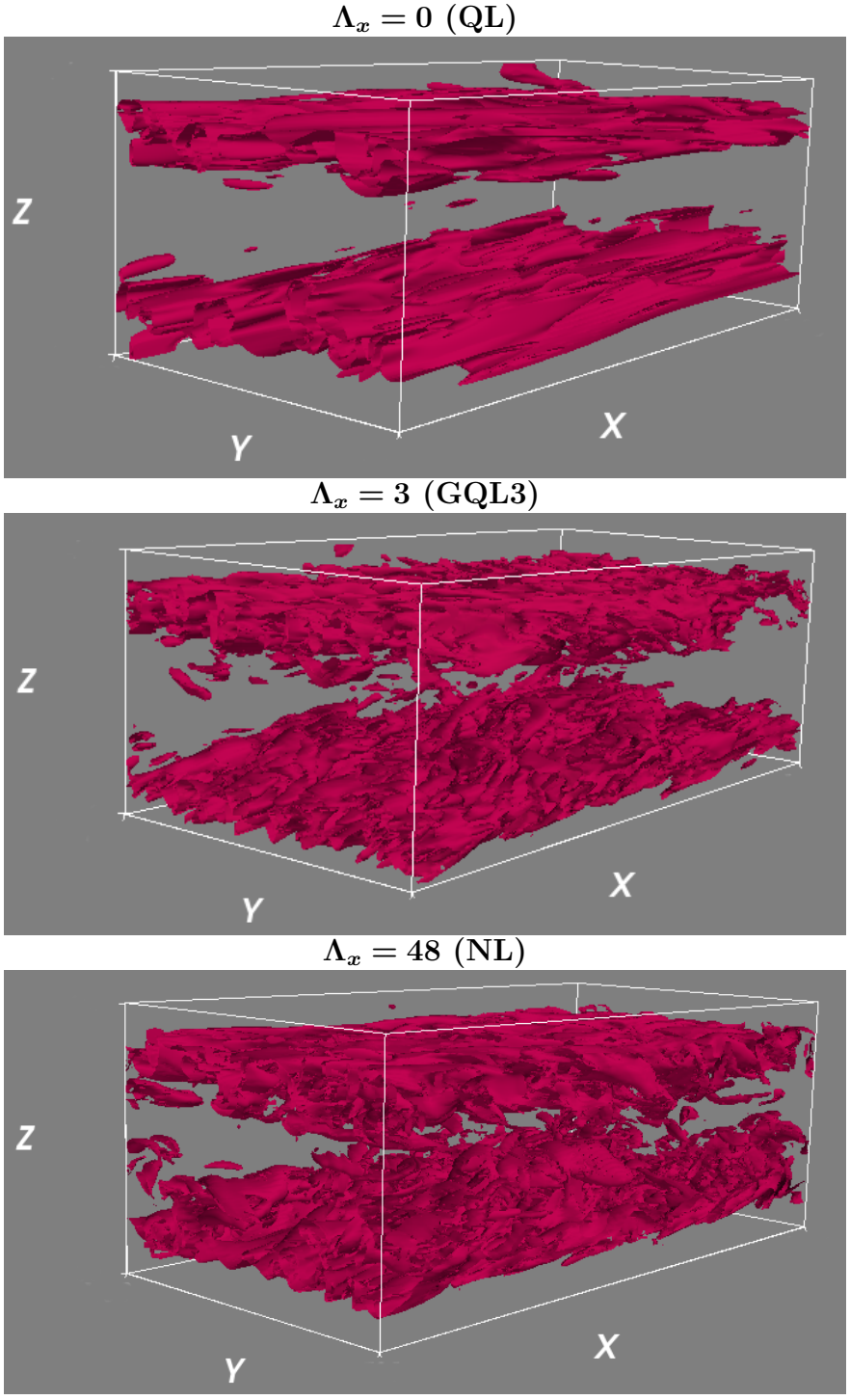

Figure 4.10: Isosurfaces of the enstrophy in QL, GQL3, and NL.

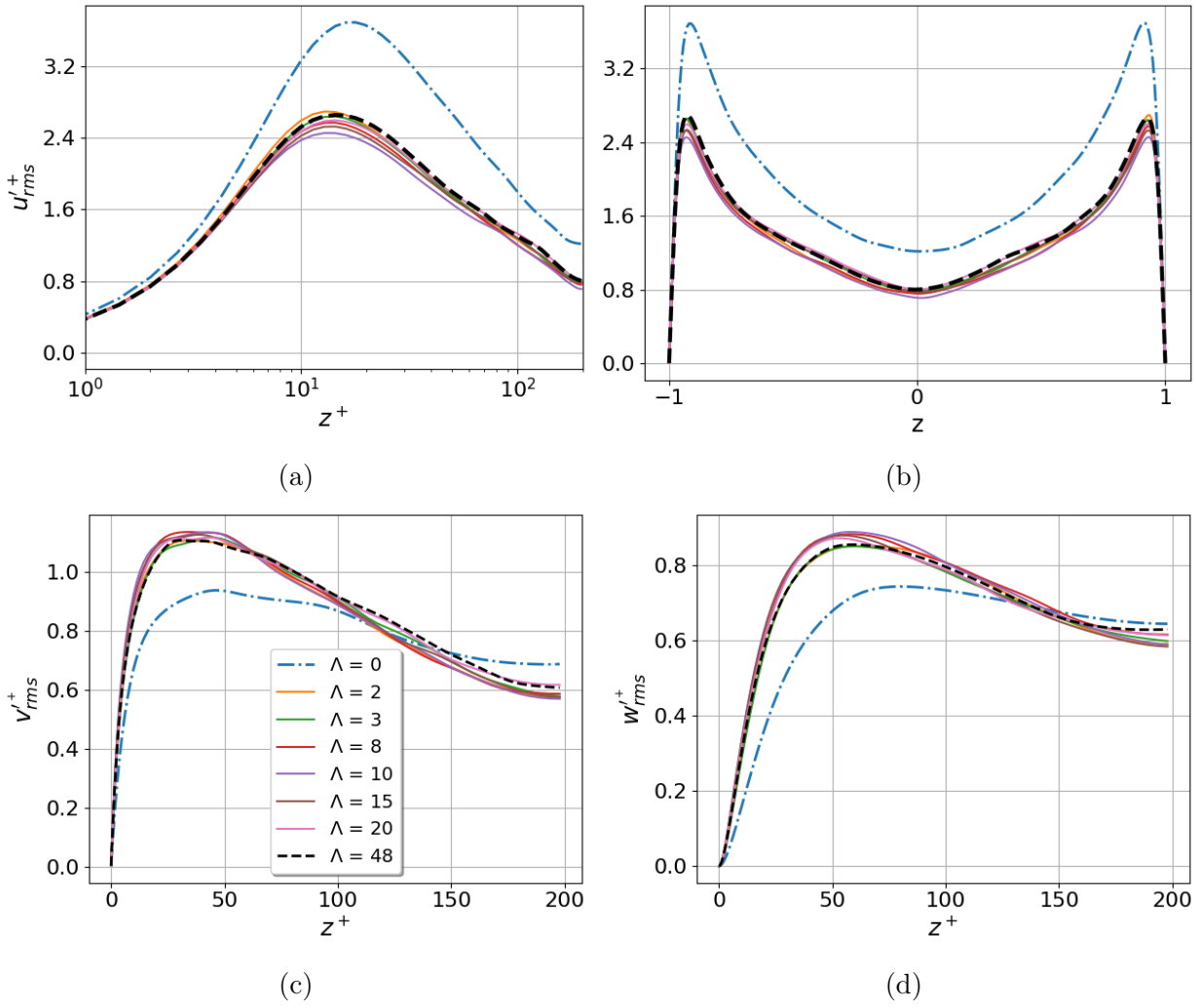

Figure 4.11: Root-mean-square fluctuating velocity components for various Λ_x. (a) u'_{rms} in inner normalized and (b) outer normalized units, (c) v'_{rms} and (d) w'_{rms}. The legend in (c) applies to all four subplots.

Remarkably, all GQL simulations accurately predict each of the three rms velocity components relative to the fully nonlinear simulation. The QL simulation significantly over-predicts u'_{rms} throughout the entire channel, and under-predicts v'_{rms} and w'_{rms} near the wall and overestimates them in the core. Thus, GQL, even with a few low modes retained, is more capable of predicting the profiles of turbulence intensity.

Reynolds stresses

The components of the Reynolds stress tensor and the turbulent kinetic energy, as defined by Equations (2.15) and (2.21), were computed for simulations using various values of Λ_x and are shown in a variety of ways.

First, select Reynolds stress profiles are shown as a function of inner normalized distance from the wall in Figure 4.12. QL significantly overestimates the streamwise fluctuating Reynolds stress and turbulent kinetic energy, while the GQL results are in closer agreement with those of the NL simulation (Figures 4.12a and 4.12d). More significantly, QL under-predicts the Reynolds shear stress near the wall, as evident in Figure 4.12c, which indicates the influence of the viscous effects extends farther from the wall relative to the fully nonlinear simulation. The attenuation of the Reynolds stress in the QL simulation effectively redefines the dynamics in the various regions of the flow, delaying streak breakdown and encroaching on the log region, which is the reason why QL fails to recover the log region dynamics. The GQL simulations, on the other hand, tend to slightly over-predict Reynolds shear stress near the wall, implying some elements of the fully nonlinear dynamics are missing, albeit to a lesser extent. Also, the accuracy of the GQL simulations, as compared to the NL simulation, is again seen to vary non-monotonically with increasing Λ_x.

The total stress budget for each simulation is plotted in Figure 4.13. Note that the location of peak production, i.e., where the viscous stress and Reynolds shear stress are equal, is shifted away from the wall in the QL simulation relative to NL, providing further evidence for the delay of streak breakdown.

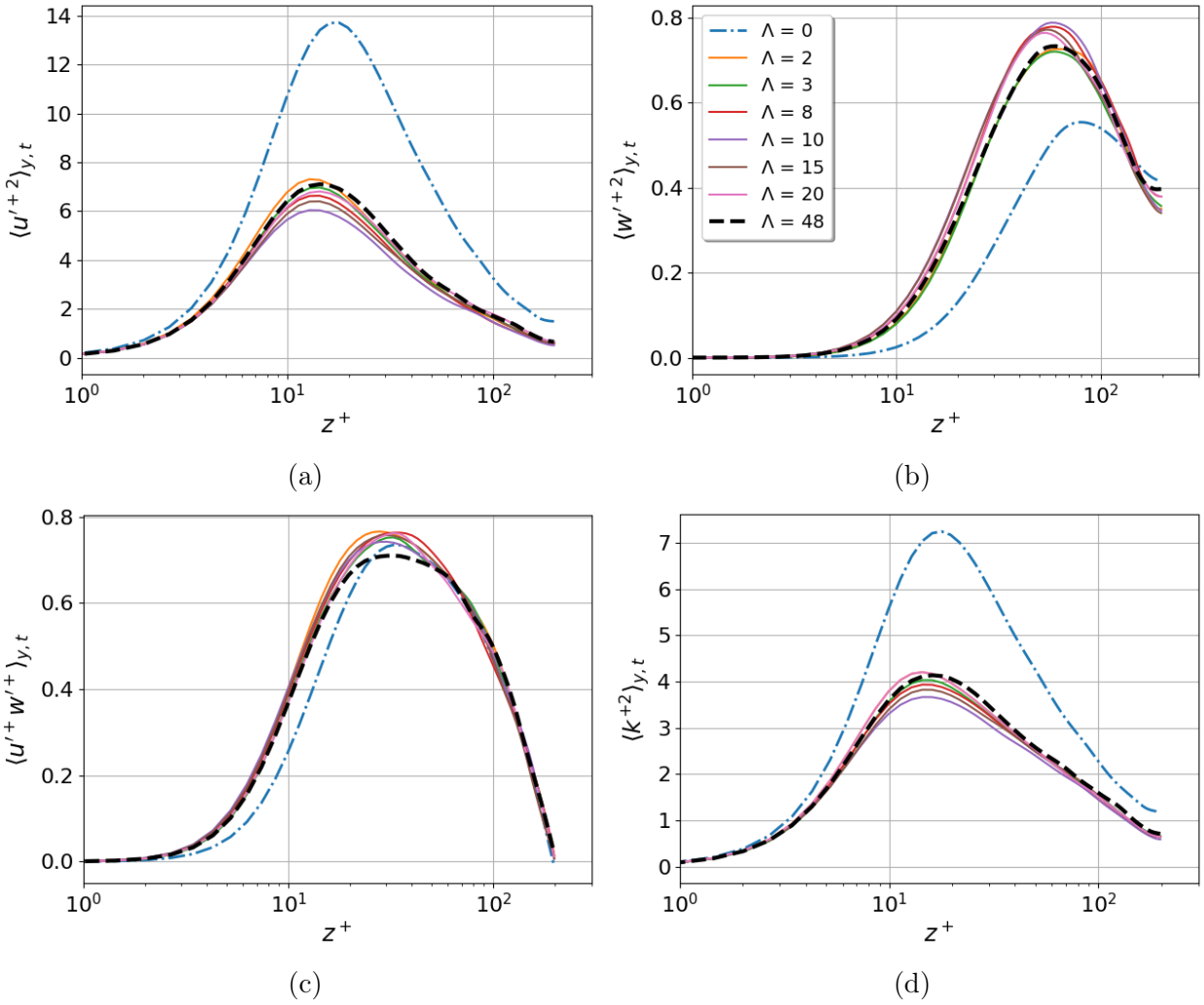

Figure 4.12: Select Reynolds stress profiles and turbulent kinetic energy profile for all simulations, where (a) $\langle u'^{+2}\rangle_{y,t}$, (b) $\langle w'^{+2}\rangle_{y,t}$, (c) $\langle u'^+ w'^+\rangle_{y,t}$, and (d) $\langle k^{+2}\rangle_{y,t}$. The legend in (b) applies to all four subplots.

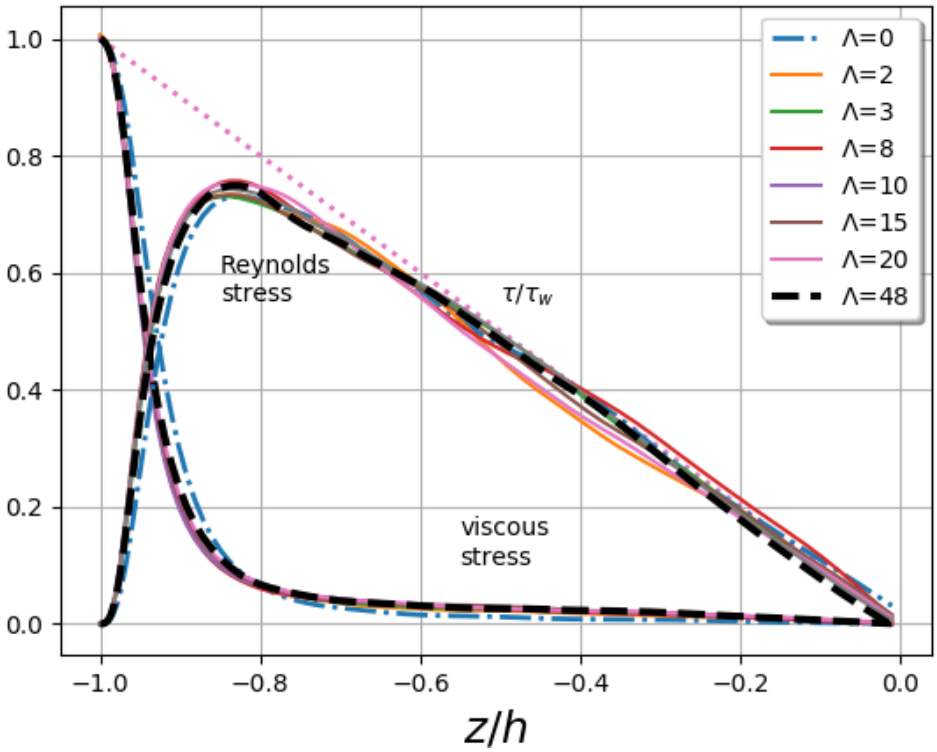

Figure 4.13: Reynolds shear stress and mean viscous stress profiles.

Characterization of Reynolds stress anisotropy

Recovering the anisotropic characteristics of the flow is critical to the success of the GQL algorithm. Recall from the discussion in Chapter 2 the Lumley triangle is an useful tool to characterize the anisotropy of the flow.

In Figure 4.14, the Reynolds stress invariants are plotted on the Lumley triangle for the QL, GQL3, and NL simulations. An immediate observation in comparing the QL data to the NL data is that all (ξ, η) pairs are shifted toward the 1-component region of the triangle, providing further evidence that the QL dynamics exhibit a delay in streak breakdown, and predict a flow dominated by streaks farther from the wall than is realized in the NL simulation. The distinctive cluster of constant η points in the log-law region is conspicuously absent (as predicted by the indicator function in Figure 4.2), as are the 2-component near-wall ($z^+ < 1$) points. Remarkably, the near-wall and log-law region contributions are

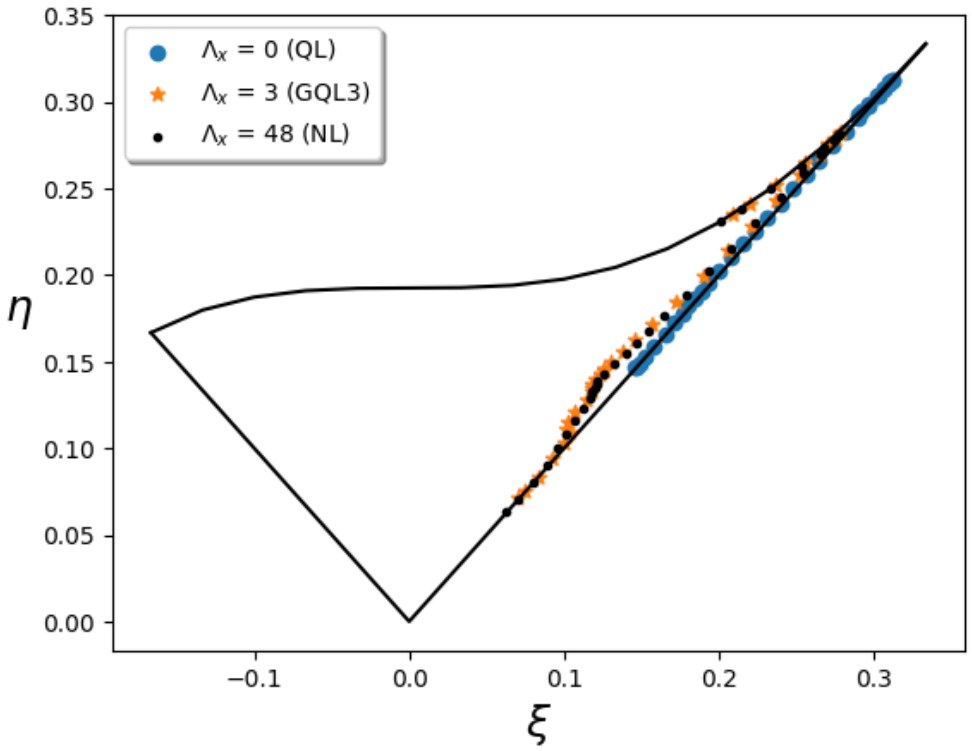

Figure 4.14: Direct comparison of Reynolds stress invariants on the Lumley triangle for QL, GQL3, and NL.

recovered by retaining a modest number of nonlinear low modes, as evident in the GQL3 simulation. The Lumley triangle provides compelling evidence that the physical structure of turbulence in the channel, and thus the flow dynamics, are better recovered by the GQL methodology.

Q-*R* invariants

Another way to visualize the kinematic features of turbulent channel flow is via the invariants of the velocity gradient tensor, as described in Chapter 2. Figure 4.15 shows Q-R plots for the QL, GQL3, and NL simulations. To create these plots, a joint pdf was constructed from one instantaneous snapshot of the velocity gradient tensor at a wall-normal location in the near-wall region using the Seaborn data visualization library written in Python (Waskom et al.). To include more data points for more reliable statistics, the joint pdf includes two adjacent horizontal planes ($z^+ = 8.612$ and $z^+ = 9.924$).

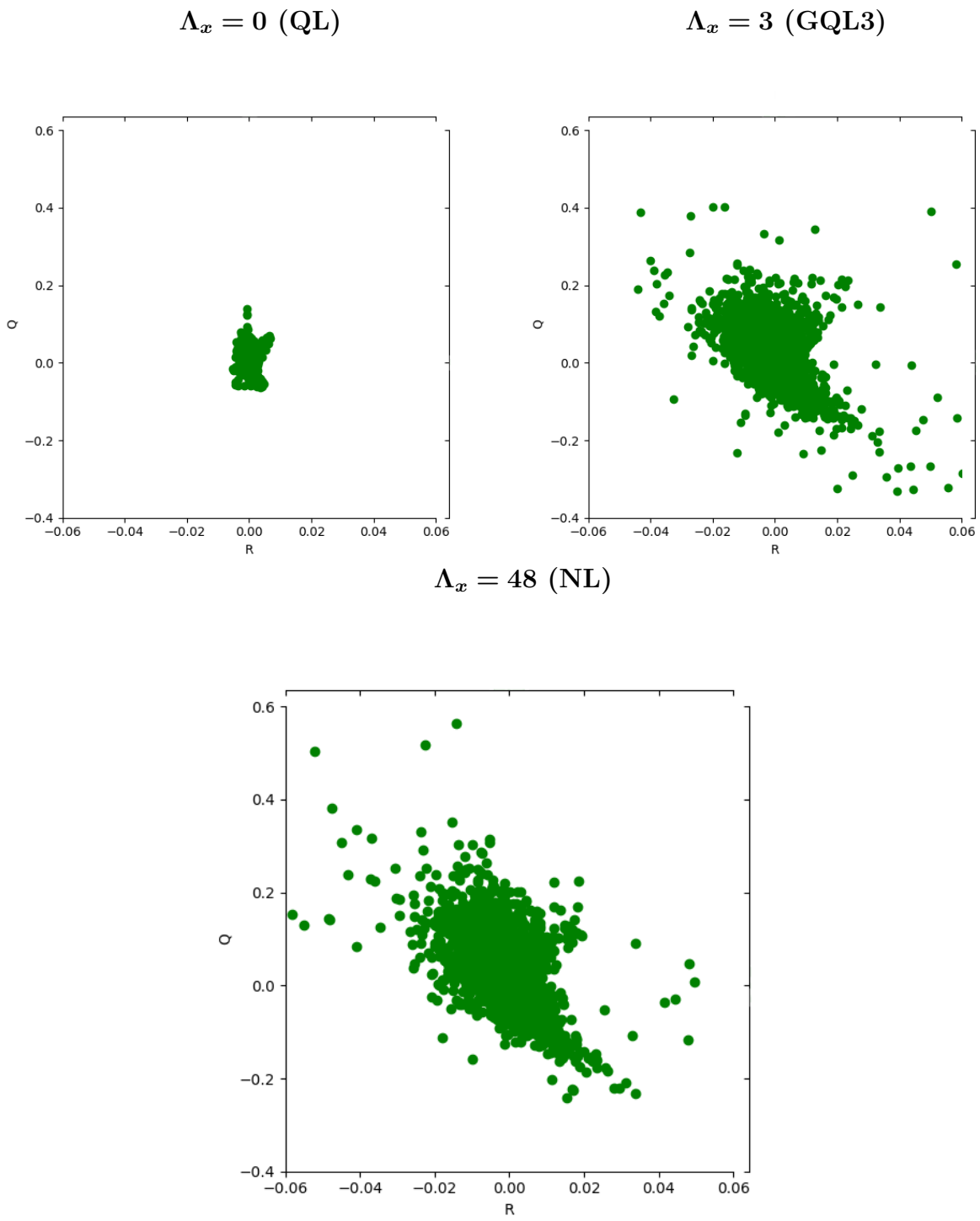

Figure 4.15: Joint pdf of the Q-R invariants at $z^+ = 8.612$ and $z^+ = 9.924$ for QL, GQL3, and NL.

The QL simulation exhibits very small values of Q and R, and fails to recover the characteristic teardrop shape of the pdf, which corresponds physically to low strain resulting in one-dimensional flow. In stark contrast, the topology of the flow in GQL3 is qualitatively similar to that of NL; in particular, the characteristic shape of the NL pdf, is captured.

Energy in physical space

Energy is a critically important quantity in the study of turbulence and its transfer underlies many of the mechanisms in the transition to and sustenance of turbulence. Of particular interest in assessing the accuracy of the approximation methods is the budget of turbulent kinetic energy and the distribution of the streamwise fluctuating kinetic energy among the dynamic range of scales.

The budget of turbulent kinetic energy can be analyzed in both physical space and wavenumber space, but in this section the analysis will focus on an evaluation in physical space. The terms of the turbulent kinetic energy budget defined in Equation (2.15) have been computed for QL, GQL3, GQL8, and NL simulations, and are shown in Figure 4.16. The residuals, i.e., the differences between the terms in the QL and GQL energy budgets and those in the NL budget, are shown in Figure 4.17.

Again, QL fails to accurately recover important aspects of the fully nonlinear dynamics. Notably, the turbulent kinetic energy peak production in QL is shifted significantly away from the wall, which is also observed in the total stress budget shown in Figure 4.13, while peak production is shifted slightly towards the wall in GQL.

Another significant difference between the QL and GQL simulations is evident in the vertical profile of turbulent advection, also known as nonlinear transfer, as this mechanism arises from the nonlinear term in the governing PDEs. QL over-predicts turbulent advection towards the wall as well as away from the core. In contrast, GQL slightly under-predicts the turbulent advection toward the wall and slightly over-predicts the nonlinear advection away from the core. These deviations are, of course, a direct consequence of the omission of

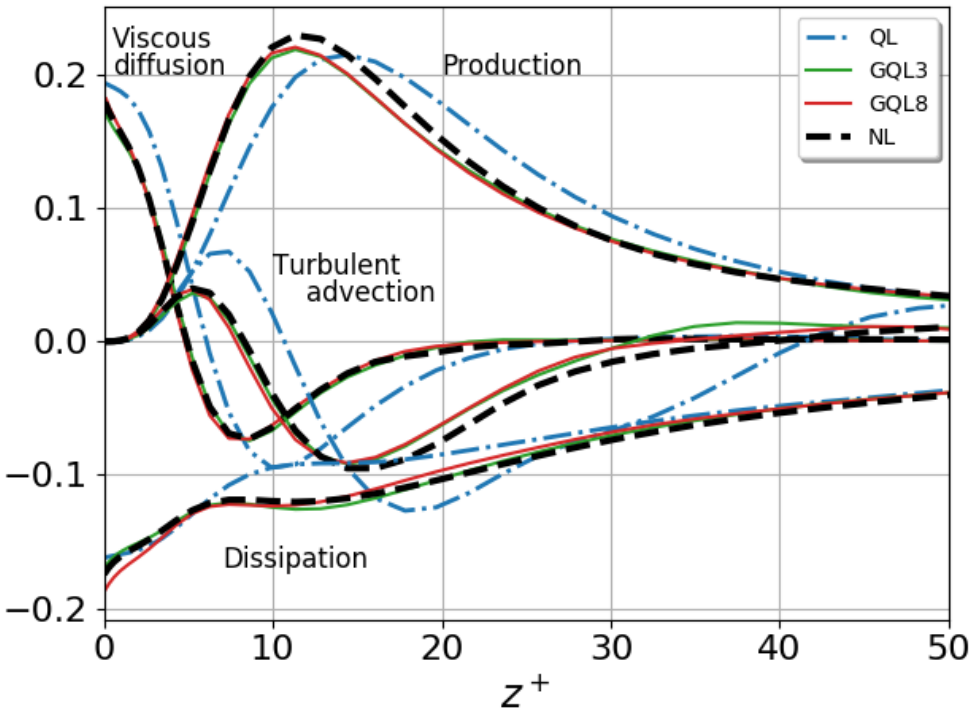

Figure 4.16: Turbulent kinetic energy budget for select simulations. Note that the pressure transport term is not shown.

certain nonlinear interactions in the QL and GQL simulations, and hence are of particular interest in understanding the dynamics recovered (and not recovered) by the various approximation methods. Clearly, the nonlinear interactions permitted by the various (even modest) truncations of GQL enable key aspects of the turbulence energetics across the channel to be more accurately captured than is possible with the QL approximation.

Energy in wavenumber space

To better understand the effect of the QL and GQL approximations on the nonlinear transfer term and the overall energy of the system, it is instructive to analyze these quantities in wavenumber space as a function of the dynamic range of scales.

The turbulent kinetic energy balance in wavenumber space was derived in Chapter 2 and is represented by Equation (2.20). The nonlinear transfer of energy is described by the second term on the right hand side of Equation (2.20), written separately here:

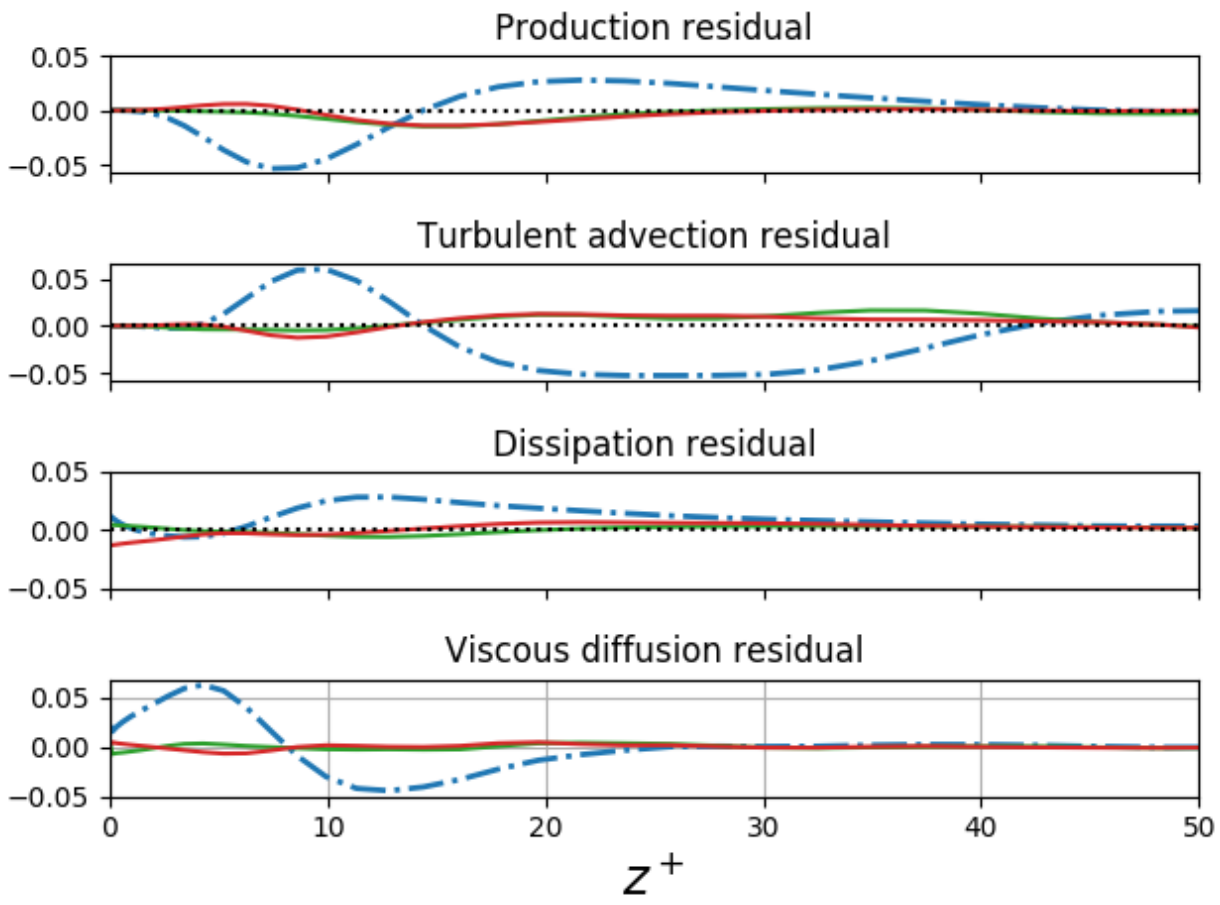

Figure 4.17: Residuals of the components of the turbulent kinetic energy budget for select simulations (see Figure 4.16).

$$T(\boldsymbol{\kappa}, z) = \Re\left[\hat{\boldsymbol{u}}^*(\boldsymbol{\kappa}, z)\hat{\boldsymbol{N}}(\boldsymbol{\kappa}, z)\right] \tag{4.3}$$

The analysis of the nonlinear transfer term that follows is outlined by Domaradzki et al. (1994). The total nonlinear energy transfer in a horizontal plane at a particular instant in time was obtained by summing over all wavenumbers $\boldsymbol{\kappa}$ for fixed z. The total plane-averaged energy transfer, $T_I(z)$, is then plotted in Figure 4.18 and compared with the contribution from the mean (i.e., $\boldsymbol{\kappa} = 0$) and the contribution from the fluctuations about the mean (i.e., $\boldsymbol{\kappa} \neq 0$) for the QL, GQL3, and NL simulations. In all three cases, the largest contribution to nonlinear energy transfer is from the mean, where energy is extracted from the core and transferred to the near-wall region. In QL, the magnitude of the energy transferred

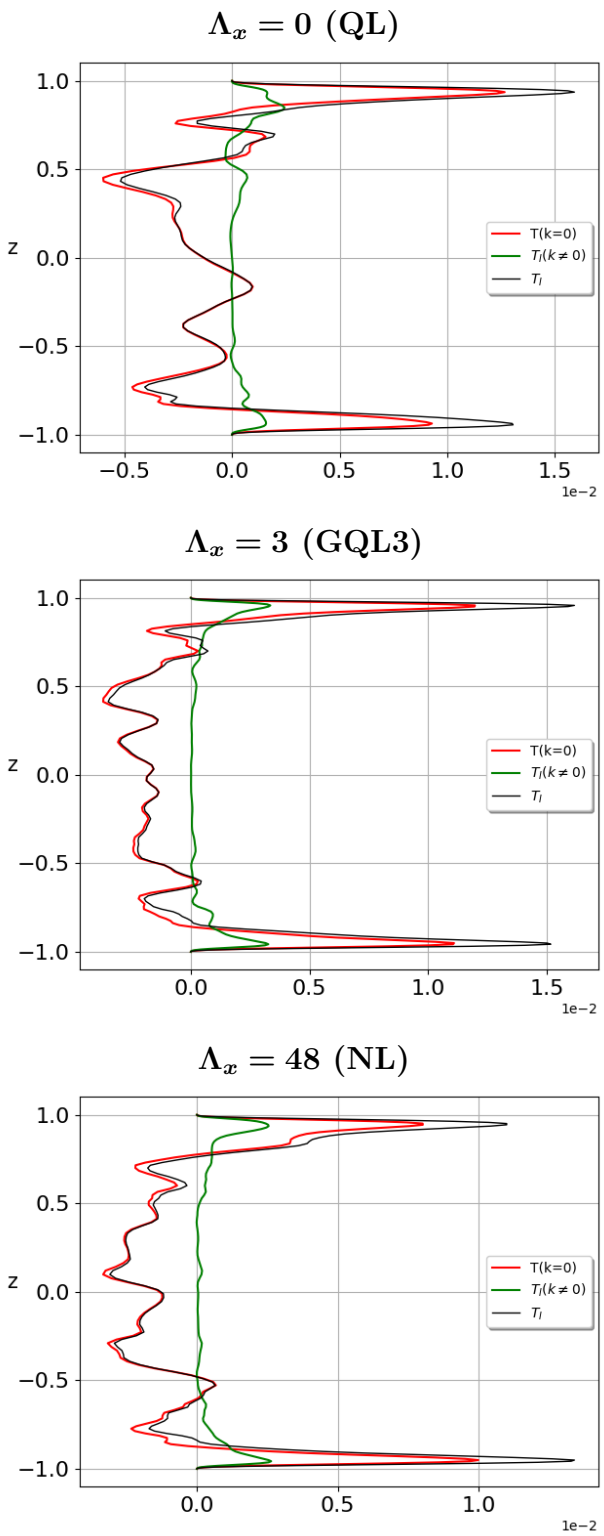

Figure 4.18: Total horizontal plane-averaged nonlinear energy transfer, the contribution from the mean ($\boldsymbol{\kappa} = 0$ mode), and contribution from the fluctuations ($\boldsymbol{\kappa} \neq 0$ modes) for QL, GQL3, and NL.

away from the core is larger relative to NL, which again reinforces the observation that QL over-predicts the mixing in the core. GQL better predicts the energy transfer away from the core, but does slightly overestimate the energy transfer towards the walls through nonlinear interactions involving the mean and the fluctuations. These observations are in concert with those made regarding the turbulent advection term in physical space. As noted previously, GQL necessarily omits certain dynamics due to the (albeit less severe) restriction of the energy cascade, which can be seen more readily in a spectral analysis of the nonlinear energy transfer terms specifically. Indeed, this methodology enables many other avenues of exploration, including, e.g., computing the nonlinear energy transfer contribution associated with specific bands of modes, that may illuminate aspects of the dynamics associated with nonlinear energy transfer retained (and neglected) in the various GQL approximations.

Another method of assessing the accuracy of the various simulations is through an analysis of the two-dimensional energy spectra. The two-dimensional energy spectra for the fluctuating streamwise velocity u' in the horizontal plane $z^+ = 10$ is obtained by computing the two-dimensional discrete Fourier transform of the fluctuating streamwise velocity u', exploiting the discrete Parseval relation in two dimensions, and time averaging the energy spectra over the statistically-steady regime for each simulation:

$$E(k_x, k_y, z) = \frac{1}{2N_x N_y} \hat{u}(k_x, k_y, z)\hat{u}^*(k_x, k_y, z) \tag{4.4}$$

In Figure 4.19, the two-dimensional spectra for the fluctuating streamwise velocity near the wall ($z^+ = 10$) is shown. The color field represents the turbulent kinetic energy on a base 10 logarithmic scale as a function of streamwise and spanwise wavenumbers. The white region indicates energy below the established minimum threshold indicated by the color bar. Immediately apparent in the QL simulation is the restriction in the streamwise cascade of energy to small scales and the large energy magnitudes relative to NL. The magnitude and distribution of energy in the GQL simulation with just three low modes constitutes a dramatic improvement over QL. Interestingly, in the GQL8 energy spectrum, there is a

distinctive discontinuity along $k_x = 8$, which is more apparent in the one-dimensional energy spectra as a function of k_x.

To obtain a better sense of how energy is distributed among the different scales in each of the horizontal directions, the one-dimensional energy spectra of u' is computed by following the same procedure as for the 2D spectra except using the one-dimensional discrete Fourier transform with appropriate normalization. In each case, the energy spectra is averaged appropriately to show a 1D profile.

As evident in Figure 4.20a, the streamwise-averaged streamwise kinetic energy as a function of the spanwise wavenumber obtained from each of the GQL simulations shows excellent agreement with the corresponding NL spectrum. As expected, the QL simulation is quantitatively shown to retain too much energy in the large scales and dissipates too severely in the small scales, owing to the suppression of energy scatter among streamwise (x) Fourier modes. In Figure 4.20b, showing spanwise-averaged streamwise kinetic energy as a function of the streamwise wavenumber, the discontinuity observed in GQL8 in Figure 4.19 is seen more clearly in all simulations for $\Lambda_x \geq 8$. Upon closer inspection, a discontinuity exists for all GQL simulations at precisely the streamwise spectral cutoff, Λ_x, the wavenumber at which the equations governing the large and small scales switch. For $\Lambda_x \leq 3$, the discontinuity is seen only in the slope, but as Λ_x increases, there is a discontinuity in the energy itself, the magnitude of which increases with increasing Λ_x until all high modes are strongly damped. The origin of this phenomenon is explored in greater detail in Chapter 6.

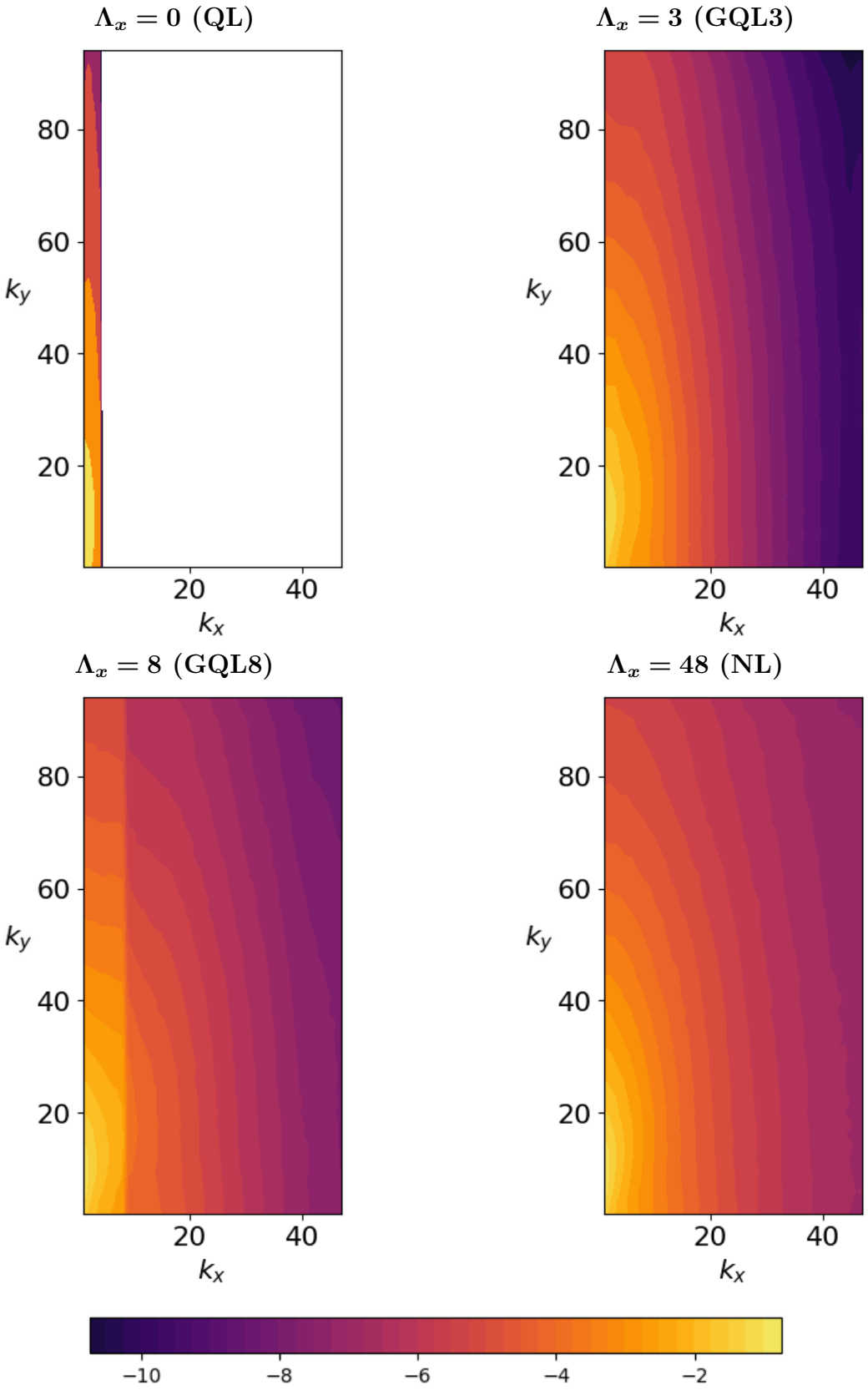

Figure 4.19: Two-dimensional energy spectra for streamwise velocity fluctuations in the horizontal plane $z^+ = 10$ for select GQL simulations.

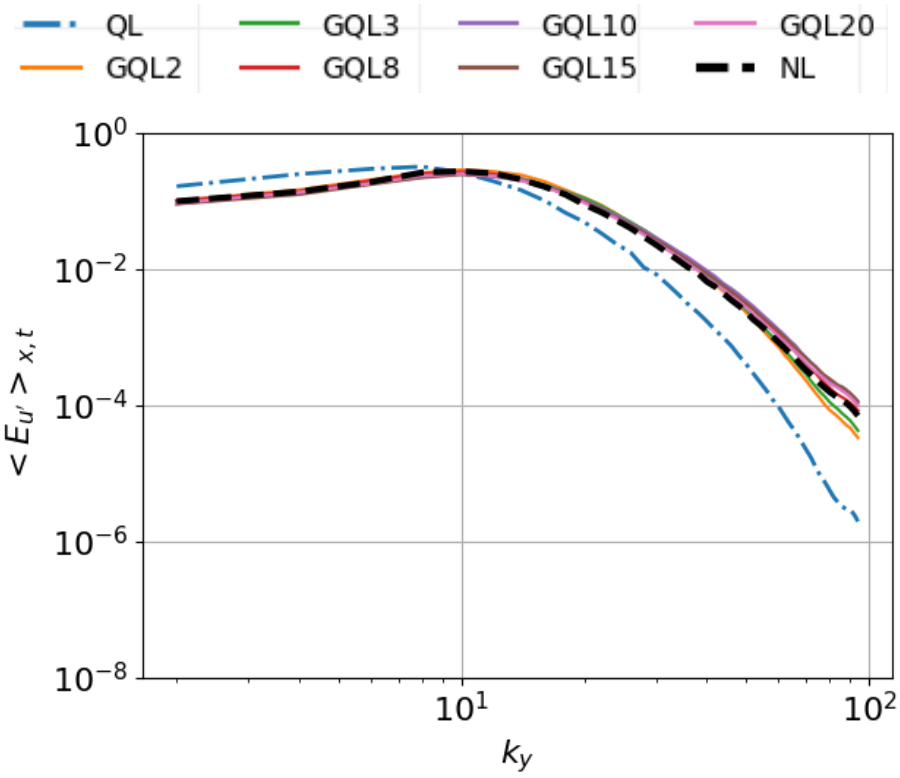

(a)

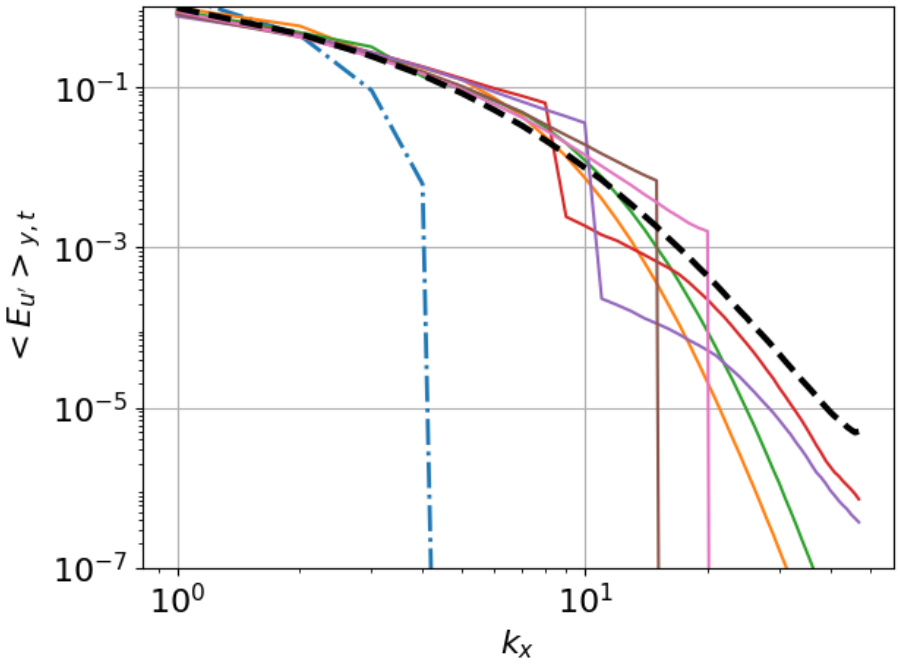

(b)

Figure 4.20: (a) Time and streamwise-averaged streamwise kinetic energy $\langle E_{u'} \rangle_{x,t}$ as a function of k_y and (b) time and spanwise-averaged streamwise kinetic energy $\langle E_{u'} \rangle_{y,t}$ as a function of k_x.

Chapter 5

GQL Simulations at Low Reynolds Number

In accord with the goal of developing a robust algorithm, a suite of simulations is performed in a lower Reynolds number parameter regime. To ensure the sustenance of non-trivial dynamics, a spatially-extended horizontal domain is used for these simulations.

5.1 Code validation/minimum model

In this section, the single mode quasilinear (SMQL) algorithm is explored. Of particular interest is the versatility of the Python/Dedalus algorithm, which can operate in SMQL, QL, GQL, and NL modalities. Here, the code is tested for its SMQL capability by directly comparing the results to the SMQL code written in MATLAB, introduced in Section 3.1. Since the MATLAB code uses a different numerical algorithm and was coded independently, this comparison provides a good external validation. The SMQL data results are then compared to results from a modest GQL simulation and other related results in the literature.

Recall from Chapter 3 that the single mode quasilinear (SMQL) approximation is one in which the fluctuation-fluctuation interactions are neglected unless they feed back onto the mean *and* only a single streamwise fluctuation mode is retained. While there are more sophisticated choices, the retained fluctuation mode here is selected based on the streamwise dimension of the channel to simplify the coding.

For purposes of validation, a SMQL simulation is run using each algorithm in the parameter regime shown in Table 5.1. Note that the domain is spatially-extended in the horizontal

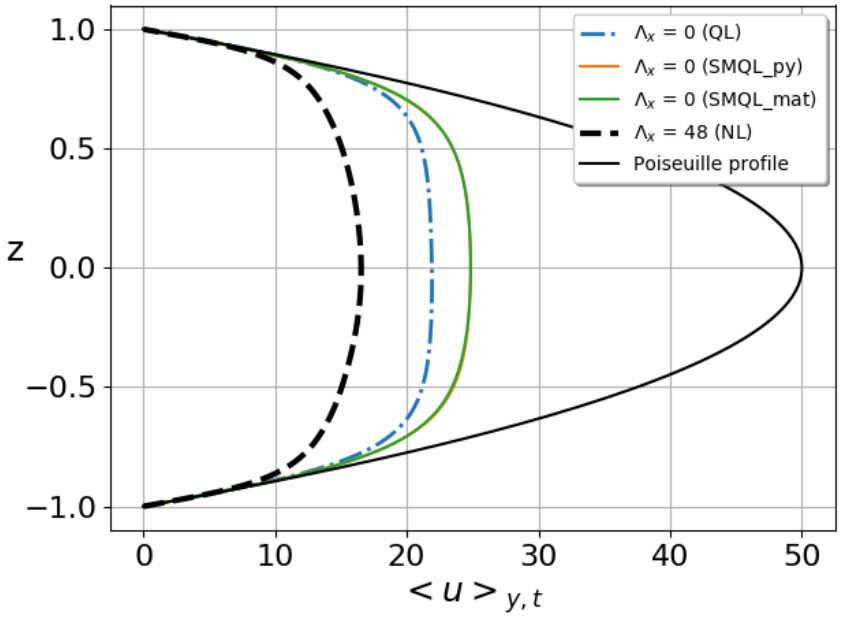

Figure 5.1: Comparison of mean velocity profiles obtained using SMQL (Dedalus) and SMQL (MATLAB), QL (Dedalus), and NL (Dedalus).

relative to the simulations performed at larger Re_τ. The fundamental wavenumber α_0 (i.e., the first streamwise Fourier mode of the fluctuation field) is retained in each case, which corresponds to $\alpha = 2\pi k_x/L_x = 1/8$, where the mode number $k_x = 1$. The SMQL simulations are initialized using the random-noise perturbations of the laminar solution. Both simulations are run to a statistically steady turbulent state with a dimensionless simulation time of $t = 210$, enabling a direct comparison between the two algorithms as well as with the fully nonlinear solution.

$[L_x, L_y, L_z]$	N_x x N_y x N_z	Re_τ
$[16\pi, 8\pi, 2]$	3 x 96 x 144	100

Table 5.1: SMQL simulation parameters.

The mean velocity profiles in Figure 5.1 show turbulence is sustained in each of the three cases. A team of researchers working on the restricted nonlinear (RNL) model have also been able to sustain turbulence in a channel using a single fluctuation mode, albeit at a much higher Reynolds number (Farrell et al., 2016; Bretheim et al., 2018). The mean veloc-

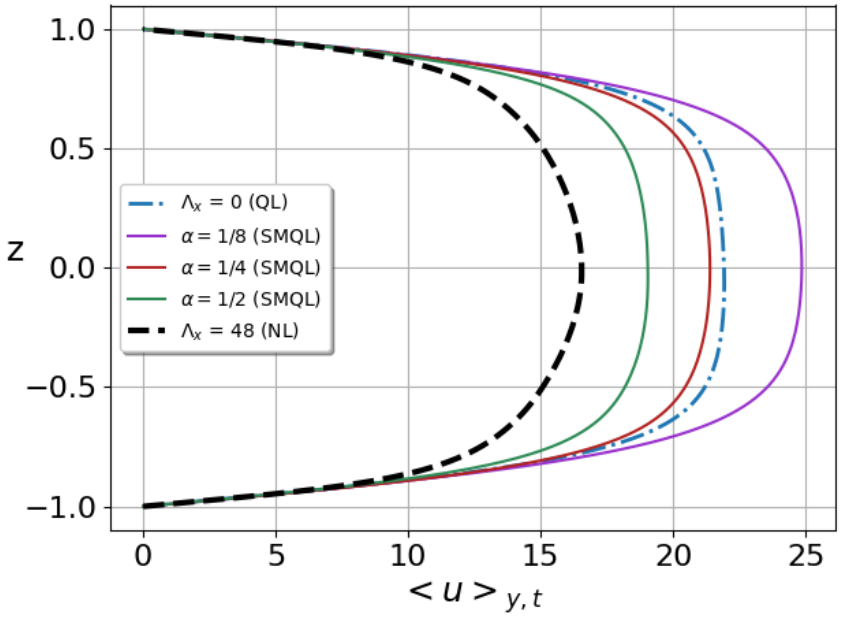

Figure 5.2: Comparison of mean velocity profiles obtained by using SMQL but retaining various harmonics of the fundamental wavenumber compared to QL and NL.

ity profiles for the SMQL simulations are nearly indistinguishable, which demonstrates the versatility of the Dedalus/Python code and provides an independent check on that software, at least for first-order statistics. As the focus of this simulation is on validating the SMQL code, no further analysis is presented. However, the verification that a minimum model for QL sustains turbulence gives further credence to the significance of the instability of the streamwise streaks in the self-sustaining process theory of Waleffe (1997), and vortex-wave interaction theory of Hall and Smith (1991), Hall and Sherwin (2010) and its extension by Chini et al. (2017).

It is also worth noting that the SMQL algorithm does not outperform the QL approximation in terms of accurately reproducing the mean velocity profile compared to the fully nonlinear case, but this conclusion is dependent on the choice of the retained streamwise fluctuation mode. Although all of the harmonics in NL are included in QL in principle, Bretheim et al. (2018) demonstrated that retaining a particular harmonic and suppressing the remaining set actually could improve the accuracy of the SMQL model while also re-

ducing computational cost. To demonstrate this point, additional SMQL simulations were performed using different harmonics of the fundamental wavenumber. Indeed, Figure 5.2 demonstrates accuracy does depend on the choice of the streamwise Fourier mode retained.

Bretheim et al. (2018) further suggested that selectively retaining (and neglecting) specific harmonics using a technique called "band-limiting" could further improve accuracy while still preserving the improvement in computational efficiency. While identifying the best choice for the set of retained streamwise Fourier modes remains a challenge, this idea also could be applied to GQL using a similar strategy termed "sideband truncation" by Boyd (2001). Applied to GQL, a specific subset of high (i.e., linearized) streamwise Fourier modes would be retained and all other high modes neglected, which would yield a significant increase in computational efficiency relative to existing GQL algorithms. The challenge in adapting this strategy to GQL, however, is not only to properly determine the energy containing modes, but also to ensure that the additional restriction is performed in a manner compatible with energy conservation.

5.2 Low Reynolds number turbulence

Cases	$[L_x, L_y, L_z]$	N_x x N_y x N_z	Re_τ	Re_{CL}
$\Lambda_x = 0$ (QL) $\Lambda_x = 3$ (GQL3) $\Lambda_x = 15$ (GQL15) $\Lambda_x = 72$ (NL)	$[16\pi, 8\pi, 2]$	144 x 144 x 144	100	10,000

Table 5.2: Low Reynolds number regime parameters.

At $Re_\tau = 100$, and again choosing $L_x = 16\pi$ and $L_y = 8\pi$ (Table 5.2), QL, GQL3, and NL simulations each sustain turbulence. Each simulation is initialized from a previous simulation with the same Λ_x in a statistically steady state and re-scaled in order to improve resolution and reduce computational time. The data from the last 200 nondimensional time units from each simulation are used in the analysis that follows. As in the previous section, the mean is defined as the time and horizontal spatial average.

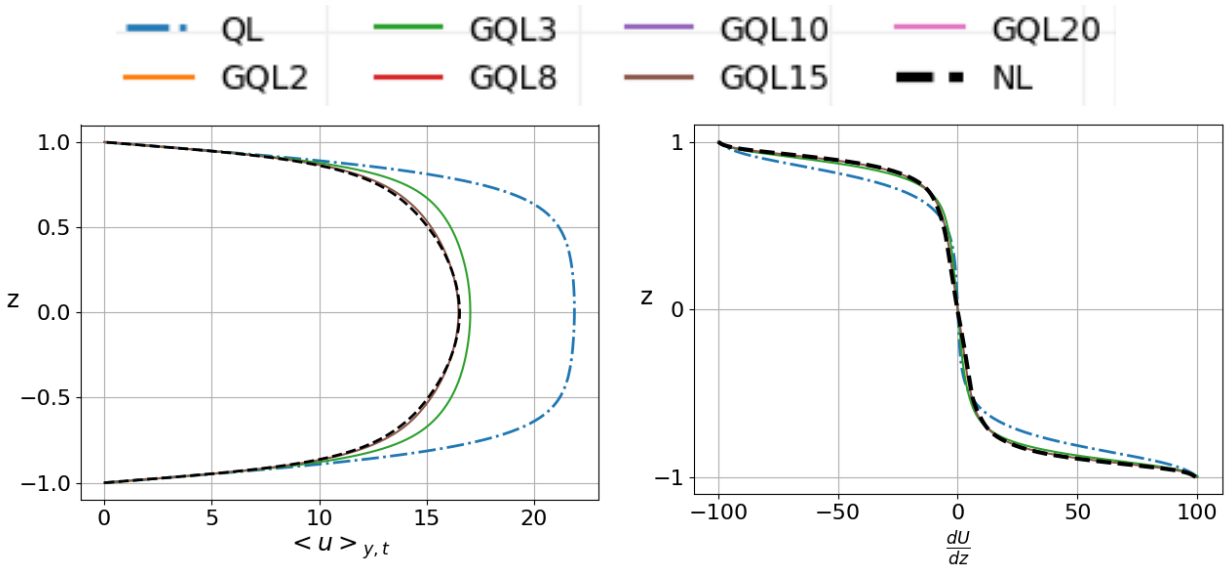

(a) (b)

Figure 5.3: (a) Mean streamwise velocity profile and (b) the mean velocity gradient for simulations at $Re_\tau = 100$.

The mean streamwise velocity and mean velocity gradient profiles are shown in Figure 5.3. As in the high Reynolds number regime, GQL outperforms QL in reproducing first-order statistics, and QL over-predicts the mixing in the core and overestimates the shear near the walls. Interestingly, GQL slightly overestimates the magnitude of the mean velocity in the lower Reynolds number regime, whereas the various GQL simulations consistently underestimate the magnitude of the mean velocity in the high Reynolds number regime.

Figure 5.4 shows a comparison of the instantaneous streamwise velocity and instantaneous streamwise velocity fluctuations obtained from the QL, select GQL, and the NL simulations. The QL simulation is dominated by streaky one-component flow near the wall, while the banding patterns characteristic of low Reynolds number flows seen in the NL simulation are reproduced by GQL3.

The root-mean-square velocity fluctuation profiles in Figure 5.5 and select Reynolds stress profiles in Figure 5.6 again demonstrate that GQL better recovers the fundamental physics of the flow than does QL. These results also suggest that the improvement in accuracy of GQL over QL in the lower Reynolds number regime is less dramatic for modest spectral

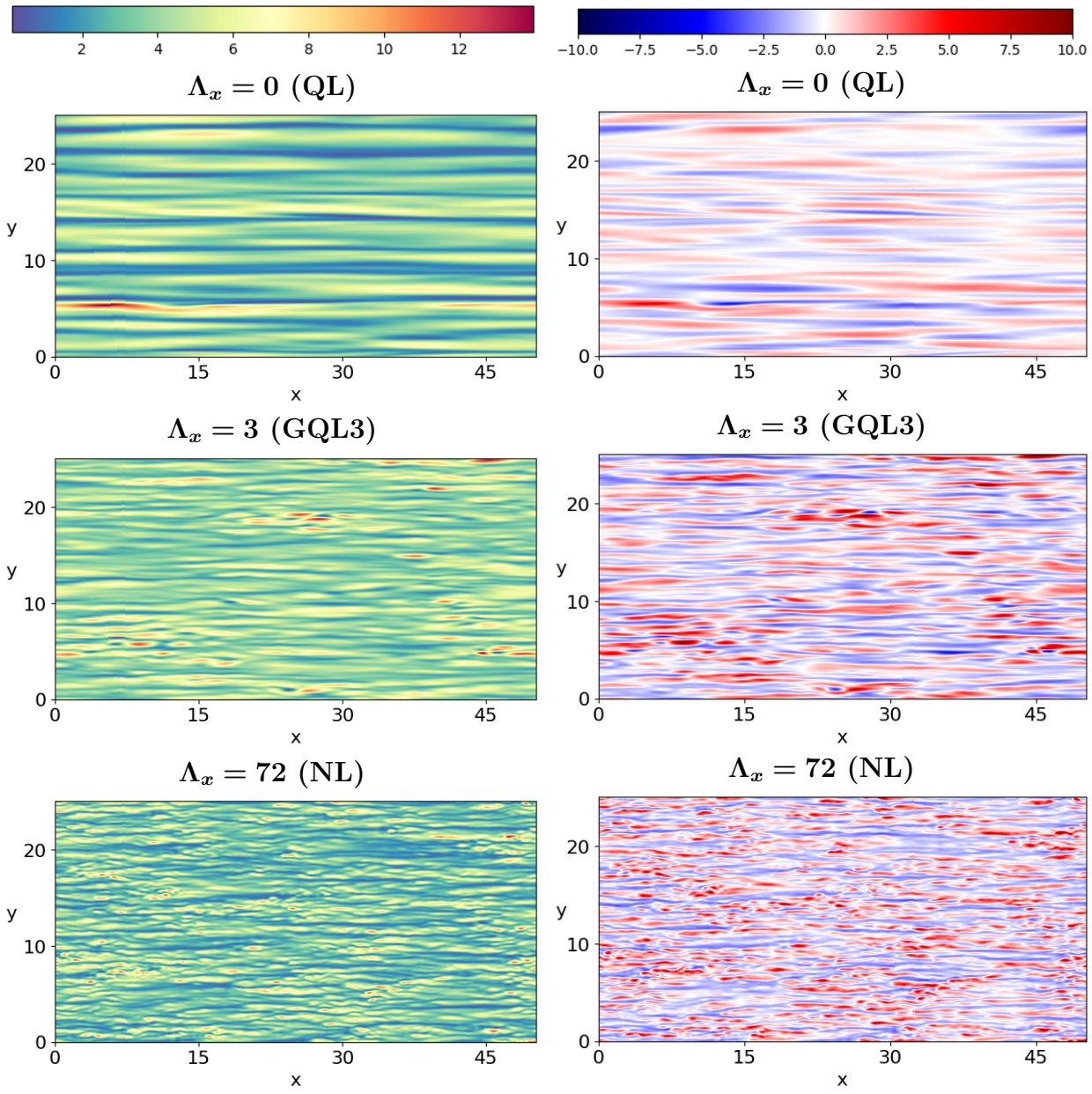

Figure 5.4: Instantaneous streamwise velocity (left column) and instantaneous streamwise velocity fluctuations (right column) for select simulations at $Re_\tau = 100$ at $z^+ = 10$ (near wall location).

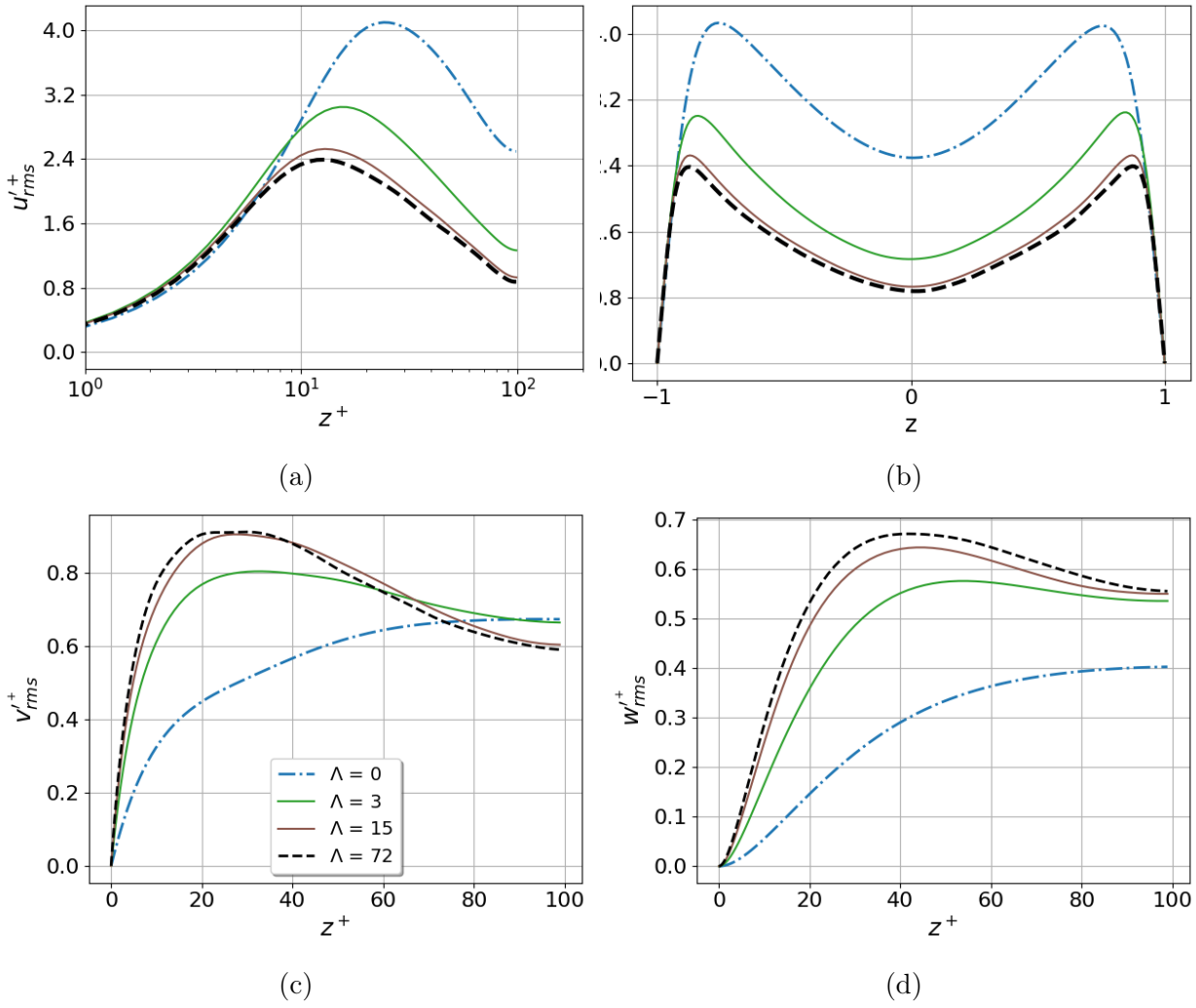

Figure 5.5: Root-mean-square fluctuating velocity components for various Λ_x at $Re_\tau = 100$. (a) u'_{rms} in inner normalized and (b) outer normalized units, (c) v'_{rms} and (d) w'_{rms}. Legend in (c) applies to all four subplots.

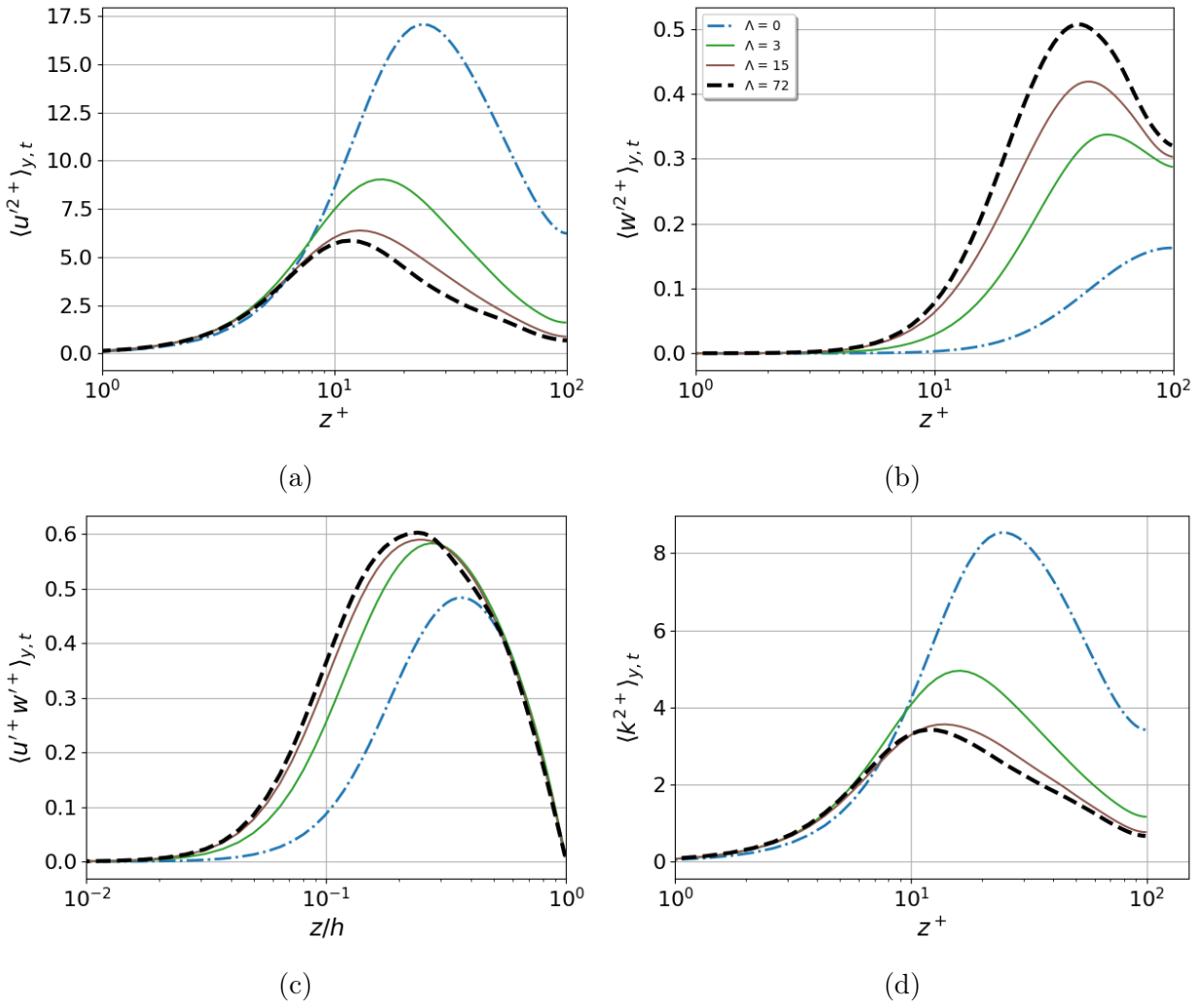

Figure 5.6: Select Reynolds stress profiles and turbulent kinetic energy profile for all simulations, where (a): $\langle u'^{+2} \rangle_{y,t}$, (b): $\langle w'^{+2} \rangle_{y,t}$, (c): $\langle u'^{+} w'^{+} \rangle_{y,t}$, and (d): $\langle k^{+2} \rangle_{y,t}$. Legend in (b) applies to all four subplots.

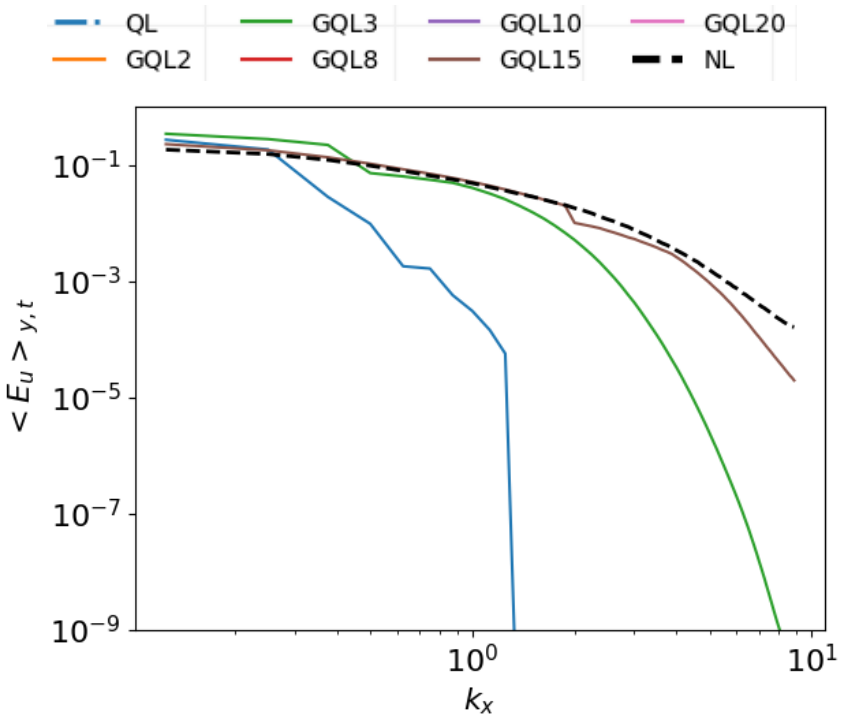

Figure 5.7: Time- and spanwise-averaged streamwise kinetic energy $\langle E_{u'} \rangle_{y,t}$ as a function of k_x for select simulations at $Re_\tau = 100$.

cutoff values, but a more comprehensive analysis for intermediate values of Λ_x is warranted.

Finally, the time- and spanwise-averaged streamwise kinetic energy spectra, shown in Figure 5.7, are qualitatively similar to those realized at higher Reynolds number. In particular, a discontinuity is present in the select GQL simulations shown, although notably the GQL15 simulation does not exhibit strongly damped high modes as is the case in the $Re_\tau = 200$ regime.

Chapter 6

Spectral Energy Discontinuity in GQL

When examining the energy spectra at $Re_\tau = 200$ for various truncations of GQL, a discontinuity is evident in the one-dimensional spanwise-averaged energy spectra of u' at the spectral cutoff Λ_x. For $\Lambda_x \leq 3$, the discontinuity exists only in the slope of the energy spectra, but as the spectral cutoff is increased, a discontinuity exists in the energy itself. For $\Lambda_x \geq 15$ the energy spectra drops to machine precision at the spectral cutoff and the high modes are strongly damped. The discontinuity in the slope of the energy spectra at the spectral cutoff of the GQL simulations is expected, given that the large and small scales are governed by different differential equations. The discontinuity in the energy itself is investigated in this chapter.

6.1 The role of streak instability

The spectral energy discontinuity observed in Figure 6.1 has been documented, although not analyzed in detail, by other investigators in both RNL and GQL. The strong damping of high modes in the QL simulation is also evident in the RNL simulations of channel flow at much higher Reynolds number performed by Farrell et al. (2016). Although in that work the amplitude of the different Fourier modes are plotted as functions of time, the highest modes are strongly damped and it could be argued that other modes $k_x > 12$ are strongly damped in the long-time limit. Moreover, the spectral energy discontinuity observed in GQL8 and GQL10 was also noted by Child et al. (2016) in their GQL simulation of the HMRI at

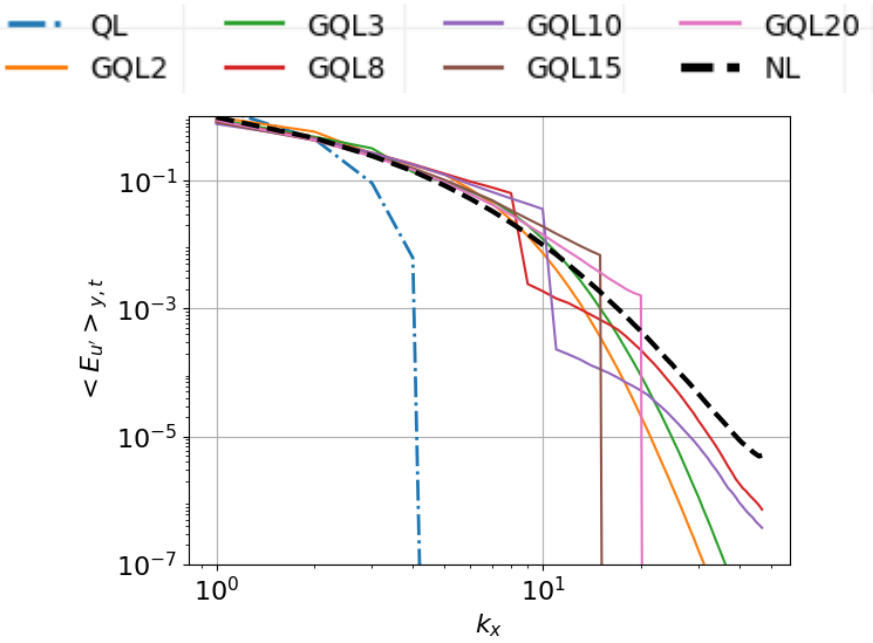

Figure 6.1: Spectral energy discontinuity in GQL simulations of channel flow at $Re_\tau = 200$ (see Chapter 4)

a modest spectral cutoff of $\Lambda = 20$ (of 600 total Fourier modes used). Interestingly, the discontinuity is seen in the energy spectra for the velocity as well as the magnetic field.

Stability theory provides a heuristic framework for understanding the fate of high modes in GQL simulations. Specifically, the mechanism that enables the growth and sustenance of a given high mode is a generalized instability of the mean flow to the fluctuations, where for GQL, the "mean" includes all of the low modes and the "fluctuations" are the high modes. Recall from Chapter 3 the spectral representation of the equations of motion for the GQL approximation:

$$\partial_t \boldsymbol{u}_\ell = \mathcal{L}(\boldsymbol{u}_\ell) + \mathcal{N}_\ell(\boldsymbol{u}_h, \boldsymbol{u}_h) + \mathcal{N}_\ell(\boldsymbol{u}_\ell, \boldsymbol{u}_\ell) \tag{6.1}$$

$$\partial_t \boldsymbol{u}_h = \mathcal{L}(\boldsymbol{u}_h) + \mathcal{N}_h(\boldsymbol{u}_\ell, \boldsymbol{u}_h) + \mathcal{N}_h(\boldsymbol{u}_h, \boldsymbol{u}_\ell) \tag{6.2}$$

Given this notion of instability versus non-local energy scatter, a preliminary explanation of the spectral energy discontinuity is that for modest spectral cutoffs ($\Lambda_x \leq 3$ for the simulations performed in this work), unstable modes are contained in both the low- and

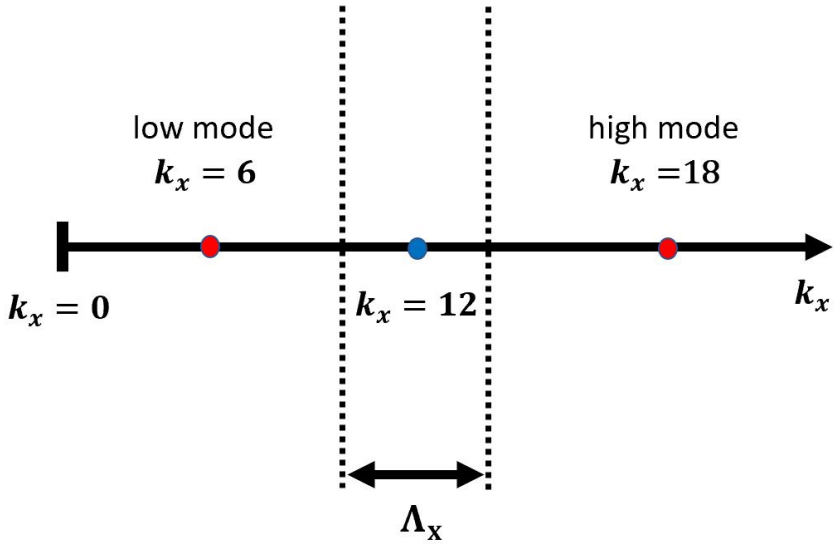

Figure 6.2: Graphic to supplement preliminary explanation of energy discontinuity exhibited by GQL simulations in Figure 6.1.

high-mode sets, allowing for the growth and sustenance of turbulence through an instability of the mean streaky flow to the fluctuations. As the spectral cutoff increases, however, the band of unstable modes is eventually confined to the low modes, dramatically reducing the efficiency of spectrally non-local energy transfers among different high modes and resulting in strongly damped high modes.

The explanation given above is presented graphically in Figure 6.2. Assume, for example, $k_x = 12$ is the highest mode unstable to the $k_x = 0$ mode (the mean) and let $\Lambda_x > 6$. Then $k_x = 6$ is always considered a low mode. For $6 < \Lambda_x < 12$, the resulting nonlinear interaction between the low mode $k_x = 6$ and the high mode $k_x = 12$ generates a high mode $k_x = 18$, which is a nonlinear interaction permitted in the GQL approximation. However, if $\Lambda_x > 12$, $k_x = 12$ is a low mode, and the interaction between a low mode and a low mode that creates a high mode is *not* permitted in the GQL approximation. Indeed, in this study, for $\Lambda_x > 15$, the energy drops to machine precision and GQL20 acts like an implicit LES simulation or an under-resolved DNS. For $8 \leq \Lambda_x < 15$, the energy recovers past the spectral cutoff, suggesting a mode unstable to the zero mode is contained in the high mode set.

To assess this conjecture, determination of the precise scales that exhibit linear instabilities in the fully nonlinear flow and quantification of the rates of (spectrally non-local) energy scattering among the high modes is necessary. Investigating streak instabilities suggests the need for stability analysis about a fully two-dimensional (and possibly time-dependent) streak flow; a simpler alternative is explored in the next section.

6.2 Hydrodynamic stability theory

The stability of laminar plane Poiseuille flow has been extensively studied by finding solutions to the Orr-Sommerfeld eigenvalue equation (Orr, 1907; Sommerfeld, 1908). The wall-normal (z) velocity fluctuation is assumed to be proportional to the real part of a streamwise-varying wave-like disturbance of the form

$$w' \propto \hat{w}(z) e^{i\alpha x} e^{\sigma t} \tag{6.3}$$

where the wavenumber $\alpha = 2\pi/\lambda_x$, with λ_x the x-wavelength of the disturbance, is assumed to be a positive real number, and $\sigma = \sigma_r + i\sigma_i$ is the complex growth rate. Linearizing the Navier-Stokes equations about the laminar solution, $\overline{u} = \langle u \rangle_{x,z,t}(z)$, and reducing the problem to two dimensions via Squire's theorem, the result is the well-known Orr-Sommerfeld equation

$$Re\left[(i\alpha\overline{u} + \sigma)\left(\frac{d^2\hat{w}}{dz} - \alpha^2\hat{w}\right) - i\alpha\frac{d^2\overline{u}}{dz}\hat{w}\right] - \frac{d^4\hat{w}}{dz} + 2\alpha^2\frac{d^2\hat{w}}{dz} + \alpha^4\hat{w} = 0 \tag{6.4}$$

$$\hat{w}(\pm 1) = \hat{w}'(\pm 1) = 0 \tag{6.5}$$

In the eigenproblem, $\sigma_r > 0$ is a linearly unstable eigenvalue, which permits the amplitude of the wall-normal velocity fluctuation to grow exponentially in time (Orszag, 1971).

For turbulent flows, however, this classical hydrodynamic stability theory has not yielded especially promising results. Malkus (1956) suggested that extending the Orr-Sommerfeld equation to turbulent flows by linearizing about the turbulent mean (rather than the laminar) velocity profile would result in marginally stable or neutrally stable modes at the flow

Reynolds number, but this proposal was eventually disproved by Reynolds and Tiederman (1967). Reynolds and Hussain (1972) developed a model that replaced the molecular viscosity in the Orr-Sommerfeld equation with additional terms that depend on a prescribed eddy viscosity and its derivatives, but this modification did not result in unstable modes either. Finally, Sen and Veeravali (2000) proposed an eddy viscosity model that could account for the anisotropy of the dynamics as a function of the distance from the wall that did yield a band of unstable modes. All of these various approaches are explored in this section, if only to motivate a more systematic approach.

For all computations, the Orr-Sommerfeld eigenproblem is solved using the eigenvalue problem solver native to Dedalus. The solver requires the user to enter only the governing PDE and boundary conditions, the range of wavenumbers to be analyzed, and a specified number of eigenvalues to return for each wavenumber. For each wavenumber, a sparse solver algorithm is employed, which yields the eigenvalues near a specified target eigenvalue, σ_T. Since the objective is to identify the threshold streamwise wavenumber separating growing and decaying modes, σ_T is set to zero and the typical number of eigenvalues returned for each α is $N = 120$. Dedalus then returns the maximum growth rate, σ_r, for each value of α.

Classic Orr-Sommerfeld analysis

In the classical Orr-Sommerfeld problem specified by Equation (6.4), the flow is linearized about the steady state (i.e., laminar) solution, where $\overline{u} = (1-z^2)$ and $\frac{d^2\overline{u}}{dz} = 2$. For centerline velocity Reynolds number $Re_{CL} = 5776$, there is a single marginal mode with streamwise wavenumber $\alpha = 1.02$. This result was replicated using the stability analysis coded in Dedalus, as shown in Figure 6.3a.

Turbulent mean

To begin the linear stability analysis for the parameter regime in Chapter 4, the laminar solution $\overline{u}$ in Equation (6.4) was replaced by the time- and horizontally-averaged turbulent

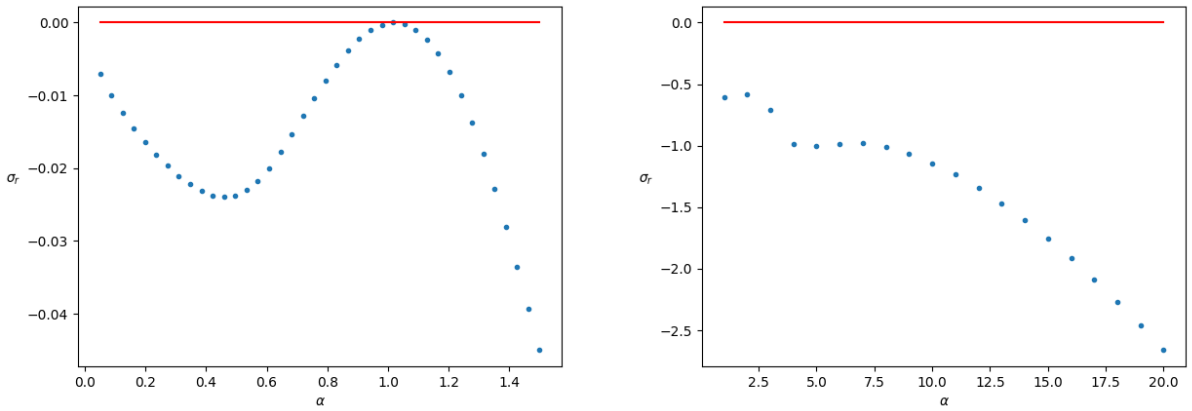

(a) (b)

Figure 6.3: Growth rate curves for (a) classic Orr-Sommerfeld stability problem at $Re = 5776$ and (b) Orr-Sommerfeld stability problem at $Re_\tau = 200$ linearized about the turbulent mean.

mean velocity profile extracted from the fully nonlinear simulation at $Re_\tau = 200$. Not unexpectedly, (based on the work of Reynolds and Tiederman (1967)), Figure 6.3b confirms that all modes are damped at the flow Reynolds number.

Eddy viscosity model

The next step was to reproduce the results of the eddy viscosity model developed by Sen and Veeravali (2000), which accounts for the characteristic anisotropy of wall-bounded turbulence. In this model, the Orr-Sommerfeld equation is modified with an additional set of terms:

$$\begin{aligned} &Re_\tau \left[(i\alpha\overline{u} + \sigma)\left(\hat{w}'' - \alpha^2\hat{w}\right) - i\alpha\overline{u}''\hat{w}\right] - \left[\hat{w}'''' - 2\alpha^2\hat{w}'' + \alpha^4\hat{w}\right] \\ &- \left[E(\hat{w}'''' - 2\alpha^2\hat{w}'' + \alpha^4\hat{w}) + 2E'(\hat{w}''' - \alpha^2\hat{w}') + E''(\hat{w}'' - \alpha^2\hat{w})\right] \\ &-\lambda E\left[-2i\alpha\hat{w}''' + 2i\alpha^3\hat{w}'\right] - 2i\alpha\hat{w}'\left[\lambda E'' + 2\lambda' E' + \lambda'' E\right] = 0 \end{aligned} \tag{6.6}$$

where the primes indicate differentiation with respect to z. The first line of Equation (6.6) is the classic Orr-Sommerfeld equation. The second line includes all terms in an isotropic

eddy viscosity model, where E is the normalized eddy viscosity. The third line involves the anisotropy parameter λ and its derivatives.

The normalized eddy viscosity E and the anisotropy parameter λ are defined as

$$\lambda = C(k/\epsilon_d)\frac{d\overline{u}}{dz} \tag{6.7}$$

$$E = \frac{\epsilon}{\nu} = \frac{-1}{\nu}\frac{\langle u_i u_j \rangle}{d\overline{u}/dz} \tag{6.8}$$

where k is the turbulent kinetic energy, ϵ_d is the dissipation rate of turbulent kinetic energy, and C is a constant. Sen and Veeravali (2000) employ the following analytical expressions to model the eddy viscosity and the anisotropy parameter:

$$E(z) = \frac{1}{2}\left[1 + \kappa^2 Re_\tau^2/9(2z - z^2)^2(3 - 4z + 2z^2)^2(1 - \exp(-zRe_\tau/A^+))^2\right]^{\frac{1}{2}} - \frac{1}{2} \tag{6.9}$$

$$\lambda(z) = 10\left[3/10 + \left(\frac{1 - 3/10}{2}\right)\left(1 - \text{erf}\left(\frac{z - 0.5}{0.25}\right)\right)\right] \tag{6.10}$$

where $\kappa = 0.4$ is the von Kármán constant and $A^+ = 27$ is the Van Dreist constant.

The eigenvalue problem was solved over a half-channel with the anti-symmetry boundary conditions at the centerline

$$\hat{w}(z = 0) = 0; \quad \hat{w}'(z = 0) = 0 \tag{6.11}$$

$$\hat{w}'(z = 1) = 0; \quad \hat{w}'''(z = 1) = 0 \tag{6.12}$$

where here $z = 0$ is the bottom of the channel and $z = 1$ is the centerline. The notation and wall coordinate system is slightly different than used in Equation (6.4) to accord with that of Sen and Veeravali (2000). When $\lambda = 0$ all modes should be damped, as discussed by Sen and Veeravali (2000); see Figure 6.4a.

Results obtained using the fully modified Orr-Sommerfeld equation are shown in Figure 6.4b, which reveals a band of unstable modes. This result directly supports the notion that a sufficiently high spectral cutoff results in all unstable modes being included in the low-mode set. Of course, this conclusion should be viewed with caution: the *ad hoc* model-

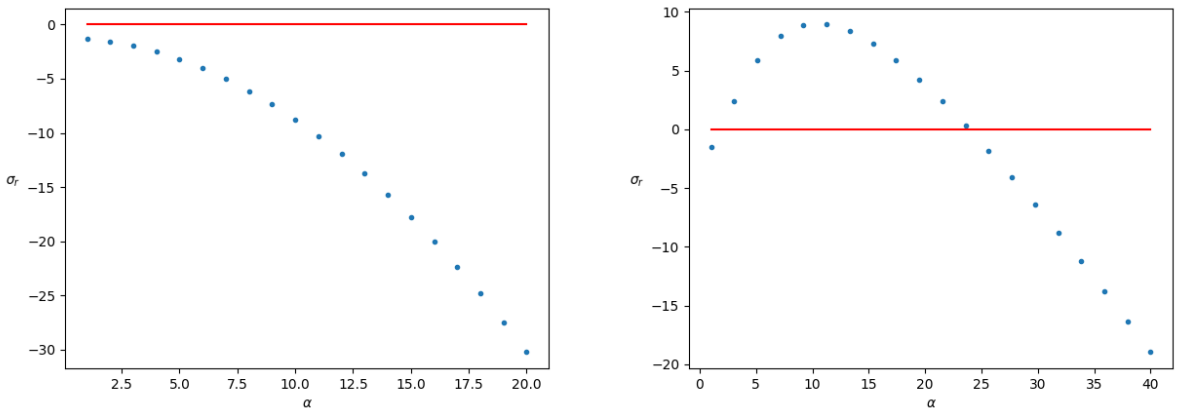

(a) (b)

Figure 6.4: (a) Orr-Sommerfeld stability problem at $Re_\tau = 200$ linearized about the turbulent mean with isotropic eddy viscosity and (b) fully-modified Orr-Sommerfeld stability problem of Sen and Veeravali (2000) at $Re_\tau = 200$ exhibiting a band of unstable modes.

ing used to specify the eddy viscosity and the anisotropy terms make the results suggestive at best. Indeed, the use of other expressions for λ as defined in Sen and Veeravali (2000) either yields strongly damped modes or a band of unstable modes that includes the entire streamwise wavenumber spectrum.

A more precise approach is to test the linear stability of the time- and streamwise-averaged streaky flow using either a spatial Floquet analysis or a forward/adjoint time-stepping scheme. This approach also has a clearer link to the self-sustaining process of Waleffe (1997). Although such an analysis has been left for future work, the results shown in Figure 6.4b do support the conjecture that the discontinuity in the energy spectrum may be attributable to a lack of instability in the high mode set.

Chapter 7

Conclusion

The purpose of this work was to further establish the generalized quasilinear (GQL) approximation as a robust, accurate, and computationally efficient alternative to existing methods of numerically simulating turbulent flow by investigating its effectiveness in 3D turbulent channel flow. Although the GQL approximation has been applied to other turbulent systems, this study constitutes the first engineering flow to be explored and only the second application of GQL in three dimensions. Additionally, channel flow is only weakly linearly unstable in the inviscid limit, in contrast to all other flows simulated using GQL to date. Finally, $Re_\tau = 200$ is the highest Reynolds number parameter regime explored using GQL in any system. In this chapter, the primary areas of investigation, significant findings, and open questions relating to those outcomes are reviewed.

Accuracy of GQL turbulent channel flow simulations

The GQL algorithm developed and used in this work is capable of operating in four modalities, ranging from extreme truncation (single-mode QL, i.e., SMQL) to full DNS. GQL simulations with varying values of the streamwise spectral cutoff Λ_x were performed in two parameter regimes: $Re_\tau = 100$ with the nondimensional domain $[16\pi, 8\pi, 2]$, and $Re_\tau = 200$, with the nondimensional domain $[2\pi, \pi, 2]$. In both regimes, sustained turbulence was achieved. As both QL and GQL employ a linearization about the *streamwise-averaged* mean, in contrast to other methodologies, these results lend further credibility to the role of

streak instabilities in the self-sustaining process (SSP) of Waleffe (1997). However, the GQL simulations, even those with a modest number of low modes retained ($\Lambda_x \leq 3$), significantly outperformed QL in reproducing the first-and second-order turbulence statistics, and accurately captured the small-scale instantaneous dynamics and characteristic structure of the flow.

To quantify the accuracy of the GQL approximation, a variety of turbulence metrics was used. This quantitative study also illuminated the role of the nonlinear interactions that are retained (or neglected) depending on the spectral cutoff Λ_x. The QL approximation, due to the severe restriction of nonlinear-nonlinear interactions among the non-mean modes, does not accurately predict the energy distribution in the system, underestimates Reynolds shear stress near the wall, and over-predicts mixing in the core. As a consequence, the influence of the viscous forces extends farther from the wall which encroaches on other regions of the flow and fundamentally alters the flow dynamics. Specifically, two-component flow is not recovered very near the wall, there is a delay in streak breakdown, resulting in the persistence of predominantly one-component streaky flow too far from the wall, and no evidence of log region dynamics is observed.

In contrast, the GQL simulations, even with a modest number of low modes retained, is significantly better at predicting the energy distribution across the dynamic range of scales and outperforms QL in every metric considered in both Reynolds number parameter regimes studied in this work. Perhaps the most impressive results are the comparisons of the turbulence intensity profiles (Figure 4.11) and Reynolds stress profiles (Figure 4.12) at $Re_\tau = 200$, in which the GQL profiles are shown to be in remarkably good agreement with NL and experimental results, while the QL profiles show significant deviations. The GQL simulations have also been shown to reproduce the characteristic dynamics of wall-bounded shear flows, including two-component flow very close to the wall, no evidence of delayed streak breakdown, and the emergence of the log layer.

Although GQL has been shown to reproduce instantaneous features and turbulence statis-

tics better than QL, the improvement in accuracy is non-monotonic at $Re_\tau = 200$ and yields diminishing returns as Λ_x is increased further, an observation also made by other investigators for different flows (Child et al., 2016; Tobias and Marston, 2017). In the low Reynolds number regime, the improvement in accuracy is less pronounced for modest values of the spectral cutoff. Given the objectives of this study, the analysis only considered a subset of the possible values for Λ_x. A more complete examination of GQL in channel flow (i.e., at all possible values of Λ_x) in both parameter regimes may yield additional insights into the effect of inhibiting particular nonlinear interactions among the large scales. Owing to time constraints, the analysis of the behavior of the nonlinear energy transfers was limited, though promising. Using a spectral approach introduced by Domaradzki et al. (1994), the nonlinear energy transfer can be isolated and an estimate of the nonlinear energy transfer between two fixed wavenumber bands can be determined. The aforementioned concepts can facilitate the targeted analysis of local and non-local nonlinear energy transfer in the flow. This methodology can (and should) be utilized to more fully investigate the physical effect of restricting specific nonlinear interactions in the GQL simulations and can potentially shed light on the non-monotonicity of the accuracy of GQL.

Spectral energy discontinuity at high GQL truncations

One of the most significant findings in this work was the identification and subsequent analysis of a discontinuity in the streamwise fluctuating velocity energy spectrum at $Re_\tau = 200$ (see Figure 4.20). For $\Lambda_x \leq 3$, the discontinuity exists in the slope of the energy spectra, but as Λ_x is increased, the discontinuity is seen in the energy itself at precisely the spectral cutoff. For $\Lambda_x \geq 15$ (given the data available in this study), the energy drops to machine precision at Λ_x and negligible energy exists in the high modes. The discontinuity is also observed at $Re_\tau = 100$ in this work (see Figure 5.7). Interestingly, this phenomenon was captured by Child et al. (2016) in their analysis of the helical magnetorotational instability (HMRI) and is (implicitly) evident in a restricted nonlinear (RNL) simulation for plane

Poiseuille flow at $Re_\tau = 940$ by Farrell et al. (2016).

One explanation for the spectral energy discontinuity is that for the given parameter values, the instability in the streaks is present only in modes with mode numbers less than 15. Therefore, for $\Lambda_x \geq 15$, all flow instabilities are contained in the low modes, and the high modes, which cannot scatter energy *directly* among themselves, become strongly damped. Confirmation requires a precise knowledge of which scales exhibit linear instabilities in the fully nonlinear flow and quantification of the rates of (spectrally non-local) energy scattering among the high modes. Using the governing equations for GQL and stability theory as a guide, a high mode in GQL can grow and be sustained through an instability of the "mean" (i.e., low-mode) flow to that high mode. This mechanism was investigated using hydrodynamic stability theory. Despite the mixed success in producing meaningful results in turbulent flows, this approach was deemed to be the simplest first step in exploring the issue of stability in the context of fully NL simulations. Several analyses were performed using the Orr-Sommerfeld equation: first, by linearizing about the turbulent time-averaged mean (as opposed to the laminar solution in the classic analysis); secondly, by modifying the Orr-Sommerfeld equation with the addition of an eddy viscosity; and by additionally incorporating anisotropic eddy diffusion (Orszag, 1971; Sen and Veeravali, 2000). Linear stability analysis using the Orr-Sommerfeld equation as modified by Sen and Veeravali (2000) yielded a band of unstable modes for the high Reynolds number regime, confirming the plausibility of the conjectured mechanism. Nevertheless, the reliability of this result may be questioned given the extensive *ad hoc* modeling of the parameters and inconsistent results obtained if other models are used. Ultimately, these efforts strongly suggest an alternative methodology: linearizing about the 2D streaks as opposed to the 1D time-averaged and horizontally-averaged mean velocity profile, and solving the resulting eigenvalue problem using either spatial Floquet theory or a forward-adjoint time-stepping algorithm. Both methods are non-trivial to derive and implement, and so were not pursued in this work, but constitute a natural next step in the continuation of this research.

Computational efficiency of GQL

Computational efficiency is a primary consideration in the simulation of turbulent flows. Although not analyzed in great detail, computational efficiency data for all simulations was collected and is included as Appendix A. An intriguing and, indeed, puzzling observation is that certain GQL simulations were significantly faster (in terms of wall-clock time) than NL and even QL simulations. This finding seems counter-intuitive because the GQL algorithm used in this work does not eliminate modes, requiring the inversion of large matrices at every time step regardless of the value set for Λ_x. The precise reason for the efficiency of GQL3 over NL and QL has not yet been determined and should be pursued in future studies.

One potential improvement of the GQL algorithm considered in the course of this work is based on the concept of "band-limiting" introduced by Bretheim et al. (2018) for QL. In employing "sideband truncation" in GQL, the spectral cutoff Λ_x still establishes the low modes permitted to interact nonlinearly, but an additional restriction is made on the high modes whereby only a select band of fluctuation modes is retained. All other high modes are neglected or artificially damped. Sideband truncation may provide marked improvement in efficiency, but further study is needed to identify the appropriate band of fluctuation modes to retain and to ensure energy is conserved in the inviscid limit.

List of references

Acarlar, M. S. and C. R. Smith
1987. A study of hairpin vortices in a laminar boundary layer. Part 1. Hairpin vortices generated by a hemisphere protuberance. *J. Fluid Mech.*, 175:1–41.

Aghdam, S. K. and P. Ricco
2016. Laminar and turbulent flows over hydrophobic surfaces with shear-dependent slip length. *Phys. Fluids*, 28:035109–1.

Bakker, A.
2018. Prediction methods of turbulent simulations. [Online; graphic accessed 1 Nov 2018].

Beaume, C., E. Knobloch, G. P. Chini, and K. Julien
2015. Exact coherent structures in an asymptotically reduced description of parallel shear flows. *Fluid Dyn. Res.*, 47.

Benney, D. J.
1984. The evolution of disturbances in shear flows at high Reynolds numbers. *Stud. Appl. Math*, 70:1–19.

Boyd, J. P.
2001. *Chebyshev and Fourier Spectral Methods*, second (revised) edition. Mineola, NY: Dover Publications, Inc.

Bretheim, J. U., C. Meneveau, and D. F. Gayme
2018. A restricted nonlinear large eddy simulation model for high Reynolds number flows. *J. Turbul.*, 19:141–166.

Burns, K. J., G. M. Vasil, J. S. Oishi, D. Lecoanet, and B. P. Brown
2019. Dedalus: A Flexible Framework for Numerical Simulations with Spectral Methods. *arXiv e-prints*, P. arXiv:1905.10388.

Cantwell, B. J.
1993. On the behavior of velocity gradient tensor invariants in direct numerical simulations of turbulence. *Phys. Fluids A*, 5:357.

Child, A., R. Hollerbach, B. Marston, and S. Tobias
2016. Generalised quasilinear approximation of the helical magnetorotational instability. *J. Plasma Phys.*, 82(3):905820302.

Chini, G. P., B. Montemuro, C. M. White, and J. Klewicki
2017. A self-sustaining process model of inertial layer dynamics in high Reynolds number turbulent wall flows. *Philos. Trans. A Math Phys. Eng. Sci.*, 375.

Cho, M., Y. Hwang, and H. Choi
2018. Scale interactions and spectral energy transfer in turbulent channel flow. *J. Fluid Mech.*, 854:474–504.

Chong, M. S., A. E. Perry, and B. J. Cantwell
1990. A general classification of three dimensional flow fields. *Phys. Fluids A*, 2:765.

Cushman-Roisin, B.
2018. *Environmental Fluid Mechanics*. John Wiley & Sons.

Davidson, P. A.
2015. *Turbulence: An Introduction for Scientists and Engineers*. Oxford, UK: Oxford University Press.

Domaradzki, J. A., W. Liu, C. Härtel, and L. Kleiser
1994. Energy transfer in numerically simulated wall-bounded turbulent flows. *Phys. Fluids*, 6:1583.

Domaradzki, J. A. and R. S. Rogallo
1990. Local energy transfer and nonlocal interactions in homogeneous, isotropic turbulence. *Phys. Fluids A*, 2:413.

Farrell, B. F. and P. J. Ioannou
2003. Structural stability of turbulent jets. *J. Atmos. Sci.*, 60:2101–2118.

Farrell, B. F. and P. J. Ioannou
2007. Structure and spacing of jets in barotropic turbulence. *J. Atmospheric Sci.*, 64:3652–3665.

Farrell, B. F., P. J. Ioannou, J. Jiménez, N. C. Constantinou, A. Lozano-Durán, and M.-A. Nikolaidis
2016. A statistical state dynamics-based study of the structure and mechanism of large-scale motions in plane Poiseuille flow. *J. Fluid Mech.*, 809:290–315.

Ghiasi, Z., D. Li, J. Komperda, and F. Mashayek
2018. Near-wall resolution requirement for direct numerical simulation of turbulent flow using multidomain Chebyshev grid. *Int. J. Heat Mass Transf.*, 126.

Hall, P. and S. Sherwin
2010. Streamwise vortices in shear flows: harbingers of transition and the skeleton of coherent structures. *J. Fluid Mech.*, 661:178–205.

Hall, P. and F. T. Smith
1991. On strongly nonlinear vortex/wave interactions in boundary-layer transition. *J. Fluid Mech.*, 227:641–666.

Hamlington, P. E., D. Krasnov, T. Boeck, and J. Schumacher
2012. Statistics of the energy dissipation rate and local enstrophy in turbulent channel flow. *Physica D*, 241:169–177.

Herring, J. R.
1963. Investigation of problems in thermal convection. *J. Atmos. Sci.*, 20:325–338.

Jiménez, J. and G. Kawahara
2013. Dynamics of wall-bounded turbulence. In *Ten Chapters in Turbulence*, P. Davidson, Y. Kaneda, and K. R. Sreenivasan, eds., chapter 6, Pp. 221–268. Cambridge: Cambridge University Press.

Jiménez , J. and P. Moin
1991. The minimal flow unit in near-wall turbulence. *J. Fluid Mech.*, 225:213–240.

Jiménez , J. and A. Pinelli
1999. The autonomous cycle of near-wall turbulence. *J. Fluid Mech.*, 389:335–359.

Khamlaj, T.
2018. Computation of y+. [Online; graphic accessed 15 May 2019].

Khashehchi, M., G. E. Elsinga, H. Bornstein, C. Atkinson, A. Ooi, I. Marusic, and J. Soria
2009. Studying the invariants of the velocity-gradient tensor of a round turbulent jet using Tomo-PIV. *8th International Symposium on PIV*.

Kim, J., P. Moin, and R. Moser
1987. Turbulence statistics in fully developed channel flow at low Reynolds number. *J. Fluid Mech.*, 177:133–166.

Kline, S. J., W. C. Reynolds, F. A. Schraub, and P. W. Runstadler
1967. The structure of turbulent boundary layers. *J. Fluid Mech.*, 30:741–773.

Kolmogorov, A. N.
1941. The local structure of turbulence in incompressible viscous fluid for very large Reynolds numbers. *Kokl. Akad. Nauk. SSSR*, 30:301 – 305. reprinted in Proc. Royal Soc. Lond. A, volume 434, pages 3-13.

Malkus, W. V. R.
1956. Outline of a theory of turbulent shear flow. *J. Fluid Mech.*, 1:521–539.

Marston, J. B., G. P. Chini, and S. M. Tobias
2016. Generalized quasilinear approximation: Application to zonal jets. *Phys. Rev. Lett*, 116(214501).

Marston, J. B., E. Conover, and T. Schneider
2008. Statistics of an unstable barotropic jet from a cumulant expansion. *J. Atmospheric Sci.*, 65:1955–1966.

Orr, W. M.
1907. The stability or instability of the steady motions of a liquid. Part I. A perfect liquid. *Proc. Royal Ir. Acad. A*, 27:9–68.

Orszag, S. A.
1971. Accurate solution of the Orr-Sommerfeld stability equation. *J. Fluid Mech.*, 50:689–703.

Pope, S. B.
2000. *Turbulent Flows*. Cambridge: Cambridge University Press.

Ramachandran, P. and G. Varoquaux
2011. Mayavi: 3D Visualization of Scientific Data. *Computing in Science & Engineering*, 13(2):40–51.

Reynolds, W. C.
2000. The potential and limitations of direct and large eddy simulations. In *Whither Turbulence? Turbulence at the Crossroads*, J. L. Lumley, ed., volume 357. Springer, Berlin, Heidelberg.

Reynolds, W. C. and A. K. M. F. Hussain
1972. The mechanics of an organized disturbance in turbulent shear flow. Part 3. Theoretical models and comparisons with experiments. *J. Fluid Mech.*, 54:263–288.

Reynolds, W. C. and W. G. Tiederman
1967. Stability of turbulent channel flow, with application to Malkus's theory. *J. Fluid Mech.*, 27:253–272.

Richardson, L. F.
1920. The supply of energy from and to atmospheric eddies. *Proc. Royal Soc. Lond. A*, 97.

Sen, P. K. and S. V. Veeravali
2000. Behavior of organised disturbances in fully developed turbulent channel flow. *Sādhanā*, 25:423–437.

Smits, A. J. and I. Marusic
2013. Wall-bounded turbulence. *Physics Today*, 66:25.

Sommerfeld, A. B.
1908. Ein Beitrag zur hydrodynamische Erklärung der turbulenten Flüssigkeitsbewegungen. *Proceedings of the 4th International Congress of Mathematicians*, III:116–124.

Stuart, J. T.
1958. On the non-linear mechanics of hydrodynamic stability. *J. Fluid Mech.*, 4:1–21.

Tennekes, H. and J. L. Lumley
1972. *A First Course in Turbulence*. Cambridge, MA: MIT Press.

Thomas, V. L., B. F. Farrell, P. J. Ioannou, and D. F. Gayme
2015. A minimal model of self-sustaining turbulence. *Phys. Fluids*, 27.

Thomas, V. L., B. K. Lieu, M. R. Jovanović, B. F. Farrell, P. J. Ioannou, and D. F. Gayme
2014. Self-sustaining turbulence in a restricted nonlinear model of plane Couette flow. *Phys. Fluids*, 26(105112).

Tobias, S. M., K. Dagon, and J. B. Marston
2011. Astrophysical fluid dynamics via direct statistical simulation. *Astrophys. J.*, 727:127.

Tobias, S. M. and J. B. Marston
2017. Three-dimensional rotating Couette flow via the generalised quasilinear approximation. *J. Fluid Mech.*, 810:412–428.

Tobias, S. M., J. Oishi, and J. B. Marston
2018. Generalized quasilinear approximation of the interaction of convection and mean flows in a thermal annulus. *Philos. Trans. Royal Soc. A*, 494.

Trefethen, L.
2000. *Spectral methods in MATLAB*. Philadelphia, PA: Society for Industrial and Applied Mathematics.

Tsukahara, T., Y. Seki, H. Kawamura, and D. Tochio
2005. DNS of turbulent channel flow at very low Reynolds numbers. *TSFP Digital Library Online*.

Waleffe, F.
1997. On a self-sustaining process in shear flows. *Phys. Fluids*, 9.

Waleffe, F., J. Kim, and J. Hamilton
1993. On the origin of streaks in turbulent shear flows. In *Turbulent Shear Flows 8*, F. Durst, R. Friedrich, B. E. Launder, F. W. Schmidt, U. Schumann, and J. H. Whitelaw, eds. Springer, Berlin, Heidelberg.

Waskom, M., O. Botvinnik, and D. O'Kane
. Seaborn.

Appendix A

Computational Efficiency of GQL Algorithm

Although the primary focus of this work is to demonstrate the accuracy of the GQL approximation in turbulent channel flow, the computational time for each simulation was recorded and is presented in this section. An additional efficiency investigation is presented at a lower Reynolds number regime for comparison. Each simulation was performed in parallel on 24 processors with a process mesh size of [6 x 4].

Cases	Time Steps	Avg Δt (non-dim)	Wall Time (D-H:M)
$\Lambda_x = 0$ (QL)	3582600	$5.5560e^{-4}$	6-19:11
$\Lambda_x = 2$ (GQL)	4100800	$4.8770e^{-4}$	5-15:19
$\Lambda_x = 3$ (GQL)	4533000	$4.4675e^{-4}$	5-04:31
$\Lambda_x = 8$ (GQL)	6190200	$3.2339e^{-4}$	7-03:13
$\Lambda_x = 10$ (GQL)	6499300	$3.0820e^{-4}$	7-15:31
$\Lambda_x = 15$ (GQL)	6830400	$2.9374e^{-4}$	15-16:24
$\Lambda_x = 20$ (GQL)	6849300	$2.9323e^{-4}$	15-21:36
$\Lambda_x = 48$ (NL)	6547000	$3.0750e^{-4}$	15-18:57

Table A.1: Efficiency of simulations at $Re_\tau = 200$ in statistically steady state, where Δt has been averaged over last 200 nondimensional time units of the simulation.

Cases	Time Steps	Avg Δt (non-dim)	Wall Time (D-H:M)
$\Lambda_x = 0$ (QL)	746700	$2.6780e^{-3}$	2-11:29
$\Lambda_x = 3$ (GQL)	1203300	$1.6636e^{-3}$	1-09:26
$\Lambda_x = 48$ (NL)	2922400	$6.8687e^{-4}$	13-23:17

Table A.2: Efficiency of simulations at $Re_\tau = 100$, where Δt has been averaged over last 200 nondimensional time units of the simulation.

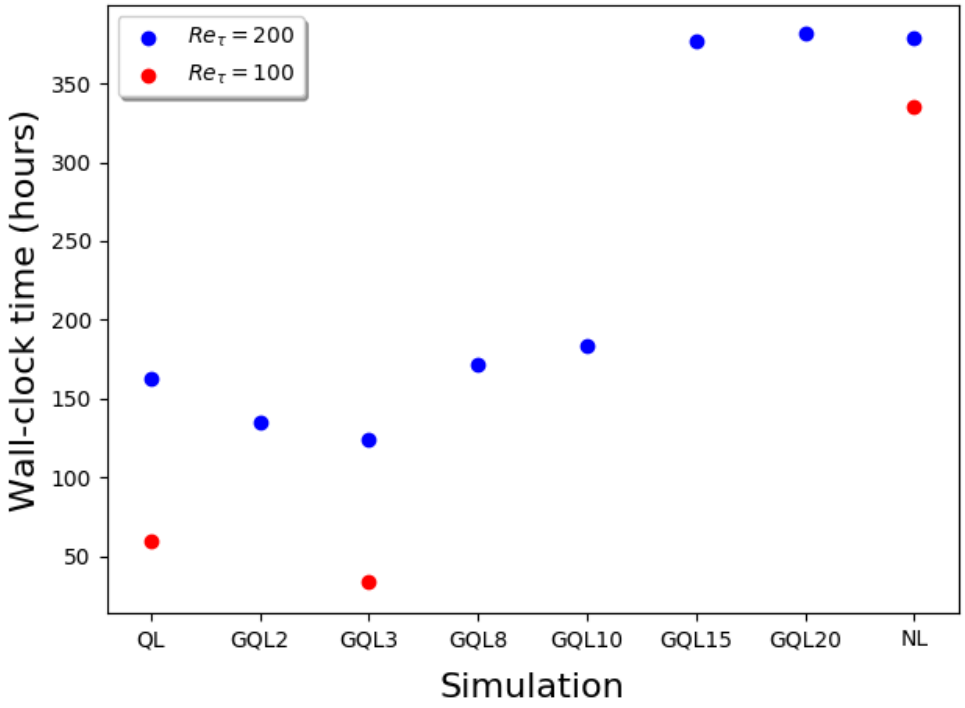

Figure A.1: Wall-clock time of all simulations (in hours) for $Re_\tau = 200$ (blue) and $Re_\tau = 100$ (red).